ABSTRACT

NOWAK, JOSHUA MICHAEL. Development and Characterization of a Hybrid Atmospheric Pressure Plasma Electrospinning System for Nanofiber Enhancement. (Under the directions of Drs. Alexei Saveliev and Mohamed Bourham).

A hybrid atmospheric pressure-electrospinning plasma system was developed to be used for the production of nanofibers and enhance their performance for various applications. Electrospun nanofibers are excellent candidates for protective clothing in the field of chemical and biological warfare defense; however, nanofibers are structurally weak and easily abrade and tear. They can be strengthened through the support of a substrate fabric, but they do not adhere well to substrates. Through the use of the developed hybrid system with either pure He or He/O_2 (99/1) feed gas, adherence to the substrate along with abrasion and flex resistance were improved. The plasma source was diagnosed electrically, thermally, and optically. An equivalent circuit model was developed for non-thermal, highly collisional plasmas that can solve for average electron temperature and electron number density. The obtained temperatures (~ 3eV) correlate very well with the results of a neutral Bremsstrahlung continuum matching technique that was also employed. Using the temperatures and number densities obtained from the circuit model and the optical spectroscopy, a global chemical kinetics code was written in order to solve for radical and ion concentrations. This code shows that there are significant concentrations of oxygen radicals present. The XPS analysis confirmed that there was an increase of surface oxygen from 11.1% up to 16.6% for the He/O_2 plasma and that the C-O bonding, which was not present in the control samples, has increased to 45.4%. The adhesive strength to the substrate has a significant increase of 81% for helium plasma and 144% for He/O_2 plasma; however, these values remain below the desired values for protective clothing applications. The hybrid

system displayed the ability to oxygenate nanofibers as they are being electrospun and shows the feasibility of making other surface modifications. The developed circuit model and chemical kinetics code both show promise as tools for deterministic atmospheric pressure plasma research in the field of surface modifications.

Development and Characterization of a Hybrid Atmospheric Pressure Plasma Electrospinning System for Nanofiber Enhancement

by
Joshua Michael Nowak

A dissertation submitted to the Graduate Faculty of
North Carolina State University
in partial fulfillment of the
requirements for the degree of
Doctor of Philosophy

Mechanical Engineering

Raleigh, North Carolina

2013

APPROVED BY:

Dr. Alexei Saveliev
Co-Chair of Advisory Committee

Dr. Mohamed Bourham
Co-Chair of Advisory Committee

Dr. Gregory Buckner

Dr. Andrey Kuznetsov

Dr. Marian McCord

DEDICATION

To my parents

BIOGRAPHY

Joshua M. Nowak was born December 24, 1982 in Philadelphia, PA. He lived in Sadsburyville, PA until his graduation from Coatesville Area Senior High School in 2001. He began his undergraduate studies at NC State University in the fall of that year. In 2005 he graduated with a B.S. degree in Nuclear Engineering and began his graduate studies. He received a M.S. in Nuclear Engineering with a minor in Physics in 2009.

ACKNOWLEDGMENTS

First, I would like to thank my parents for their love continued support throughout my life and academic career. They have always helped to feed my thirst for knowledge. I must next thank Dr. Mohamed Bourham who was the first person I met at NC State, and he has always been a great mentor in my studies. He was my advisor for my undergraduate and master's degrees always aiding me in whatever I may need. I would like to thank my current advisor Dr. Alexei Saveliev for the helpful conversations and for giving me a new home in Mechanical Engineering after so many years in the Department of Nuclear Engineering. Dr. Andrey Kuznetsov challenged me many years ago in his course on fluid dynamics which has pushed my academic studies to this day. Dr. Gregory Buckner reminded me of my love for engineering with his enthusiastic teaching and hands on projects.

Next, I must give my sincere appreciation to many people in the College of Textiles. Dr. Marian McCord not only welcomed me into her plasma facilities to perform my research, but she has been a good friend who helped me when I had lost my way. Dr. Xiangwu Zhang was instrumental in aiding my research. His knowledge of nanofiber production and facilities were essential. Drs. Narendiran Vitchuli and Quan Shi were with me every step of the way throughout the development of the hybrid system. Not only did they provide technical support with the electrospinning equipment, but they were excellent research partners and good friends.

This work was supported by a grant from DTRA.

TABLE OF CONTENTS

LIST OF TABLES

LIST OF FIGURES

Chapter 1: Introduction and Literature Review

Electrospun nanofibers have shown excellent properties as filtration media against the most penetrating aerosols while remaining breathable. As such they are being considered for protective applications in the field of chemical and biological warfare defense. Electrospun nanofiber mats, however, are structurally weak and require a substrate fabric for support. Adherence to this substrate is difficult because mechanical and wet chemical adherence can easily damage the nanofibers, and adhesives obstruct the small pores that make the nanofibers appealing as a breathable filter. They also show poor resistance to abrasion and tearing. Atmospheric pressure plasma is an attractive option for enhancing nanofiber properties because it can chemically treat the nanofibers without the need for wet chemical processes, will not thermally damage the nanofibers because of its low bulk temperature, and does not require the vacuum systems of low pressure plasmas which prevent continuous treatment and production. Plasma treating nanofibers as they are being electrospun could improve nanofiber adherence to the substrate and other nanofibers, as well as strengthening the nanofibers themselves through increased hydrogen bonding and crosslinking.

1.1 Atmospheric Pressure Plasma

The use of atmospheric pressure plasmas has many advantages over low-pressure and vacuum discharges. The atmospheric discharges allow for the continuous processing of materials because there is no vacuum requirement and no need for a vacuum chamber. These discharges have proven to be the best technique for processes such as textile industry, food packages surface sterilization, and surface modification and functionalization of various paper and pulp products. The systems are economical because processing can be performed faster and does not need large infrastructure as such of the low pressure processing, namely vacuum chambers and pumping systems, power supplies such as high power RF generators, and sophisticated gas manifolds. Generating atmospheric pressure plasmas also allows for different forms of plasmas in the non-thermal regime, generating various radicals useful for surface modification chemistries. Three body reactions become much more likely at higher pressures, which is especially important for the production of ozone whose primary production mechanisms are three body reactions. Indeed, at atmospheric pressure radical production in general is increased and such radicals are important in surface functionalization processes at ambient conditions.

A major pitfall associated with atmospheric pressure plasmas is the possibility of arc formation and generation of streamers. The voltages required for the formation of a plasma discharge at atmospheric pressures are much higher than those required under vacuum. These high voltages can lead to sparking condition and can lead to arc formation if the currents are high. Arcs can easily damage the surface and structure of a substrate, and hence careful limits of operational conditions must be considered. While arcs are used as useful tools in plasma-torches, gouging and metal cutting processes, however, arcs are not desired in plasma surface modification techniques. The suppression of these arcs is crucial for the formation of a non-equilibrium plasma discharge for surface modification of materials such as textiles. Non-equilibrium plasma has the electron temperature much higher than that of the ions and neutrals. The ions, radicals and neutral gas remain at temperatures that will not thermally damage substrates. This allows for surface modification of materials without affecting the material's bulk properties. Applications of atmospheric pressure non-equilibrium plasma for surface modifications are discussed in Section 1.3.

The four main types of atmospheric pressure non-equilibrium plasma discharges used for surface modification are corona, dielectric barrier discharge (DBD), microwave, and plasma jets. A corona discharge is a weakly-luminous discharge appearing around edges, points, and thin wires. The geometry around these features leads to large electric fields that generate this discharge. As such, a corona discharge is non-uniform and centered around one electrode. A schematic of a corona discharge is shown in Figure 1.1.

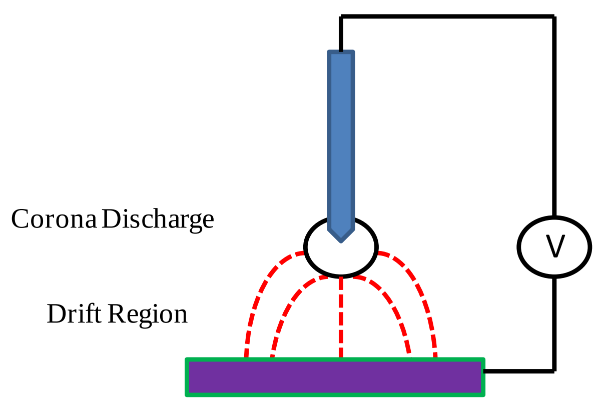

Figure 1.1; Schematic of a corona discharge configuration

A DC corona discharge in air at 1 atm produces currents in the range of micro- to milli-amperes operating at tens of kilovolts [1]. For higher currents, the voltage must be increased greatly leading to sparking and eventually arc formation. Higher currents and voltages can be obtained by using a pulsed power supply. If the pulse duration is less than the time required for spark formation, the discharge can be maintained in the glow or streamer regime.

In a dielectric barrier discharge (DBD), one or both electrodes are covered in a dielectric material that prevents the conduction current associated with sparks and arcs. The current is limited to the displacement current ($\varepsilon dE/dt$) allowing for non-equilibrium plasma production, where ε is the permittivity of the dielectric material and dE/dt is the time rate of change of the electric field. Most DBDs are filamentary discharges composed of many short lived streamers which occur when an electron avalanche reaches the anode and the charge propagates back towards the cathode. A DBD can also be operated in the glow regime; however a detailed explanation of this mode in DBDs is not very well known [2]. It depends on many variables such as the plasma working gas, applied voltage, and operating frequency. The DBDs are generally operated in the Hz to kHz range. Schematics of parallel plates and coaxial DBD configurations are shown in Figure 1.2.

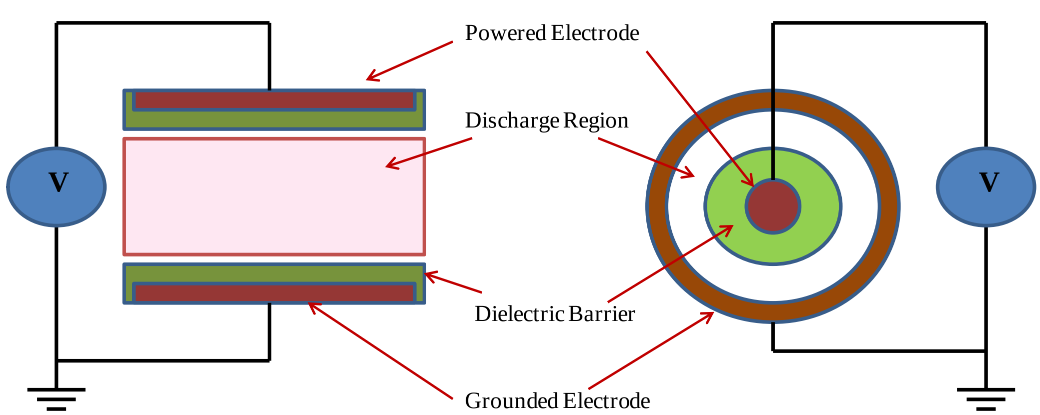

Figure 1.2; Schematic of a parallel plate (left) and coaxial (right) DBD

Microwave plasma discharges are electrodeless and plasma generation is due to wave excitation in a standing microwave in a resonator cavity. The microwave travels in wave guides and transmits energy to the electrons. Due to their mass, the heavy particles are only slightly heated. Ionization occurs through collisions and direct electron energy gain from the microwaves. A schematic of microwave-induced plasma is shown in Figure 1.3.

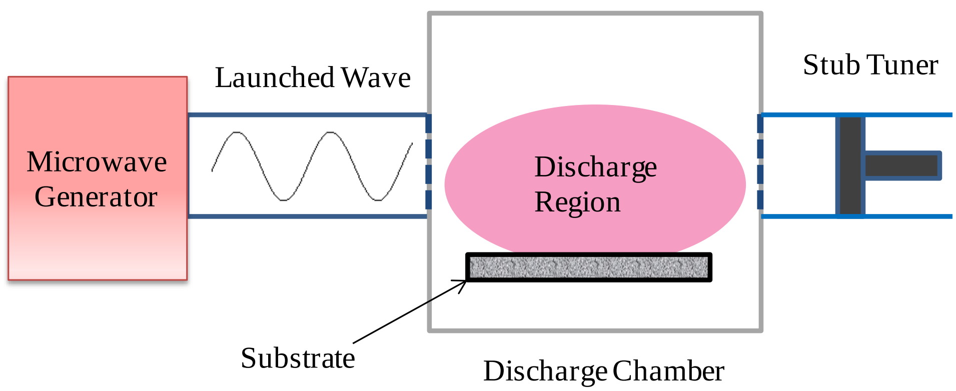

Figure 1.3; Schematic of a typical microwave induced plasma discharge

Atmospheric pressure plasma jets are operated at radio frequencies (13.56 MHz and its harmonics). They can be operated with a dielectric barrier, but it is not always required. In most cases, they consist of concentric electrodes with the powered electrode in the center and the outer electrode is grounded. They do not require the high voltages associated with corona discharges and DBDs and can be operated in the hundred volt range. Because of the configuration, the substrate is not placed between the electrodes, but a grounded electrode may be placed behind the substrate to increase the extent of the plasma onto the substrate. A schematic of an atmospheric pressure plasma jet is shown in Figure 1.4.

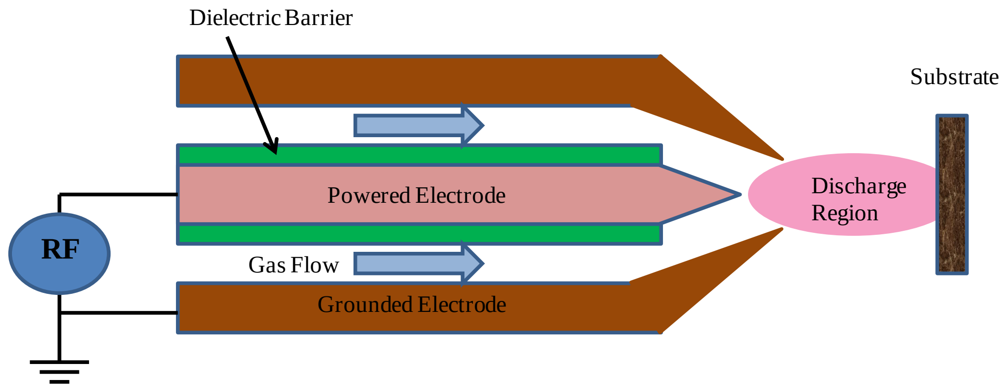

Figure 1.4; Schematic showing the features of an atmospheric pressure plasma jet

Substrates can also be treated on the edge of discharges or in the afterglow where only radicals remain. This can be very effective for surface treatments because in many cases, the radicals are the species driving treatment mechanisms such as chemical etching, oxidation, sputtering, deposition and surface activation. Treatment downstream from the plasma discharge can also allow for geometries not possible otherwise. Substrates can be belt-fed past the discharge for quick treatments. In the case of combining electrospinning and plasma treatment, the electric field of the plasma can interfere greatly with the static electric field required for electrospinning. Also, because of the nature of fibers being electrospun, the physical presence of the electrodes can be a hindrance as the fibers can collect on them instead of collecting on the substrate.

1.2 Electrospinning of Polymer Nanofibers

Polymer nanofibers can be produced through multiple techniques other than electrospinning such as drawing, template synthesis, phase separation, and self-assembly. These four processes have glaring drawbacks when compared to electrospinning. Some of them can only be used for certain polymers, others do not allow for the control of fiber diameters, and none of them can be scaled up for mass production. They all produce fibers ranging in length from a few microns to 20 microns whereas electrospinning can produce fibers from several centimeters to a few meters in length. This allows electrospun nanofibers to be used in several more applications than nanofibers produced using other methods.

The electrospinning of nanofibers must start with a polymer in liquid form. Polymers may either be melted or dissolved in a solvent. Polymer solutions are much more common than polymer melts for a myriad of reasons [3]. Polymer melts require high temperatures (>200° C) and larger electric fields. Polymer melt electrospinning also results in larger diameter fibers [4] which can be counteracted somewhat by electrospinning in vacuum. Another disadvantage of melt electrospinning is that thermoplastic polymers must be used whereas thermoset polymers may be used in solution spinning. The viscosity and surface tension of the electrospun fluid can also be controlled more easily in a solution form. Because of these disadvantages, research in melt electrospinning has been limited [4]. For these reasons, this section focuses mainly on polymer solution electrospinning.

1.2.1 Electrospinning Process

The electrospinning of polymer fibers is actually straightforward in its simplest form. It requires an electric potential, positive or negative between a conductive polymer solution and a substrate onto which the fiber is to be collected/deposited. It can be placed on the polymer (extruding the polymer away from itself because of electric repulsion of like charges), on the substrate (pulling the polymer toward it through electric attraction of opposite charges), or a combination of both. Figure 1.5 shows a typical electrospinning configuration.

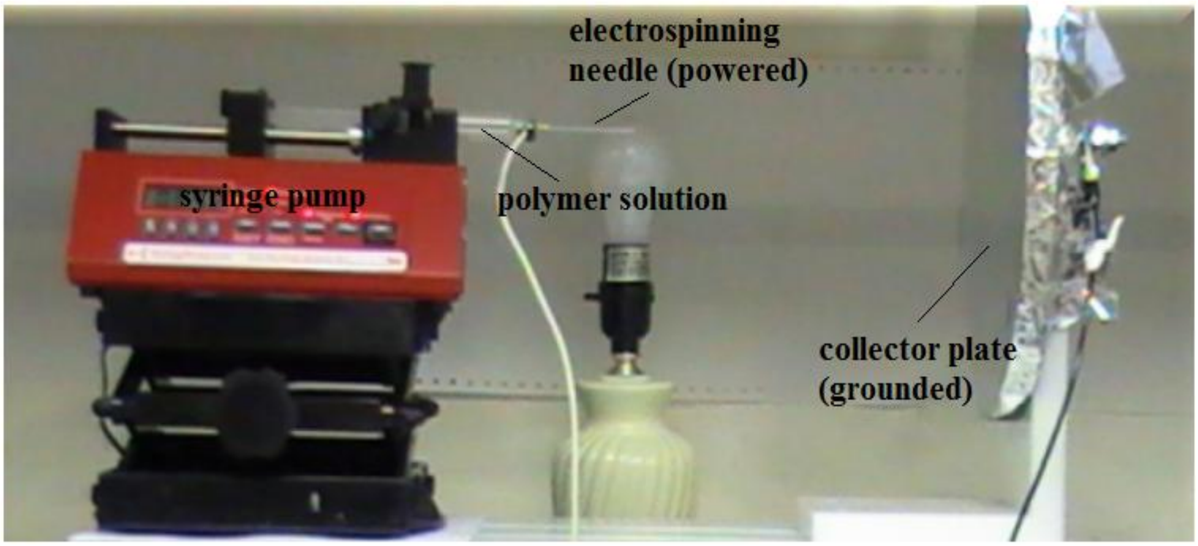

Figure 1.5; A typical laboratory electrospinning arrangement, the lamp is not part of the arrangement and was only placed to help taking the picture of the electrospun fibers

This differential electric potential will cause a Taylor cone to form on the end of a liquid droplet and a thin jet of solution to be drawn from the droplet. As the jet is drawn by the electric field, a critical point is reached at which the repulsive electric force becomes greater than the surface tension of the liquid. At this point, the jet will spread into multiple jets. These jets are drawn even thinner as they whip around towards the substrate. The polymer will solidify in transit from the bulk to the collector as the solvent evaporates. Figure 1.6 shows the features of a liquid being drawn into multiple jets.

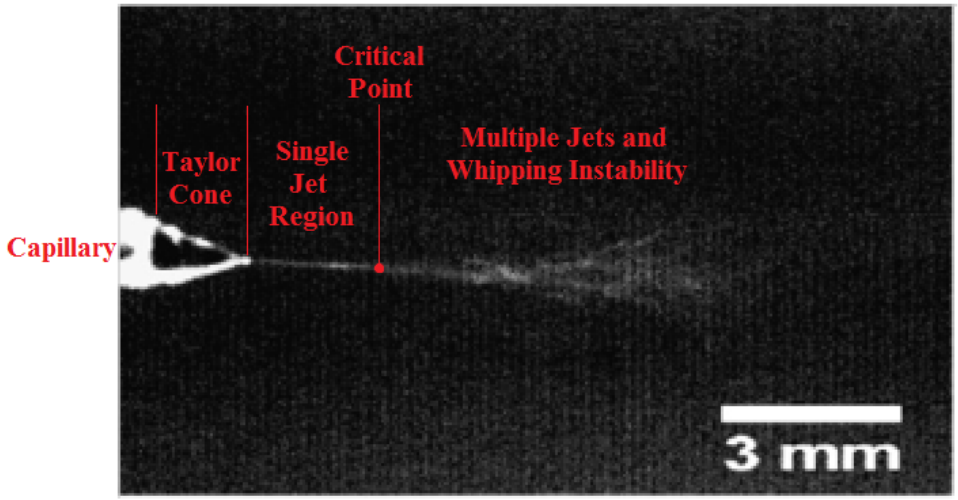

Figure 1.6; Details of electrified liquid behavior during electrospinning

1.2.2 Electrospun Fiber Size

There is a trade off that must be taken into account when performing electrospinning. Fiber diameter can only be decreased to a certain point at which polymer beads will form. If fiber diameter is further decreased, the electrospinning process will stop and electrospraying will begin and films will be produced on the substrate instead of fiber mats. There are many factors affecting the diameter of the electrospun fibers, including needle to collector distance, solution flow rate, applied voltage, solution concentration (viscosity and surface tension), and solvent volatility [5-7]. Multiple studies have been performed showing how these parameters affect electrospinning. For example, as needle to collector distance increases, fiber diameter will decrease to the point at which fibers will produce beads (solidified polymer droplets within the fibers) [5-8]. Fiber diameter will decrease as solution concentration decreases. Again, this is only to a certain point at which bead formation will dominate [5-7,9]. As voltage is increased, fiber diameter will decrease, but again only to a certain point above which bead formation is predominant [5-7]. These complexities can be problematic if the fiber diameter is to be controlled. They also provide a solution to uniform issues if the parameters can be accurately controlled. That is to say, these parameters can be used to tune relatively uniform fiber diameters [5-7,9-11]. Using these parameters, nanofibers with diameters of 50-900 nm are routinely spun into mats and diameters as low as 3 nm have been reported [12]. Because of these small fiber diameters, electrospun nanofibers have been considered for many applications.

1.3 Applications of Atmospheric Plasma in Surface Modifications

1.3.1 Surface Functionality

Changes in the surface functional groups are the important outcomes of any surface treatment and of importance when the treatment is processed with the aid of atmospheric plasmas. Surface activation for the purpose of polymeric grafting and polymer film deposition and coatings is discussed. Changes in wettability are also of principal focus and include enhanced dyeability and adhesion, as well as adhesion due to blank dyeing. Many of these effects can also be attributed to etching mechanisms, however, the dominant mechanism is the change is functional surface groups.

1.3.1.1 Wettability

Changes in the wettability of fabrics can be achieved in many ways. Increased surface roughness allows for water to be more easily drawn into fabrics. Functional groups, however, play the largest role in terms of wettability. A reduction in hydrophobic functional groups (alkyls, fluorine groups) or incorporation of hydrophilic functional groups (carbonyl, carboxyl, hydroxyl, amino, amido, aldehyde) will increase the wettability of a fabric, and the converse is of course true. These groups can be created or destroyed by etching, deposition, and chemical exchange. All have been used to varying degrees to change the wettability of textiles. They are often used in conjunction with each other but can also be competing processes producing and destroying functional groups depending on the plasma conditions.

1.3.1.1.1 Hydrophilicity

Plasma treatments aimed at improving wettability have been performed on all possible textiles. Increased hydrophilicity can be its own end, but it serves a somewhat more important goal. Increased wettability is an indication of increased surface energy and incorporation of polar functional groups. This allows for better bonding to substrates, dyes, printing inks, coatings, and adhesives [12].

Synthetic polymers, used in textiles manufacturing, often lack polar functional groups and the addition of these hydrophilic groups is often desired. Leroux et al. [13] used an atmospheric pressure air dielectric barrier discharge (DBD) just above the audio frequency range (26 kHz) to treat poly(ethylene terephthalate) (PET) woven and non-woven fabrics. They were able to decrease the water contact angle from 80º down to 50-40º on both woven and non-woven fabrics. They also observed an increase in the capillarity of the textiles as well as a slight increase in surface roughness through Atomic Force Microscopy (AFM) technique. It was proposed that the increase in wettability was due to surface oxidation. An atmospheric pressure plasma was blown onto the surface of a PET film and a silicone film for relatively short periods of time (0.1 – 10 s). The plasma was produced in atmospheric air by a DC power supply in both the glow and streamer regimes. The water contact angle was measured on the PET film showing a decrease from 77º down to 38º for the glow regime and 25º for the streamer regime. The silicone showed a drastic decrease in contact angle in the streamer regime. It dropped rapidly from >100º to <5º in treatment times greater than 1s [12]. Karahan and Ozdogan [14] used atmospheric pressure air and Argon DBD plasmas to increase the wettability of raw cotton fibers. They observed an increase in the wicking height and surface roughness as well as a decrease in contact angle for fabrics treated with either plasma. The proposed mechanism for increased wettability was the destruction of the hydrophobic layer present on raw cotton fabrics accompanied by an increase in surface oxygen content.

1.3.1.1.2 Hydrophobicity

Increased hydrophobicity is important in protective garments and water repellent textiles for outdoor use. Producing enhanced hydrophobicity usually requires wet chemical processes that are water intensive. Plasma treatments have been shown to either decrease the need for water in the chemical processes or eliminate the need for water with direct addition of hydrophobic functional groups. Most of the treatments are centered on surface fluorination of the substrate. To date most of the research that has been done in this field has been at low pressures below atmospheric. Therefore, there is little literature on atmospheric pressure plasmas in this area. However, the research conducted by de Geyter et al. [15]

successfully incorporated fluorine on the surface of PP films at atmospheric pressure with a He/CF_4 (95/5) plasma. XPS analysis showed up to a 45% fluorine concentration on the surface of the films with a treatment time of only 5 s. This was shown in water contact angle measurements as well increasing from 90.8º up to 118º. Choi et al. [16] also used a DBD of He and CF_4 to fluorinate the surface of PP films (up to 47% F on the surface). The water contact angle was increased from ~75º to slightly above 90º. XPS showed that most of the carbon (1s) peaks on the surface were, in fact, CF_3 and CF.

The surface of polyamide 6 films has also been fluorinated using a He/CF_4 discharge. Gao et al. [17] used an atmospheric pressure RF plasma jet to blow the He:CF_4 (~99:1) plasma onto the surface of the films. Ho et al. [18] fluorinated carbon fibers to increase hydrophobicity by using chlorodifluoromethane (Freon 22) as the working gas diluted in N_2. The plasma was again blown on to the fiber surface. The water contact angle increased drastically from 81º to 103º. There was also an increase in contact angle for di-iodomethane (DIM) from 30º to 56º and for formamide from 38º to 57º. There was no change in bulk fiber properties.

1.3.1.2 Adhesion

Adhesion of polymer fibers to epoxy is not generally researched in the field of textiles, but it is very important when creating fiber composites. Qiu et al. [19] treated ultrahigh modulus polyethylene fibers in an atmospheric pressure DBD He/O_2 (99/1) plasma at 7.5 kHz. Treatment times ranged from 30 – 120s. SEM images showed etching in the form of surface micro cracks. The authors showed a large increase in carboxyl and hydroxyl groups on the fiber surfaces with XPS analysis, where these groups apparently replaced the alkyl groups usually present. The interfacial shear strength between the fibers and an epoxy was examined, and a large increase in adhesion was shown with no significant change in fiber tensile strength. Kusano et al. [20] strengthened a more conventional fiber composite with a dielectric barrier helium discharge. They reported an improvement in adhesion to the epoxy resin yielding a stronger carbon fiber composite. The increased adhesion was attributed to the generation of carbonyl groups on the surface. They also introduced this functional group to the surface of carbon fibers with He/O_2 and Argon plasmas. They, however, did not make composites from these fibers and hence the adhesion strength is unknown.

Plasma treatment has also been shown to improve bond strength with adhesives. Lommatzsch et al. [21] used a low frequency (17 – 22 kHz) plasma jet with N_2 or dry air as the working gas to increase the surface oxygen content of polyethylene sheets. They reported a large decrease in water contact angle as well as a 300% increase in bond strength with methacrylate adhesive. Park et al. [22] also increased adhesive bonding strength through the incorporation of surface functional groups. They treated styrene butadiene rubber in a RF plasma jet of either He/O_2 or $Ar/He/N_2$ gas mixtures. They reported an increase in the oxygen and nitrogen surface content leading to bond strength with polyurethane adhesive (up to 3.5 kgf/cm). This is important because there was no measurable bond strength without treatment.

Functionality can also be imparted through adhesion. Kan et al. [23] used printing pastes containing antimicrobial polymers (sodium alginate, chitosan, and sodium alginate-chitosan mixture) to print on cotton fabrics. They used a RF plasma jet of He/O_2 to pre-treat samples before printing. While all showed good antibacterial properties (control and plasma treated), plasma treated samples showed better adhesion and resistance to washing. Nanoparticle adhesion has also been examined. Gorensek et al. [24] used a coronal air discharge to increase Ag nanoparticle adhesion on PET fabrics. After plasma pretreatment, the fabrics were blank dyed with a dye containing Ag nanoparticles, and there was a marked increase in Ag concentration on the treated fabrics. Untreated fabrics contained only 3.9 mg Ag/kg PET while treated fabrics showed 93 mg/kg. As a consequence, the treated fabrics displayed much better antibacterial properties.

1.3.2 Etching

Low temperature atmospheric pressure plasmas do not etch through physical mechanisms such as surface bombardment. The etching mechanism is of a chemical nature, i.e. neutral radicals interacting with the surface. With the development and use of solid state electronic devices, the etching and machining of the materials used in these devices has become highly researched. Mori et al. [25] developed a method of etching these materials in atmospheric pressure plasmas. Fluorine containing gases such as SF_6 and CF_4 (5-10%) were added to helium discharges. The discharge (RF) was limited to the area just outside the electrodes and the mechanism was due to the interaction of neutral fluorine radicals with the surface. They were able to etch silica, molybdenum, tungsten, silicon carbide, and diamond.

The addition of O_2 to the discharge aided in the production of fluorine radicals through oxidation of S and C. Sano et al. [26] were able to bevel the edges of a silicon carbide wafer using a similar method. The edges were rounded uniformly without damaging the wafer itself. Tu et al. [27] achieved good etching downstream from a RF O_2, CF_4, He plasma. This downstream method again shows that the mechanism is due to neutral radicals as ionized species quickly recombine outside the discharge volume. The etching mechanisms of APP are not limited to solid state electronic materials. The effects of atmospheric pressure plasmas on wool were examined by Karahan et al. [28], where they used Ar and air dielectric barrier discharge plasmas at 13 kHz to treat the fabrics for 20 – 60 s with observed significant anti-pilling effects. This effect was attributed to etching that decreased the wools abrasion resistance. This is one example of textile etching, and other examples are included in the section on surface functionality.

1.3.2.1 Surface Cleaning

Surface cleaning may not be generally considered an etching effect. However, the cleaning of surfaces using APP utilizes the same mechanisms as the etching of surfaces. The only difference is that in the cleaning process, impurities on or in the substrate are the targets of etching instead of the substrate itself. The cleaning of metal surfaces through the removal of impurities has been investigated using APP. Thiebaut et al. [29] used $Ar:N_2$ (99:1) discharges to remove the impurities from iron sheets. They used a direct DBD and a downstream method using a microwave discharge. The two methods were comparable and showed good removal of carbon impurities. Goosens et al. [30] have shown better results for removing metal impurities using a He:H_2 (95:5) DBD (1-4 kHz). They successfully reduced the oxygen surface concentration in Cu due to interaction between the oxygen and hydrogen. Their results were even better for the destruction of the Ag_2S layer on Ag sheets, and the impurities were completely removed. The mechanism was verified as a neutral radical process by measurement of significant amounts of H_2S in the reactor exhaust. Jung and Choi [31] used Ar/O_2 and He/O_2 DBDs to remove the photoresist layer from a silicon wafer in which the wafer was placed downstream of the discharge. Both discharges showed good etching rates. The proposed mechanism for removal was chemical etching due to atomic oxygen.

Cleaning is not limited to inorganic surfaces. APP can also be used to remove impurities from fabrics. Desizing of polyvinyl alcohol (PVA) on cotton is usually achieved with hot and cold washings or a hydrogen peroxide (H_2O_2) treatment. Cai et al. [32] utilized both air/He and air/He/O_2 audio frequency dielectric barrier discharges to enhance the desizing of PVA on cotton. Both plasmas were able to remove ~20% of the PVA size from the cotton fabrics. This is well below the ability of traditional desizing techniques. However, when combined with cold and hot washing, 99% of the size was removed. This is much higher than washing alone. It was also higher than the desizing achieved with H_2O_2 (93%) and did not require the use of chemicals. Fabric strength was not only unhindered by the treatment, in some cases it was increased.

1.3.2.2 Polishing

Because plasma etching will preferentially occur on protrusions from a surface, it can be used as a polishing technique. Wang at el. [33] have used the fluorine radicals downstream from a capacitive RF discharge to polish the surface of SiC optics. The radicals were blown onto the surface selectively etching the protrusions through the formation of SiF_4 vapor; sub-nanometer roughness was obtained. Even harder materials can also be polished. Using a very low frequency (60 Hz) discharge in air Detrick et al. [34] were able to polish diamond films. The proposed mechanism was reaction of atomic oxygen and ozone with the diamond surface. It is clear that the main etching mechanism for low temperature atmospheric pressure plasma is neutral radical chemistry.

1.3.3 Surface Coatings

1.3.3.1 Plasma Enhanced Chemical Vapor Deposition "PECVD" via Atmospheric Plasmas

In PECVD, the film precursors are added to the discharge. The plasma creates a chemically reactive environment to activate the precursors and surface to allow for deposition of thin films. Deposition can be used to change surface properties without affecting the bulk properties of the material. Korotov et al. [35] deposited SnO_x onto glass substrates to create a film with high optical transparency and good electrical conductivity. They added organotin vapors to nitrogen or air plasmas yielding SnO_x films on the surface of the glass. The films were not soluble in water or organic solvents, and good adhesion was obtained. Other metal oxides have been deposited for their unique properties. TiO_2 is an excellent photocatalyst as well as having photo-induced super hydrophilicity. Zhang and Han [36] used a gas mixture of N_2O, $TiCl_4$, and He in a low frequency (<20 kHz) DBD to deposit the TiO_2 films onto glass substrates. The films showed the increase in hydrophilicity in the presence of UV.

Foest et al. [37] deposited thin silicon organic films on aluminum for surface protection. Hexamethyldisiloxane (HMDSO) vapor was added to a dielectric barrier helium discharge. The films showed good adhesion and good protection of the Al sheets against NaOH. HMDSO has also been used as a film precursor to deposit hydrophobic SiO_x coatings onto cotton fabric. Again the HMDSO vapor was added to a dielectric barrier helium discharge. The films showed good adhesion and the water contact angle was significantly increased (~95 up to 135°) [AP6]. The film precursor may also be a monomer which is deposited and polymerized directly on the surface. Morent et al. [39] added acrylic acid monomers to a dielectric barrier argon discharge yielding polyacrylic acid films on sheets of polypropylene. Uniform polyacrylic acid films were obtained. Deposition of carbon nanotubes (CNTs) has also been examined in atmospheric plasmas [40]. Using a glow discharge of $He/H_2/CH_4$ uniform CNTs were grown on Ni-coated quartz substrates. Deposition can also be achieved through aerosol injection into the discharge. The UV resistance of cotton fabric was improved significantly by Jiang et al. through sericin deposition. An aqueous sericin solution was sprayed into a helium glow discharge operating at low frequencies (20-30 kHz). The sericin was polymerized on the surface and attached to the cotton with covalent bonds. The water uptake of the cotton fabric also increased [41].

1.3.3.2 Surface Activation

In textile applications, plasma is often used to activate the textile surface for grafting polymers. The textile is then either exposed to plasma for deposition or placed in a solution containing the chemicals to be deposited. Deposition of hydrophilic films was examined by Hossain et al. [42]. PET fabrics were treated in Ar/O_2 (ratio of 4/1) and ammonia/acetylene (NH_3/C_2H_2) or ammonia/ethylene (NH_3/C_2H_4) plasmas in order to deposit the films. The fabric surface was first activated in the Ar/O_2 plasma. The films were then deposited in either NH_3/C_2H_2 or NH_3/C_2H_4 plasmas. Both showed good film deposition and complete wettability (contact angle went from ~80º down to 0º). Yaman et al. [43] improved the dyeability of PP fabrics with soluble dyestuffs. They used a DBD Ar plasma to activate the textile surface then grafted five different polymers in aqueous solution to the activated fabric surfaces. All polymers were successfully grafted.

The above treatments center on increasing the hydrophilicity of the textile. However, the surface coatings can have many different effects on surface functionality. Bai and Liu [44] used atmospheric pressure DBD Ar plasma to graft dimethyl diallyl ammonium chloride (DMDAAC) monomers to the surface of polyacrylonitrile (PAN) fibers to improve antistatic properties. The fibers were immersed in an aqueous solution of DMDAAC and then plasma treated to graft the monomer to the fiber surface. The grafting was confirmed with SEM and XPS showing a new surface layer and the presence of Cl surface groups (present in DMDAAC), respectively. The wettability and antistatic ability were shown to drastically improve. Textiles can also be made antimicrobial through the grafting of polymers as shown by Tseng et al. [45]. The authors used an atmospheric pressure air plasma jet to activate the surface of nylon6,6 fabric. The fabric was then immersed in an aqueous solution of chitosan oligomer. The grafting was successful and the fabrics showed good antibacterial character. The fabrics also showed no cytotoxicity. This shows that the fabrics remained biocompatible making them a good candidate for medical applications, especially in the field of wound dressings.

1.4 Barrier Applications of Electrospun Nanofibers

1.4.1. Filtration

Electrospun nanofiber webs have been shown to have excellent filtration properties. The small pore size and large surface area allow for the filtering of particulates and aerosols while the small fiber diameters coupled with the large concentration of pores can be used to prevent the large pressure drop associated with high efficiency filters. Unfortunately, nanofiber webs have little structural strength and must be deposited on a substrate that provides strength to the web.

Companies like Donaldson and DuPont incorporate electrospun nanofibers into commercially available filtration systems because of the large increases in filtration efficiency without greatly sacrificing air permeability [46]. In fact, electrospun nanofibers have been used in commercial filtration systems for over 20 years. One example of the ability to greatly increase filtration with a very low density of nanofibers is shown in the research done by Patanaik et al. [47] in which they electrospun nanofibrous membranes from polyethylene oxide (PEO) in solution. The nanofibers were deposited on a polypropylene

(PP) needle-punched nonwoven fabric. They tested the filtration efficiency of the composites using dust particles in air ranging in size from .6-180 µm in diameter. The filtration efficiency was increased from 63% for the nonwoven fabric alone up to >99% with the addition of 0.4 g/m^2 of nanofibers (the area weight of the nonwoven alone was 95 g/m^2). The pressure drop across the filter rose from 12 to 17 Pa, a large percentage increase but still very low. Nanofiber mats have also been studied for liquid filtration. Polyvinylidene fluoride nanofibers were shown to remove 96% of 10µm polystyrene particles from water without loss of flow. Also 98% of 1µm particles were removed but with a large increase in pressure drop [48]. Copper(II) has also been filtered from water with nanofiber mats through micellar-enhanced filtration showing excellent filtration (74% removal) [49]. Shin et al. [50] mixed recycled polystyrene nanofibers with glass microfibers to enhance the coalescence filtration of water from oil. They were able to increase the filtration efficiency of the glass from 67 to 88%.

The focus of this research is the development of protective clothing. Therefore, the focus of this section is on those who have examined the filtration efficiency of electrospun nanofibers for the specific purpose of aerosol particle filtration for protective clothing. Gibson et al. [51] tested the filtration of potassium iodide particles (2-3µm) through nylon 6,6 nanofiber webs. They were able to achieve no particle penetration above fiber areal densities of 1 g/m^2. This led to a large convective flow resistance when compared to normal clothing materials. However, there was almost no change in water vapor permeability, thus allowing evaporative cooling to take place through the clothing without loss in aerosol protection. Smaller more penetrating particles have since been used to challenge nanofiber protection. Qin and Wang [52] deposited poly(vinyl alcohol) (PVA) nanofibers onto two different PP nonwoven substrates (spunbonded and meltblown). They used 600 nm NaCl particles in air to test the filtration. The filtration efficiency was increased from 30% and 6% (meltblown and spunbonded) to 100% and 95% respectively at areal densities of 2.9 g/m^2, where it was seen that the pressure drop increased significantly. This is not always the case though. It has been shown that 300 nm particles are the most penetrating in terms of filtration. Vitchuli et al. [53] were able to filter >99.5% of NaCl particles of this size with minimal change in pressure drop and no change in air permeability. They were able to electrospun nylon 6 fibers onto a standard military test fabric (50/50 nylon/cotton woven).

Nanofiber mats have also shown potential as molecular filters for biomolecules. Uyar et al. [54] electrospun solution mixtures of polystyrene (PS) and beta-cyclodextrine. The nanofiber mats were able to trap 63% of the phenolphthalein from a solution in 72 hrs. This is, of course, a very long time for filtration, but it shows good potential for developing filtration mats. Others have functionalized nanofiber mats with Cibacron Blue F3GA, a general affinity dye ligand for proteins [55,56]. Both showed high adsorption capacity for the specific proteins used.

1.4.2 Liquid Repellency

Filtration is one of the properties of nanofibers that make them attractive for protective clothing applications. They can also be excellent barriers to liquid penetration, stains and blood for surgical gowns. One of the most commonly used methods to determine liquid repellency is the measurement of contact angles with various liquids. The most commonly used liquid is water but various oils are used to measure increased repellency because of the low surface energies that they possess. Electrospun nanofibers can be made to display higher liquid repellency than fabrics or films of the same polymer. For example, the water contact angle (WCA) of polypropylene (PP) nanofiber mats has been measured at 151°, much higher than a commercial nonwoven PP fabric with a contact angle of 104° and a PP film at 112° [57]. Hydrophilic films of poly(D,L-lactide) and poly(D,L-lactide)-poly(ethylene glycol) with contact angles of 76.4° and 70.1° were made hydrophobic through electrospinning (WCAs of 132.2 and 114 respectively) [58]. Other polymers such as poly(styrene-b-dimethylsiloxane) [59] and poly(ε-caprolactone) [60] have also been made extremely hydropohobic through electrospinning.

Water, and various oils, contact angles of nanofiber mats have been studied by several researchers displaying good applicability to protective clothing. Cenzig et al. [61] electrospun a terpolymer containing perfluoroethyl alkyl methacrylate. The nanofiber layer was found to be superhydrophobic with a water contact angle of 172°. It was also superoleophobic for glycerol (167°) and ethylene glycol (163°). In the case of hexadecane it showed a resistance to spreading but the contact angle was only 70°. These results were expected because of the very low surface tension of hexadecane. Ma et al. [62] combined electrospinning with chemical vapor deposition to produce oleophobic fabrics. They electrospun PCL nanofiber mats which were then coated with a thin layer of perfluoroalkyl ethyl methacrylate. The resulting nanofiber mats displayed a water contact angle of 175° as well as oleophobicity with respect to decane, octane, and heptane (contact angles of 118°, 109°, and 92° respectively). Han and Steckl [63] coaxially electrospun Teflon and poly(ε-caprolactone) (PCL) as the sheath and core respectively. The nanofiber mats were shown to be superhydrophobic with a contact angle of 158° and a water rolling angle of 5°. Oleophobicity was shown with contact angles greater than 120° for (in order of increasing surface tension) decane, dodecane, hexadecane, butylbenzene, methylpyrrolidone, ethylene glycol, and glycerol. In fact, they also showed superoleophobicity for glycerol with a contact angle above 150°. The only oil that soaked into the surface was octane. These results are important in the field of protective clothing because similar surface tensions are indicative of similar contact angles. The surface tensions of liquids used in contact angle measurements are shown in Table 1.1 along with the surface tensions of liquid/aerosol chemical warfare agents.

Table 1.1; Surface tensions of liquids used for contact angle measurements and chemical warfare agents (shown in bold)

Liquid	Surface Tension (dynes/cm)		Liquid	Surface Tension (dynes/cm)
Water	72.8		n-hexadecane	27.47
Glycerol	64		**GB Sarin**	**26.5**
Ethylene glycol	47.7		n-dodecane	25.35
HD Sulfur Mustard	**43.2**		**GD Soman**	**24.5**
Methylpyrrolidone	40.79		n-decane	23.83
VX	**32.01**		n-octane	21.62
Butylbenzene	29.23		n-heptane	20.14

Penetration of liquids through nanofiber mats and composites have also been studied. Sahu et al. [64] studied the penetration of water droplet impacts on nanofiber membranes. They were able to produce nylon 6,6, PAN, and PCL nanofiber mats that prevented water penetration at impact velocities up to 3.46 m/s (the highest velocity tested). Bagherzadeh et al. [65] showed similar results for PAN nanofiber mats sandwiched between woven fabrics (material not mentioned) using a Bundesmann rain-shower test. They were able to decrease the water passing through the fabric composite from 215g (for the woven fabrics alone) down to 90g. This was coupled with no change in water vapor permeability, again a desirable quality for protective clothing. Cho et al. [57] studied the barrier properties of PP nanofibers deposited on nonwoven PP fabrics, and have shown that the water contact angle could be increased up to 151°. They also studied the penetration of pesticide/water mixtures through the composites In which it was shown that after the addition of the nanofiber layer pesticide repellency increased from 3% up to 56% and pesticide penetration fell from 83% down to 9%. Lee and Obendorf [66] also examined the ability of electrospun nanofibers to limit the penetration of pesticides. They deposited polyurethane nanofibers on PP spunbonded fabrics. They used mixtures of pesticides and water with surface tensions as low as 20.57 dynes/cm. In the most penetrating case (20.57 dynes/cm), the nanofiber mats were able to decrease the penetration from >85% (substrate alone) to below 25% (2g/m^2 nanofiber density). Again, there was no change in water vapor permeability.

1.4.3 Antimicrobial / Detoxification

Protective clothing is even more effective if it not only prevents the threat from reaching the wearer but also eliminates the threat once stopped. To this end, researchers have attempted to produce nanofiber barriers that are antimicrobial and able to detoxify chemical agents. The majority of this research has surrounded the addition of nanoparticles to the nanofiber mats.

Silver nanoparticles have shown excellent antibacterial properties. Park et al. [67] electrospun a suspension of silver nanoparticles in nylon 6 solution. The nanofibers displayed excellent antibacterial properties reducing the growth of Gram positive (S. aureus) and Gram negative (K. pneumoniae) bacteria by 99.9%. Shi et al. [68] also used a suspension of silver nanoparticles but used PAN as the polymer. They also saw excellent antibacterial properties showing the complete inhibition of growth for Gram positive (B. cereus) and Gram negative (E. coli) bacteria. Others have used metal oxide nanoparticles to functionalize their nanofibers. Such as TiO_2 which was electrospun in nylon 6. The nanofiber mats were able to kill all E. coli present within 2 minutes in the presence of UV (necessary to activate the TiO_2 nanoparticles). This displays the ability to not only inhibit growth but to kill existing bacteria [69]. Vitchuli et al. [70] simultaneously electrospun nylon 6 onto cotton/nylon woven fabrics while electrospraying ZnO. The nanofiber mats inhibited the growth of 99.99% of both Gram positive (B. cereus) and Gram negative (E. coli) bacteria. Not only were the nanofiber antibacterial, they were also showed excellent detoxifying efficiency against paraoxon (a stimulant for nerve agents). 95% of the paraoxon was detoxified within 15 min. The fabrics showed no change in water vapor transmission with the addition of the nanofiber mats. Paraoxon has also been detoxified using MgO nanoparticles in polysulfone (PSU) nanofibers. The nanofibers were 2 times more reactive than commercially available activated charcoal when detoxifying the paraoxon [71]. Ramaseshan and Ramarishna [72] produced zinc titanate nanofibers that were able to detoxify paraoxon and CEES (a stimulant for sulfur mustard agents) without the addition of nanoparticles. They were able to detoxify 91% of the paraoxon in 50 min and 69% of the CEES within 10 min. These detoxification rates are not ideal, but they do display the efficacy of zinc titanate nanofibers in protective applications.

Chapter 2: Hybrid Atmospheric Plasma – Electrospinning

It has been shown that atmospheric plasma has advantages in surface modification and functionalization at ambient conditions. It is also well documents that electrospinning has attractive features in depositing nanofibers on mats. A hybrid system that combines an atmospheric plasma electrospinning has been developed to be used as a novel technique in the production of protective mats. This chapter describes the hybrid atmospheric plasma-electrospinning system, theory, experiment and applications.

2.1 Theory of Hybrid Atmospheric Plasma – Electrospinning

Nanofiber mats have shown promise for protective clothing applications. They have shown excellent aerosol filtration [51-53] and liquid repellency [61-63]. They can also be made antibacterial [67-69] to combat biological weapons and have even shown the ability to detoxify chemical warfare stimulants such as paraoxon [70-72] and CEES [72]. The drawback is that polymer nanofibers lack structural strength. A solution to give the nanofibers structural strength is the deposition of nanofibers on fabric substrate; however, nanofibers do not adhere well to fabric substrates. They are easily abraded and peeled from the surface. Adhesion could be enhanced through wet chemical processes, but these processes can damage the nanofibers and are not environmentally friendly. A solution that could enhance adhesion and abrasion resistance is the use of atmospheric plasma to graft the nanofibers to the substrate and to each other.

Atmospheric plasmas have been used to activate surfaces for polymer and monomer grafting [42,43,45]. These experiments have focused on activating the substrate and grafting monomers and small polymer chains, but larger polymer chains can just as easily be activated for grafting. If the nanofibers can be activated while being electrospun, they will graft to the surface of the substrate as they are deposited, enhancing adhesion. They will also graft to each other giving the nanofiber mat greater strength and abrasion resistance. The purpose of this research is to use atmospheric pressure plasma to create a chemically active environment between the nanofibers being electrospun and the fabric substrate on which they are deposited. Specifically to create surface radicals as grafting sites on the nanofibers and the substrate.

2.2 Development of Experimental Hybrid Systems

There are two main challenges associated with the in-situ plasma treatment of electrospinning nanofibers. Because both plasma generation and electrospinning are electrical processes, they can easily interfere with each other's electric fields. Also, the whipping instability that draws the nanofibers to their small diameter leads to random deposition that is difficult to control. Therefore, the plasma source must be far enough from the collector to prevent deposition on the source and electrodes, but it must remain close enough to treat the nanofibers.

The most important aspect of the hybrid system design is to produce plasma at the same time electrospinning is occurring. The first design of a hybrid atmospheric plasma-electrospinning apparatus was to place electrospinning inside of a parallel plate dielectric barrier discharge in which the electric field between the parallel plates is almost uniform $|E| = \Phi / d$, where 'Φ' is the applied potential and 'd' is the distance between the two parallel plates. In this configuration the entire plasma box is equivalent to a capacitor $C = \varepsilon_p \left(A / d \right)$ with plasma filling, where 'ε_p' is the plasma permittivity and 'A' is the cross sectional area of the parallel plates. The experimental set-up was a modification of an existing plasma system (PALADIN), which is atmospheric plasma DBD device operating in the frequency range 1-12kHz [73]. It was found that if a pure helium (or close to pure) environment was used, which is the most adequate gas for plasma generation at atmospheric pressure, then the electrospinning voltage could not be maintained. A breakdown would occur between the needle tip and the collector, and the presence of the plasma provides a conductor path that short-circuits the electrospinning process.

A solution for this difficulty is to blow plasma into the electrospinning path thereby treating the nanofibers in the plasma afterglow. An audio frequency electrical system was designed and built for this purpose and was used on all subsequent designs. The details of this electrical system are given in Section 2.3. A series of plasma sources were designed and built to overcome both electrical and physical interference between the electric fields of the atmospheric pressure plasma and electrospinning. A summary of the prominent configurations is shown in Table 2.1.

The ring configuration 2a has provided producing plasma while simultaneously electrospinning, however, all of the nanofibers were collected on the plasma source without reaching the collector. When the plasma source was moved closer to the collector, most of the fibers were still collected on the plasma source, but a fraction was collected on the substrate in limited quantities and not with a reasonable thickness of nanofibers on the substrate. Configuration 3 allowed for a good collection area, however, the gas flow can be quickly blocked by nanofibers limiting the extent of the plasma treatment. With the addition of the rotating collector (a detailed description is given in Section 2.3), fibers could be collected in large enough quantities for testing while still being plasma treated.

Table 2.1; Summary of hybrid configurations and their success

No.	Hybrid Configurations		Atmospheric Pressure Plasma	Electrospinning
1	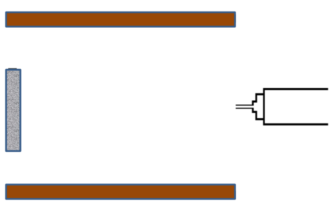		Easily obtained with high enough Helium concentration	Static breakdown occurs, high voltage cannot be maintained
2a	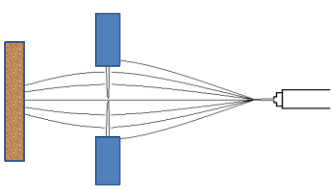		Easily obtained, limited extent	Do not reach the collector, collects on plasma source
2b	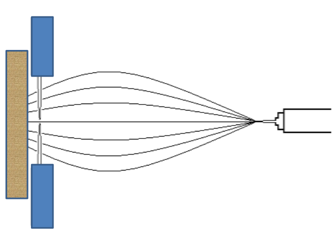		Easily obtained, limited extent	Most fibers collect on the plasma source, very small quantities of nanofibers on the collector

Table 2.1 Continued

3	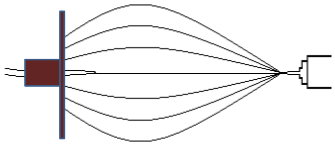 	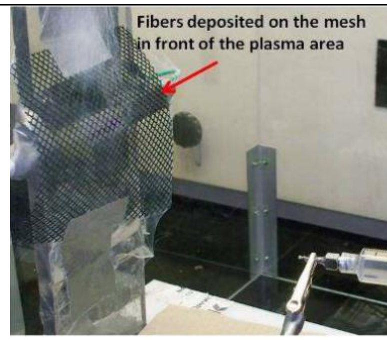	Easily obtained, limited extent	Fibers collect easily, quickly block gas flow, plasma becomes completely blocked
4a	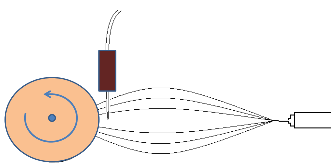	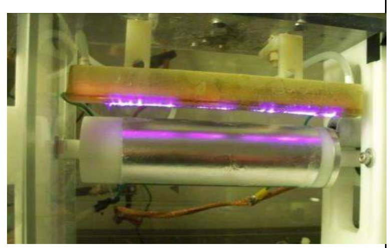	Easily obtained, limited extent, very inhomogeneous	Limited nanofibers collected on rotating collector
4b		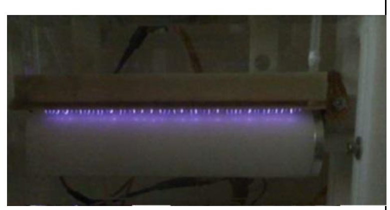	Same as above, more homogeneous treatment of nanofibers	Nanofibers collect easily on collector, some on plasma source

Configuration 4a has a continuous slit through which plasma is blown and the electric field is equivalent to the field generated by a point charge 'Q' thus $|E| = kQ/r^2 \cong 9\times10^9 Q/r^2$, where $k \cong 9\times10^9$ (N.m^2/C^2) for air, however, the plasma was very inhomogeneous along the length of the plasma source. It was found that the use of multiple holes led to an increased homogeneity along the source length. This final configuration 4b is the final successful design that was used for textile testing and plasma modeling. The features of this configuration are given in detail in the following section.

2.3 Optimized Hybrid System with Rotating Collector

The plasma source designed and built for the optimized hybrid system is a capacitively coupled dielectric barrier discharge. The dielectric barrier is garolite g10/fr4, a composite of fiberglass and epoxy. It was found that the extended use can ablate the epoxy in the plasma and the continuous operation can lead to a failure causing arcing. A simple addition to the design is the addition of a sheet of polyethylene as a protective layer on the garolite, which proven to be sufficient enough to prevent ablation and eliminate any failure that leads to arcing. A cross-section of the plasma source is shown in Figure 2.1.

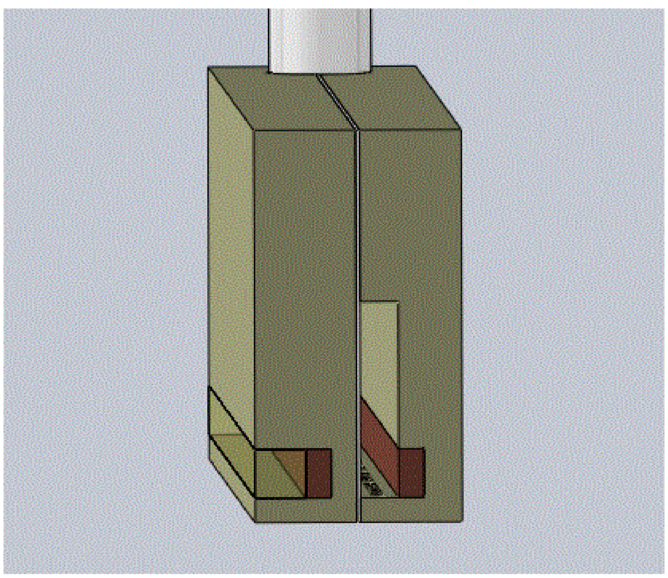

Figure 2.1; Cross-section of the hybrid plasma source

Table 2.2; Internal dimensions of the hybrid plasma source

Plasma Source	dimensions (in inches unless specified)		
	length	*width*	*thickness*
Electrodes	7	1/8	1/16
Discharge region	7	3/8	3/32
Garolite insulator			1/16
Polyethylene sheet			.25 mm
Holes (57 centered in discharge region)	*diameter* 1/32	*pitch* 1/8	

The exact dimensions of the plasma source are shown in Table 2.2. The electrode embedded in the dielectric is the powered electrode and the bare electrode is in common ground with the rotating collector. The plasma gas (either He or He/O_2 at 99/1) is introduced into the discharge region where it is excited, dissociated, ionized and then blown out of the holes to the bottom into the path of the nanofibers as they are electrospun by the electrospinning setup. Figure 2.2 illustrates the injection of the nanofiber solution into the plasma and collection on the rotating drum. In this final design, the electrospinning needle is approximately 15 cm from the rotating collector and powered by a high voltage DC source at 15kV. The electric system of the plasma source uses a TITAN hybrid switchmode AC power supply with built-in function generator operating in the frequency range 45 Hz – 15 kHz. The power supply can provide up to 8 Amp current in 2 switchable modes, 0-130 V or 0-260 V. The design can provide up to 12 kV, and higher, to induce breakdown in a dielectric-barrier discharge (DBD) at atmospheric pressure. The electrodes are coupled to the output of the 2 out-of-phase (180^{o} out-of-phase) transformers; each provides half of the required voltage. The design uses two AD6286 high voltage transformers, 10kV insulation; each has a step-up ratio of 1:125. The transformers are center-tapped to ground and the input leads are coupled to the source that provides variable frequency input at adjustable voltage. The output is coupled to a step-down transformer to adjust the output to a maximum of 110 V, which is the maximum allowable input to the out-of-phase transformers.

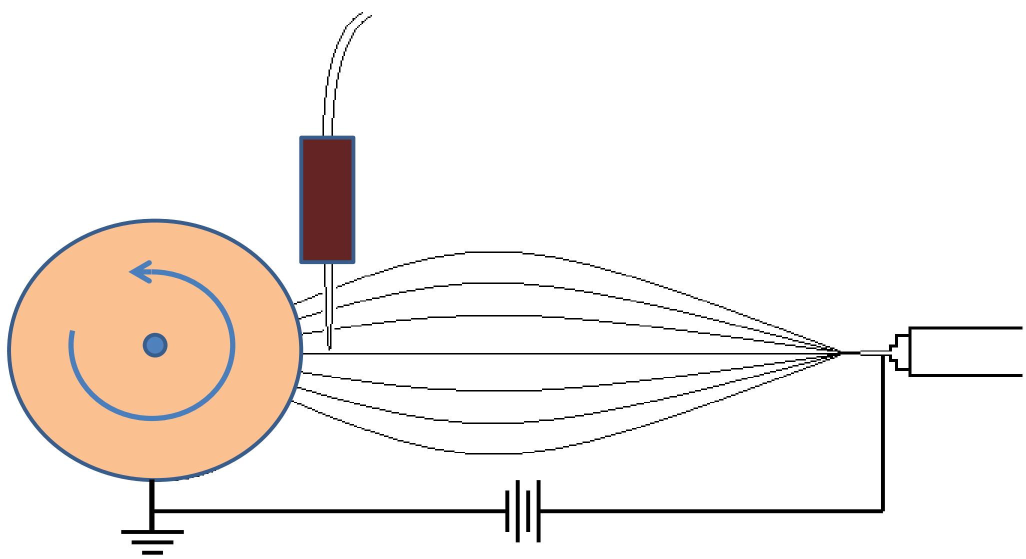

Figure 2.2; A schematic of the hybrid electrospinning system

The switchmode power supply provides 130V or 260V sinusoidal output at a selected pre-set frequency between 4 - 15 kHz, and the output is fed to the step-down transformer to adjust the output to 50V input to the out-of-phase transformers, which in turn will provide 6.25kV on each transformer output and hence the peak-to-peak voltage on the electrodes will be 12.5kV. Figure 2.3 shows the electrical circuit of the system in which the plasma discharge is modeled as a capacitor filled with plasma and has a dielectric constant determined by the nature of the generated plasma. Discharge current and voltage are always sinusoidal with typical 80^{o} phase between the voltage and current indicating the capacitive behavior of the test cell.

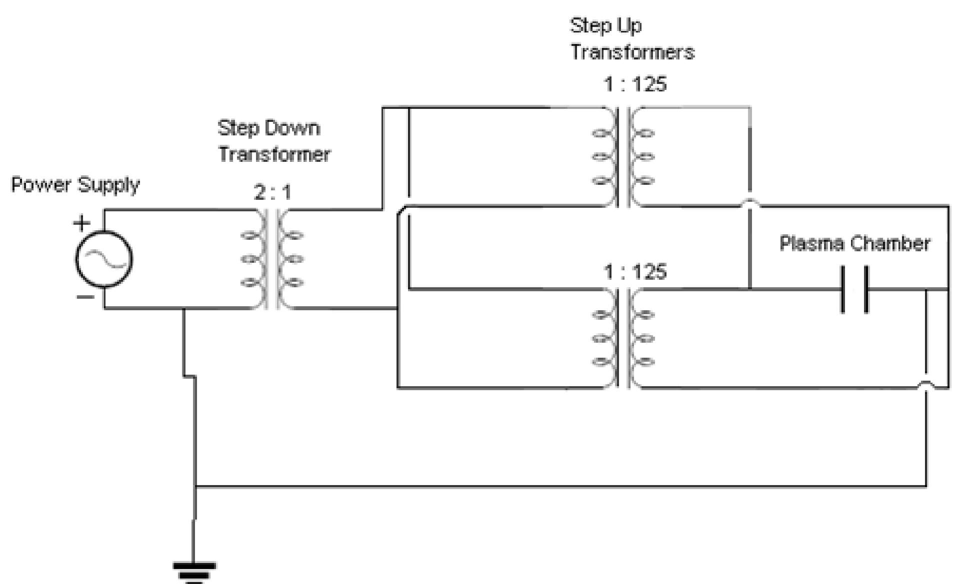

Figure 2.3; Electrical circuit of the system showing the power supply, step-down transformer, out-of-phase transformers and the plasma chamber modeled as a capacitor

Chapter 3: Plasma Parameters in the Hybrid System

3.1 Electrical Parameters

The current, voltage, and phase difference of the plasma discharge were all measured. The voltage was measured using a Tektronix P6015A compensated capacitively-coupled high voltage probe Model TDS 2024 ratio 1:1000, and the current was measured via a Pearson coil Model 2877 ratio 1V/1Amp. The waveforms were obtained by coupling the measuring sensors (voltage and current) to a Tektronix digital oscilloscope, which is connected to a computer running WaveStar® software and converting data into an Excel spreadsheet. As shown in Figure 3.1 for an experiment with pure helium, the voltage waveform is smoother than the current waveform due to the series of breakdowns that appear on the current more than that on the voltage.

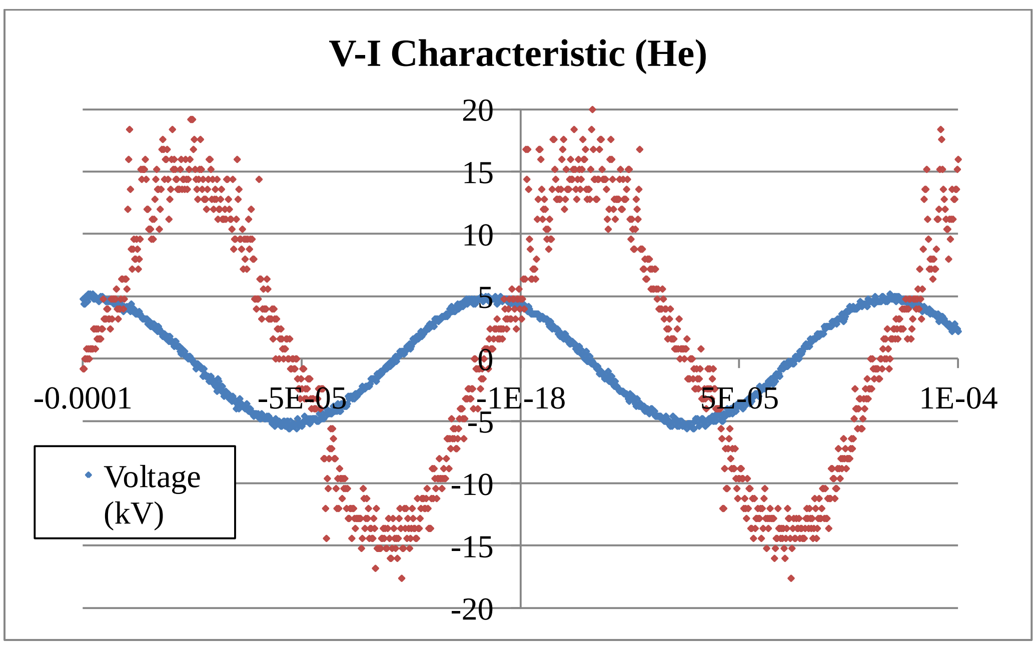

Figure 3.1; Voltage-Current characteristic for a pure helium discharge

The phase angle between the current and voltage is approximately 80^{o}, typical for this capacitively dominated discharge. Figure 3.2 shows the voltage and current of a He:O_2 discharge at a ratio of 99:1, where it is observed that the voltage is slightly higher as is expected for a discharge containing oxygen. The current is also slightly different and smoother at all positive half cycles, and its magnitude is slightly lower than that for the pure He discharge.

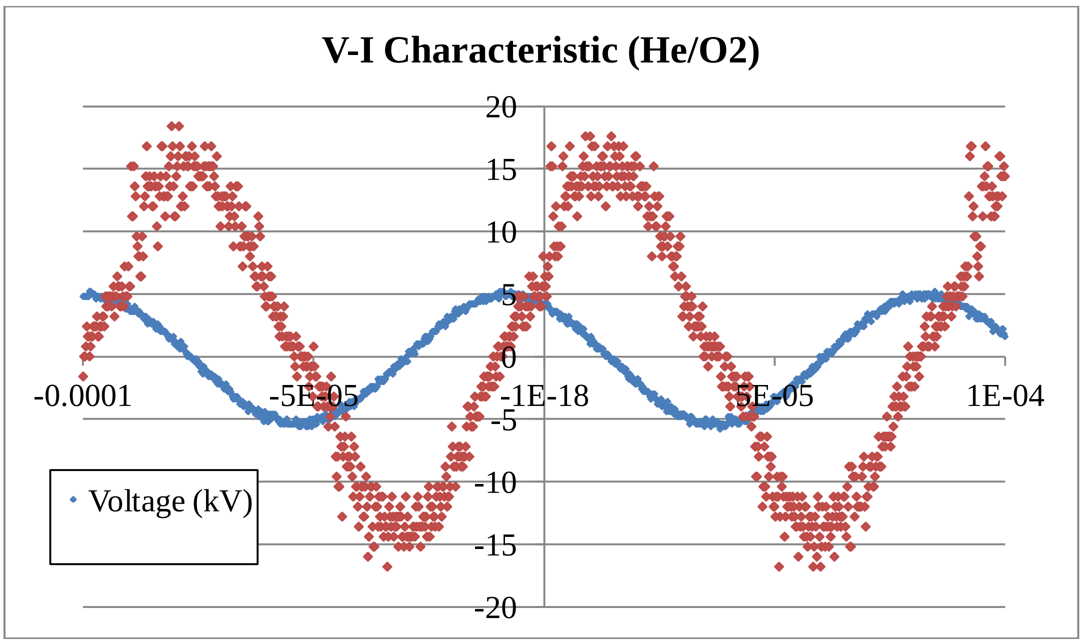

Figure 3.2; Voltage-Current characteristic for a He/O2 (99/1) discharge

A summary of the electrical parameters of pure helium and He/O_2 discharges is shown in Table 3.1. These electrical parameters are used as input parameters into the electrical model of the atmospheric plasma detailed in Section 4.1.

Table 3.1; Peak voltage and current along with calculated quantities, phase difference and impedance

	He	He/O_2
V (V)	5036.8	5096.7
I (A)	.0146	.0140
φ (rad)	1.41445	1.41371
Z	$344986\ e^{i1.41445}$	$364050\ e^{i1.41371}$

3.2 Thermal Properties

Bulk plasma temperature measurements were taken by an Omega perfluoroalkoxy (PFA) coated K-type thermocouple. The PFA electrically insulates the thermocouple to allow for direct gas temperature measurements in the plasma. The temperature was measured at the plasma outlet and at various locations in the electrospinning path. The temperature measurements indicate uniform plasma gas temperatures that all measured temperatures are within 2°C of the ambient temperature. This shows that this is, in fact, a non-thermal ‘cold’ plasma and will not thermally damage any materials being treated. This is an important aspect in the design of the hybrid atmospheric-electrospinning system ensuring no thermal effects on materials immersed in the plasma, which in turn ensures that any treatment results are solely due to plasma and not due to any thermal treatment.

3.3 Optical Emission Spectroscopy

3.3.1 Equipment

Optical emission spectroscopy has been used to obtain the spectra of the plasma at various locations inside the hybrid plasma source and specifically at the center of the discharge region. A 10 m long, 400 μm bifurcated fiber optic patch cord was used to transfer the light from the plasma source to two Ocean Optics HR2000 fixed grating spectrometers which were used to measure the spectra. Both spectrometers are fitted with a 600 line/mm grating, 25 μm slit and Ocean Optics L2 internal lens to focus the light onto the CCD. The grating of the UV-VIS spectrometer is blazed at 500 nm and views the wavelengths between 244 nm and 700 nm. The VIS-NIR spectrometer has a range of 593 nm to 1025 nm with the grating blazed at 750 nm. The spectrometers are power calibrated using an Ocean Optics LS-1-CAL lamp. Spectral data are transferred from the two spectrometers to a PC via IEEE interface card and an Ocean Optics software package.

3.3.2 Theory

Optical emission spectroscopy (OES) is a non-invasive diagnostic technique that can be used to identify plasma species and measure electron number density and temperature. The emission lines and bands present in the spectrum allow for the identification of the chemical species present in the plasma. These chemical species can be identified through the comparison of known atomic and molecular emission spectra and the emission lines and bands present in the plasmas emission spectrum. This information allow for the addition or omission of chemical species to or from the chemical kinetics code employed to determine the concentrations of the chemical species. The continuum of the plasma spectrum allows for the indirect measurement of the electron temperature and number density. The Bremsstrahlung radiation emitted by the free electrons decelerating due to collisions with neutral particles produces a continuum of radiation (neutral Bremsstrahlung). The produced neutral Bremsstrahlung continuum can be related to the electron temperature and the concentration of electrons in the plasma by the technique described by Park et al. if the plasma discharge is dominated by electron-neutral collisions [74], which is typical for most atmospheric pressure plasma discharges in which electron collisions are responsible for most reactions of the first and second order, and the momentum transport processes.

The first step in being able to match the measured continuum to a theoretical continuum is determining the theoretical continuum. The emission continuum is intensity per wavelength interval.

$$Q_{\lambda} = E_{rad} \nu_{\varepsilon\lambda} \qquad [3\text{-}1]$$

Where $E_{rad}=h\nu$ is the energy of the emitted photon and $\nu_{\varepsilon\lambda}$ is the emission frequency per unit volume in the wavelength interval dλ which is given by

$$\nu_{\varepsilon\lambda} = N_{gas} N_e \upsilon \frac{d\sigma_{NB,\lambda}(E)}{d\lambda} \qquad [3\text{-}2]$$

Where N_{gas} and N_e are the density of neutral atoms (or molecules) and electrons, respectively, υ is the initial velocity of the colliding electron, and $\frac{d\sigma_{NB,\lambda}(E)}{d\lambda}$ is the neutral bremsstrahlung emission cross section in a given wavelength interval $d\lambda$ as a function of electron energy. The energy of the emitted photon must be equal to or less than the initial energy of the colliding electron. Therefore, this term must be corrected by multiplying by the electron energy distribution function and integrating over all electron energies greater than the energy of the emitted photon yielding

$$Q_{\lambda} = N_{gas} N_e h\nu \int_{h\nu}^{\infty} \upsilon \frac{d\sigma_{NB,\lambda}(E)}{d\lambda} f(E) dE \qquad [3\text{-}3]$$

where $f(E)$ is the electron energy distribution function. However, the neutral Bremsstrahlung emission cross section is given by Dalgardo and Lane [75] per frequency interval.

$$\frac{d\sigma_{\nu}(E)}{d\nu} = \frac{8r_e}{3c}\frac{E}{h\nu}\left(1-\frac{h\nu}{E}\right)^{1/2}\left[q_0(E-h\nu)+\left(1-\frac{h\nu}{E}\right)q_0(E)\right] \qquad [3\text{-}4]$$

Where r_e is the classical electron radius, c is the speed of light, and q_0 is the electron momentum transfer cross section (the functional forms of the momentum transfer cross-section for He and O_2 and method for their determination are shown in Appendix A). This requires a change of variables yielding the final equation for the neutral Bremsstrahlung continuum intensity for a given wavelength interval.

$$Q_{\lambda} = N_{gas} N_e h\nu \int_{h\nu}^{\infty} \upsilon \frac{d\sigma_{\nu}(E)}{d\nu}\frac{d\nu}{d\lambda} f(E) dE \qquad \text{in } \frac{W}{cm^3 nm} \qquad [3\text{-}5]$$

This matches the equation given by Park et al. [74]. The electron momentum transfer cross sections for helium and oxygen were fitted from tabulated experimental data to allow for integration which leaves the electron energy distribution function (EEDF) as the last unaccounted term.

The most commonly used distribution for plasmas is a Maxwellian given by

$$f_{Max}(E) = \frac{2}{\sqrt{\pi}} \sqrt{E} (kT_e)^{-3/2} e^{\left(-\frac{E}{kT_e}\right)} \qquad [3\text{-}6]$$

Because the plasma is a non-equilibrium atmospheric pressure discharge, there are many inelastic processes which could cause the energy distribution to deviate from Maxwellian. The Druyvesteyn distribution was developed to account for these inelastic processes and is given by

$$f_{Dru}(E) = \frac{2}{\Gamma(0.75)} \left(\frac{\sqrt{0.548}}{< E >}\right)^{3/2} \sqrt{E} e^{\left(-0.548\left(\frac{E}{<E>}\right)^2\right)} \qquad [3\text{-}7]$$

Both the Maxwellian and Druyvesteyn distributions are examined and compared to determine which one better matches the experimental results. Samples of the calculated theoretical continua are shown in Figures 3.3 and 3.4.

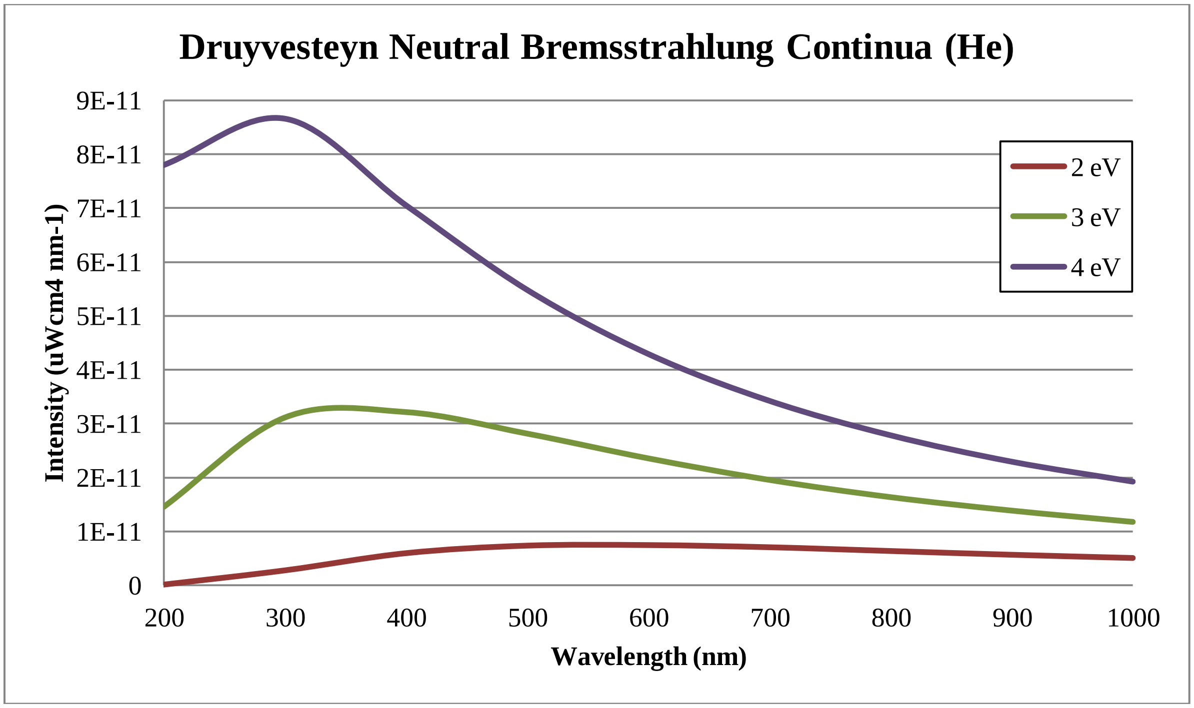

Figure 3.3; Theoretical Neutral Bremsstrahlung Continua calculated for a helium discharge using a Druyvesteyn EEDF

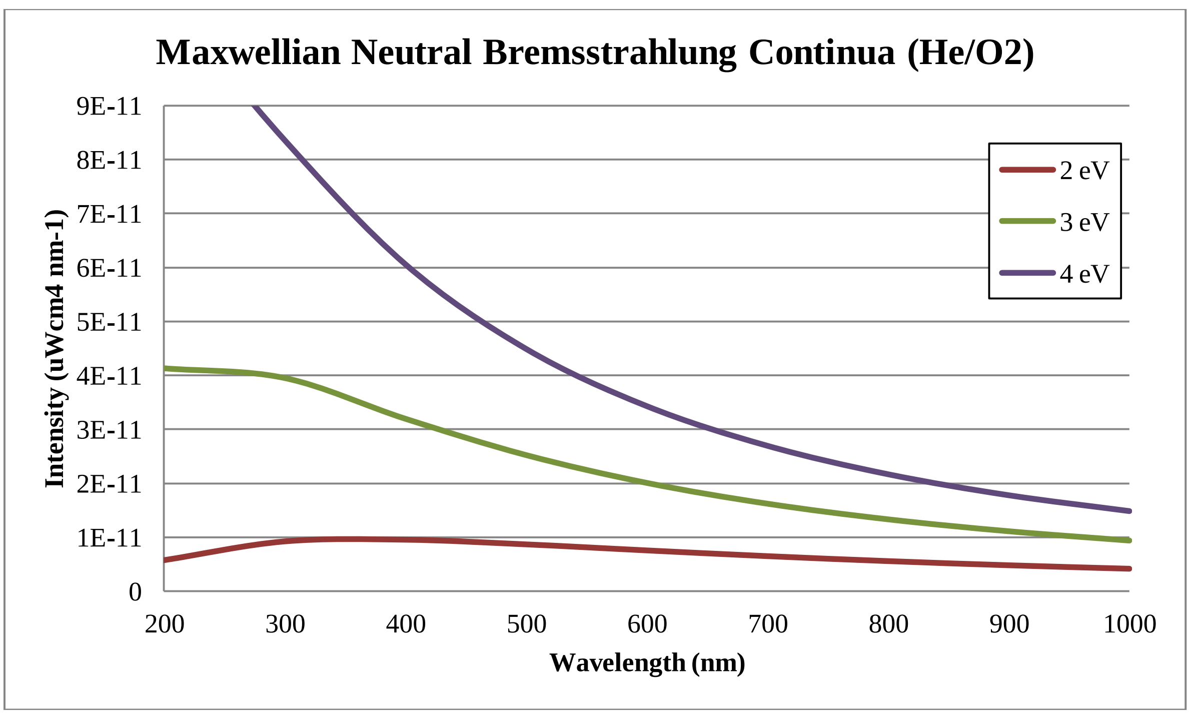

Figure 3.4; Theoretical Neutral Bremsstrahlung Continua calculated for a He/O2 discharge using a Maxwellian EEDF

Since the expression for the neutral Bremsstrahlung continuum intensity is a function of average electron energy and electron number density (Eqn 3-3), these parameters may be calculated through comparison with the experimentally measured continuum. First the continua will be normalized to allow for a comparison of continuum shape (related to electron temperature). Once normalized, the theoretical continua will be fit to the experimental continua to determine the electron temperature. After the temperature has been determined, the magnitude of the theoretical continuum will be compared to the absolutely calibrated experimental spectrum. This magnitude is a function of the electron number density, which is the final unknown in Eqn 3-3.

3.3.3 Spectral Measurements Results

3.3.3.1 Line Identification

The spectra for both plasma discharges (He and He/O_2) are very similar as the He/O_2 is only a 1% O_2, however, the pure helium discharge is not truly pure as there will always be a fraction of air in the discharge. The presence of oxygen lines in the helium discharge and the presence of N_2 lines in both spectra confirms the existence of a fraction of show air in the plasma cell, which is expected in an open air system with no vacuum equipment.

Figure 3.5 shows the atomic and molecular line identification of the helium discharge and the identified lines. Clearly helium lines are well identified. Several oxygen lines were also observed from the fractional air content in the plasma cell.

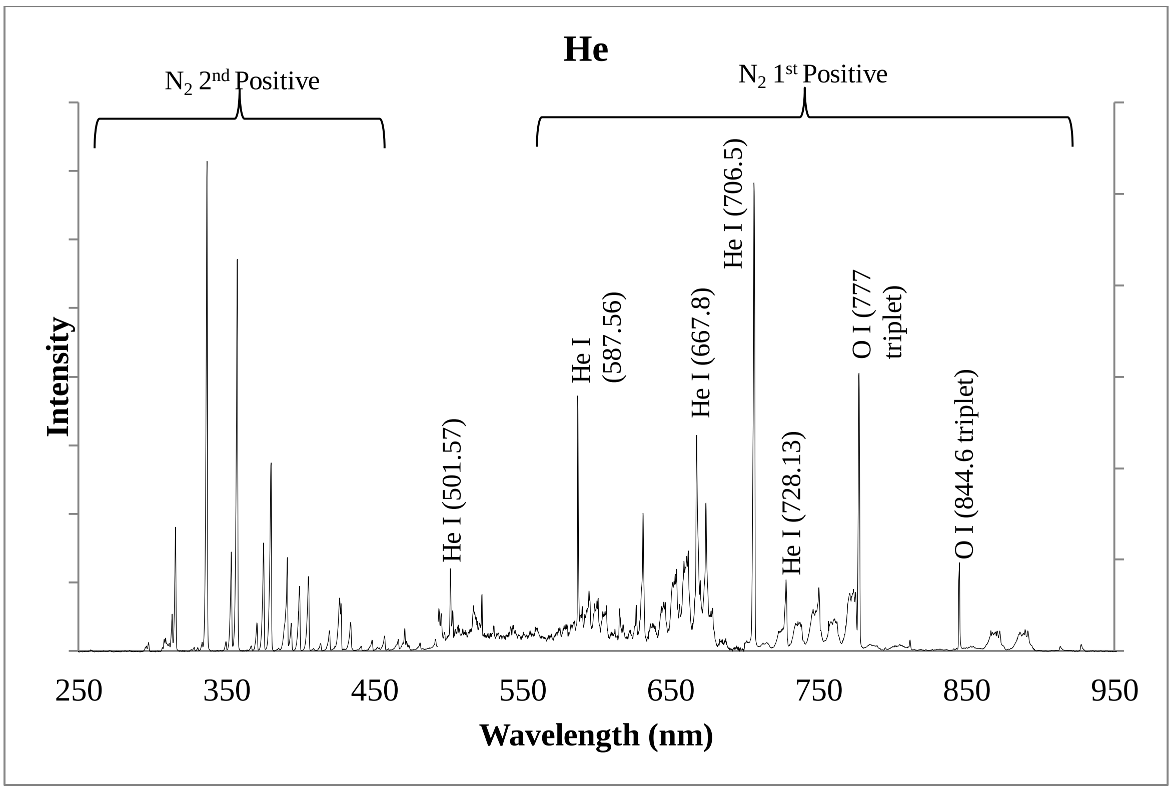

Figure 3.5; Atomic and Molecular Line Identification for He discharge

Figure 3.6 shows the atomic and molecular line identification of the helium/oxygen (He/O_2 ratio 99/1) discharge and the identified lines. Clearly it is very similar to the one obtained for pure helium discharge as can be seen from the identified lines. The only clear difference between the spectral lines is the increase in the relative intensity of the oxygen lines in the He/O_2 discharge, which is expected due to the increase in oxygen content flowing into the plasma cell.

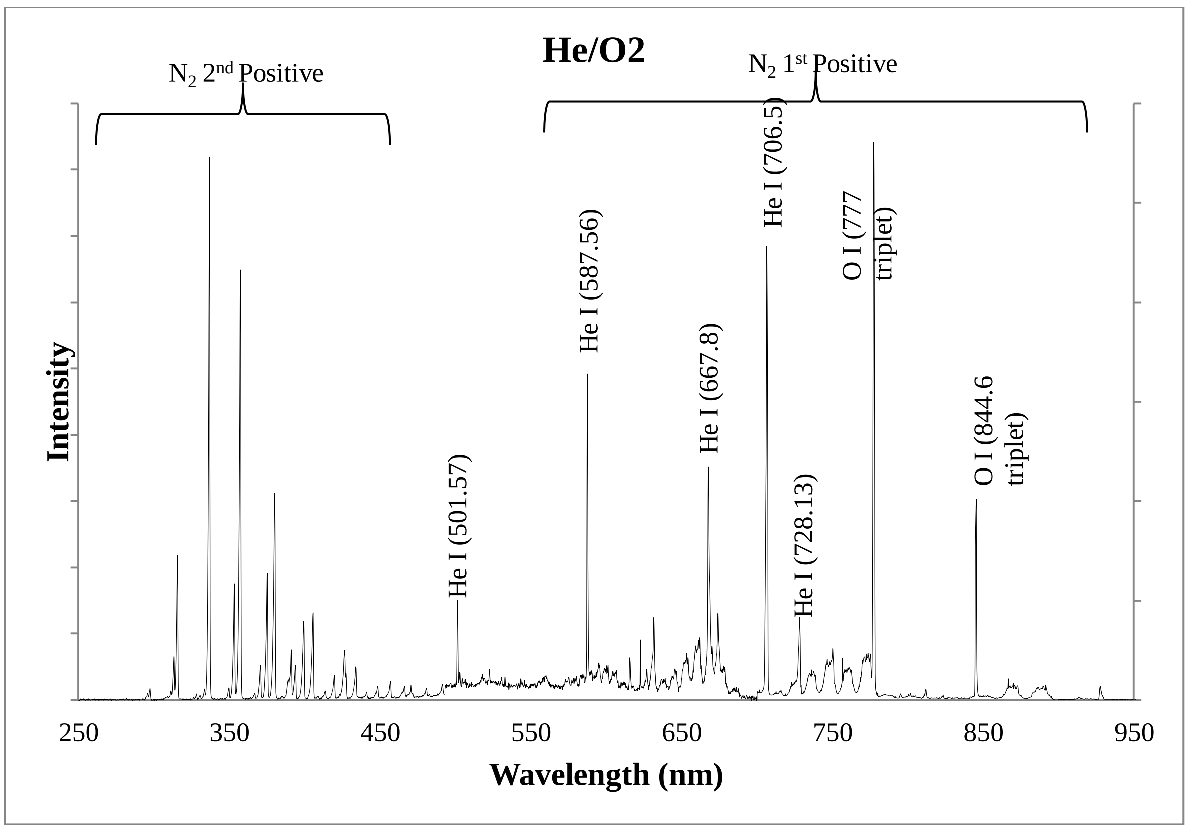

Figure 3.6; Atomic and Molecular Line Identification for He/O2 discharge

Atomic lines were identified using the NIST database [76] while molecular lines were identified using tables compiled by Pearse and Gaydon [77]. Table 3.2 shows the identified lines.

Table 3.2; Identified Atomic and Molecular Spectral Lines

Wavelength (nm)	Wavelength (nm)	Wavelength (nm)	Wavelength (nm)	Wavelength (nm)
He I	N_2 1st Positive	N_2 2st Positive	O I 777 triplet	O I 844.6 triplet
501.57	639.47	315.93	777.194	844.625
587.56	646.85	337.13	777.417	844.636
667.8	654.48	353.67	777.539	844.676
706.5	662.36	357.69		
728.13	738.66	375.54		
	750.39	380.49		
	762.62	399.84		
	775.32	405.94		
	872.23	426.97		
	891.16			

3.3.3.2 Neutral Bremsstrahlung

The theoretical neutral bremsstrahlung continua were generated using MathCad codes written for this purpose (reported listing is given in Appendix B). Both the theoretical continua and measured spectra were normalized to 700 nm in order to match the shape of the neutral bremsstrahlung continuum which gives an estimate of the average electron temperature because the theoretical continua are functions of energy. Upon determining the electron temperature, the electron number density can easily be calculated because it is the quotient of the measured continuum magnitude and the theoretical magnitude. Plots of He and He/O_2 continua using a Maxwellian EEDF are shown in Figures 3.7 and 3.8.

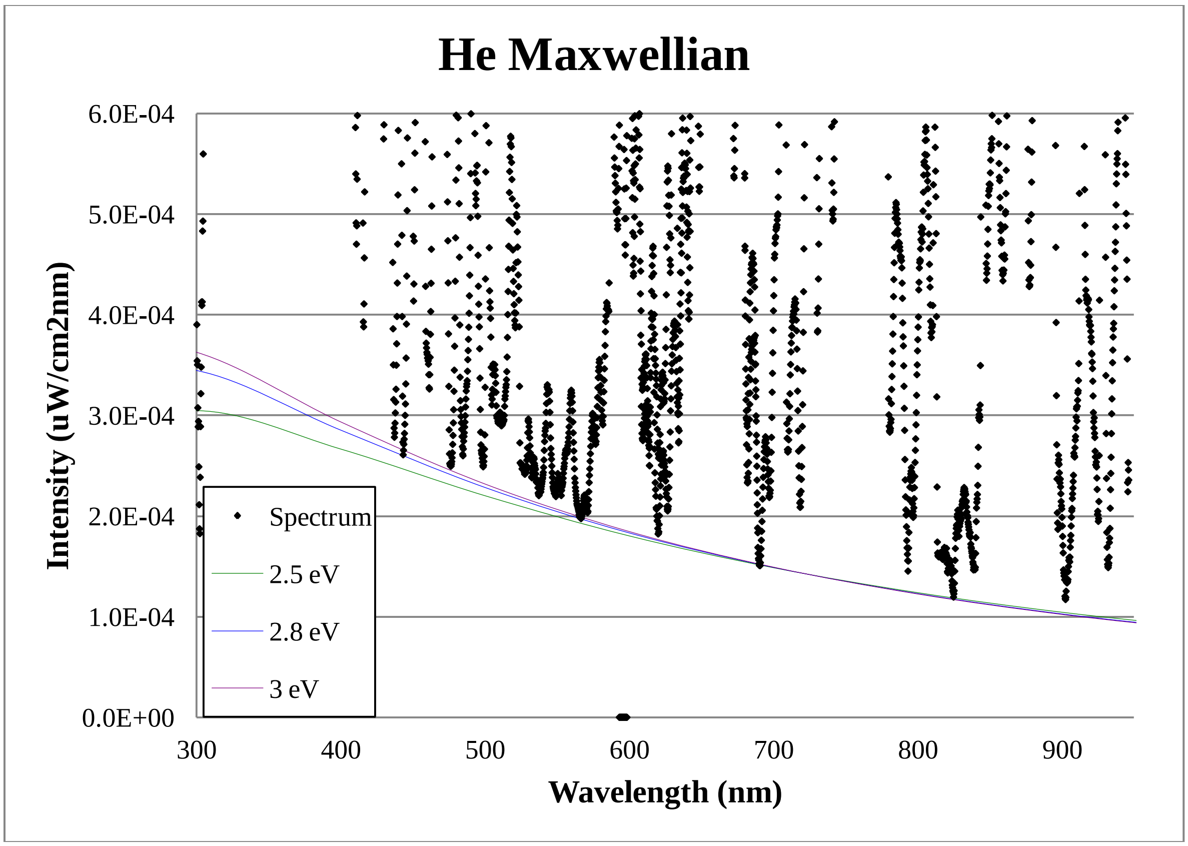

Figure 3.7; Neutral Bremsstrahlung Continuum matching for He discharge using a Maxwellian EEDF

The He discharge matches well to an average electron temperature of 2.8 eV for the Maxwellian EEDF, corresponding to 2.03×10^7 electrons/cm^3 while the He/O_2 discharge shows a lower electron temperature of 2.7 eV, corresponding to 1.16×10^7 electrons/cm^3.

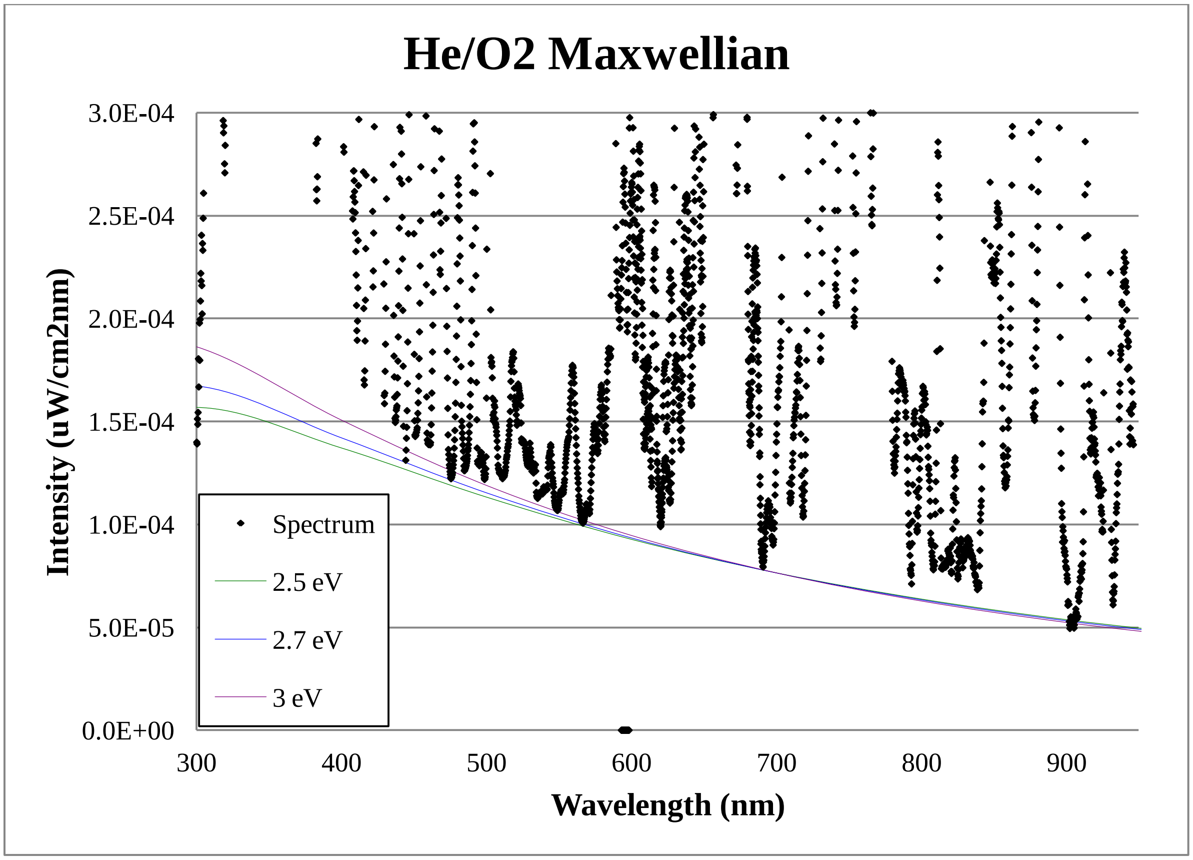

Figure 3.8; Neutral Bremsstrahlung Continuum matching for He/O_2 discharge using a Maxwellian EEDF

Using a Druyvesteyn EEDF (Figures 3.9 and 3.10), the electron temperatures were shown to be very similar for both the He and He/O_2 discharges (3.5 eV). The electron number densities, however, showed a difference of a factor of 2 between He and He/O_2 discharges, 1.1×10^7 and 5.6×10^6 electrons/cm^3, respectively.

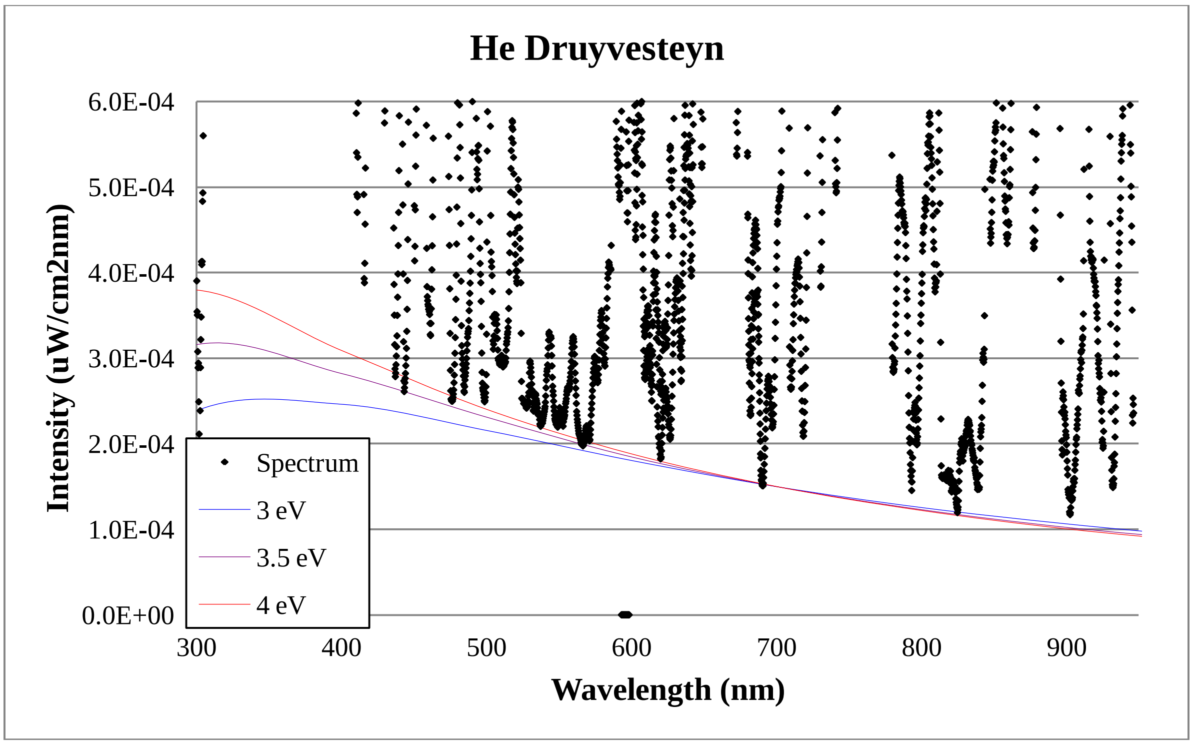

Figure 3.9; Neutral Bremsstrahlung Continuum matching for He discharge using a Druyvesteyn EEDF

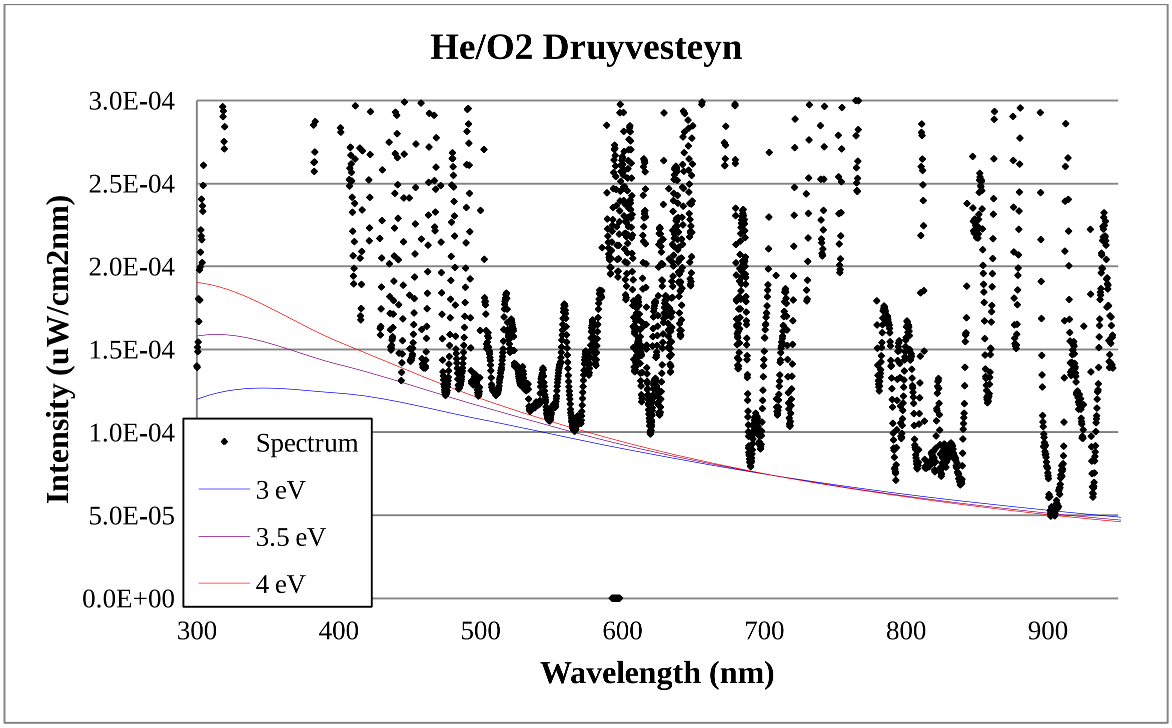

Figure 3.10; Neutral Bremsstrahlung Continuum matching for He/O_2 discharge using a Druyvesteyn EEDF

These numbers are well within the ranges for electron temperature and number density for atmospheric pressure plasma discharges. These results indicate a plasma temperature in the range of 2.5-3.5eV and an electron number density in the range $5.6x10^6$ to $2x10^7$ for such typical discharges. Also indicates that both methods are quite successful and adequate for determining the plasma discharge parameters.

Chapter 4: Atmospheric Plasma Modeling

4.1 Equivalent Circuit Model

A circuit model was developed based on modeling the plasma cell as an electrical circuit with equivalent circuit elements and impedances. To derive an equivalent circuit model, one can start from setting up the impedance equation for an oscillatory AC discharge as

$$Z = \frac{V_0}{I_0} e^{i\varphi} = \frac{V_0}{I_0} [\cos(\varphi) + i \sin(\varphi)] \qquad [4\text{-}1]$$

where Z is the complex impedance of the circuit, V_0 is the amplitude of the applied voltage, I_0 is the amplitude of the current, and φ is the phase angle between the current and voltage. It is reasonable to model the plasma as a series of complex impedances, and then the equivalent circuit impedance is given by

$$Z = Z_d + Z_{sheath} + Z_p \qquad [4\text{-}2]$$

where Z is the total equivalent impedance of the circuit [78-80]. This equivalent impedance is composed of three complex impedances, impedance of the dielectric barrier Z_d, which is composed of thin layers of garolite and polyethylene, the plasma sheath impedance Z_{sheath}, and the bulk plasma impedance Z_p. These three impedances will be considered separately.

4.1.1 Dielectric Barrier

The dielectric barrier is a simple series of two capacitors with the dielectric constants of the two materials. For the purposes of this model, the capacitances are considered a series of parallel plate capacitors whose capacitances are given by

$$C = \frac{k\varepsilon_0 A}{d} \qquad [4\text{-}3]$$

Where k is the relative permittivity (dielectric constant) of the material, ε_0 is the permittivity of free space, A is the area (equal for the two capacitors), and d is the thickness of each dielectric layer. The series combination of the two capacitors then yields the dielectric barrier impedance.

$$Z_d = \frac{-i}{\omega\varepsilon_0 A}\left(\frac{d_g}{k_g} + \frac{d_{pe}}{k_{pe}}\right) \qquad [4\text{-}4]$$

4.1.2 Sheath

The plasma sheath is approximated using the formulations developed by Oliver et al. [81] for a mobility limited ion sheath. They give the effective frequency dependent impedance as

$$Z_{sheath} = \frac{2s}{A\varepsilon_0\omega}\frac{\omega\tau - i\left[e^{-i\omega\tau} - 1\right] - i(\omega\tau)^2\left[\alpha + \frac{1}{2}\right]}{(\omega\tau)^2[1 + 2\alpha]} \qquad [4\text{-}5]$$

Where s is the sheath thickness, A is the area, ω is operating frequency, τ is the ion transit time across the sheath, and α is a parameter given by

$$\alpha = \frac{\varepsilon_0}{n_s e\mu\tau} \qquad [4\text{-}6]$$

Where n_s is the ion density at the sheath's edge and μ is the ion mobility obtained by

$$\mu = \frac{q}{m_i \nu_{in}} \qquad [4\text{-}7]$$

here m_i is the ion mass and ν_{in} is the ion-neutral collision frequency given by

$$\nu_{in} = \sigma n_n v_i \qquad [4\text{-}8]$$

and σ is the ion-neutral collision cross-section approximated by hard sphere collisions and v_i is the ion velocity.

The effective impedance may be simplified in the low frequency limit ($\omega\tau \ll 1$) to be

$$Z_{sheath} = \frac{i2s\alpha}{A\varepsilon_0\omega[1+2\alpha]} \qquad [4\text{-}9]$$

This shows that the impedance is given by an equivalent capacitance in the case of a high pressure (mobility limited), low frequency ($\omega\tau \ll 1$) plasma sheath.

4.1.3 Plasma

Assuming the plasma acts as a parallel plate capacitor with a complex frequency-dependent permittivity, its capacitance is given by

$$C_p = \frac{\tilde{\varepsilon}_p(\omega)A}{d_p} \qquad [4\text{-}10]$$

And the impedance is then given by

$$Z_p = \frac{1}{i\omega C_p} \qquad [4\text{-}11]$$

Combining the equations

$$Z_p = \frac{d_p}{i\omega\tilde{\varepsilon}_p(\omega)A} \qquad [4\text{-}12]$$

The frequency, thickness, and area are all known quantities, leaving only the permittivity as the remaining unknown.

The Drude Model was used to determine the permittivity of the plasma. This model takes into account the frequency of the applied voltage, the restoring force of a resonant (natural) frequency for the electrons, and the drag created by collisions in the plasma [78]. Because this is weakly ionized plasma, the collision frequency can be approximated as the electron-neutral collision frequency, thus neglecting the electron-ion collision frequency, and the equation for this model becomes,

$$\tilde{\varepsilon}_p(\omega) = \varepsilon_0 \left[1 + \frac{\omega_p^2}{(\omega_0^2 - \omega^2 - i\omega\nu_{en})} \right] \qquad [4\text{-}13]$$

Where ε_o is the permittivity of free space, ω_o is the resonant frequency, ω is the frequency of the applied field, and ω_p is the electron plasma frequency given by,

$$\omega_p^2 = \frac{ne^2}{m_e\varepsilon_0} \qquad [4\text{-}14]$$

This resonant frequency is caused by the binding energy that the atom exerts on the electron. Since the current is carried by the free electrons in the plasma, there is no resonant frequency, and hence $\omega_o = 0$. This simplifies the equation slightly; however there is a great deal of algebra to obtain a useful form of the impedance.

Eliminating the resonant frequency the Drude model becomes

$$\tilde{\varepsilon}_p(\omega) = \varepsilon_0 \left[\frac{(-\omega^2 - i\omega\nu_{en}) + \omega_p^2}{(-\omega^2 - i\omega\nu_{en})} \right] \qquad [4\text{-}15]$$

Inversing Eqn 4-15 one gets $\frac{\varepsilon_0}{\tilde{\varepsilon}_p(\omega)} = \left[\frac{-\omega^2 - i\omega\nu_{en}}{\omega_p^2 - \omega^2 - i\omega\nu_{en}} \right]$ which yields

$$\frac{\varepsilon_0}{\tilde{\varepsilon}_p(\omega)} = \frac{\left(\omega^4 - \omega^2\omega_p^2 + \omega^2\nu_{en}^2\right) - i\omega\omega_p^2\nu_{en}}{\left(\omega_p^2 - \omega^2\right)^2 + \omega^2\nu_{en}^2} \qquad [4\text{-}16]$$

The above equation can be separated into the real and imaginary parts. Substituting the result from Eqn 4-16 into the plasma impedance gives

$$Z_p = \frac{d_p}{i\omega\varepsilon_0 A}\frac{\left(\omega^4 - \omega^2\omega_p^2 + \omega^2\nu_{en}^2\right) - i\omega\omega_p^2\nu_{en}}{\left(\omega_p^2 - \omega^2\right)^2 + \omega^2\nu_{en}^2} \qquad [4\text{-}17]$$

And distributing the i terms one obtains

$$Z_p = \frac{d_p}{\omega\varepsilon_0 A}\frac{-\omega\omega_p^2\nu_{en} - i\left(\omega^4 - \omega^2\omega_p^2 + \omega^2\nu_{en}^2\right)}{\left(\omega_p^2 - \omega^2\right)^2 + \omega^2\nu_{en}^2} \qquad [4\text{-}18]$$

4.1.4 Total Impedance

Combining these three impedances as per Eqn 4-2 yields the following.

$$\begin{aligned} Z = \frac{-i}{\omega\varepsilon_0 A}\left(\frac{d_g}{k_g} + \frac{d_{pe}}{k_{pe}}\right) + \frac{i2s\alpha}{A\varepsilon_0\omega[1 + 2\alpha]} \\ + \frac{d_p}{\omega\varepsilon_0 A}\frac{-\omega\omega_p^2\nu_{en} - i\left(\omega^4 - \omega^2\omega_p^2 + \omega^2\nu_{en}^2\right)}{\left(\omega_p^2 - \omega^2\right)^2 + \omega^2\nu_{en}^2} \end{aligned} \qquad [4\text{-}19]$$

The complex impedance can be broken into the real and imaginary parts as follow:

$$Re(Z) = \frac{d_p}{\omega\varepsilon_0 A}\frac{-\omega\omega_p^2\nu_{en}}{\left(\omega_p^2 - \omega^2\right)^2 + \omega^2\nu_{en}^2} \qquad [4\text{-}20a]$$

$$Im(Z) = \frac{-1}{\omega\varepsilon_0 A}\left(\frac{d_g}{k_g} + \frac{d_{pe}}{k_{pe}}\right) + \frac{2s\alpha}{A\varepsilon_0\omega[1 + 2\alpha]} - \frac{d_p}{\omega\varepsilon_0 A}\frac{\left(\omega^4 - \omega^2\omega_p^2 + \omega^2\nu_{en}^2\right)}{\left(\omega_p^2 - \omega^2\right)^2 + \omega^2\nu_{en}^2} \qquad [4\text{-}20b]$$

These can then be equated to Eqn 4-1 as follows

$$\frac{V_0}{I_0}\cos(\varphi) = \frac{d_p}{\omega\varepsilon_0 A}\frac{-\omega\omega_p^2\nu_{en}}{\left(\omega_p^2 - \omega^2\right)^2 + \omega^2\nu_{en}^2} \qquad [4\text{-}21a]$$

$$\frac{V_0}{I_0}\sin(\varphi) = \frac{-1}{\omega\varepsilon_0 A}\left(\frac{d_g}{k_g} + \frac{d_{pe}}{k_{pe}}\right) + \frac{2s\alpha}{A\varepsilon_0\omega[1 + 2\alpha]} - \frac{d_p}{\omega\varepsilon_0 A}\frac{\left(\omega^4 - \omega^2\omega_p^2 + \omega^2\nu_{en}^2\right)}{\left(\omega_p^2 - \omega^2\right)^2 + \omega^2\nu_{en}^2} \qquad [4\text{-}21b]$$

4.1.5 Circuit Model Results

The solutions for the electron number density n_e and the plasma temperature T_e are determined graphically (the MathCad codes used to determine these graphs are included in Appendix C). The resistance and reactance are plotted as functions of both n_e and T_e. There are multiple solutions which satisfy either $R=Re(Z)$ or $X=Im(Z)$, but only one set of n_e and T_e that satisfies both. As seen in Figure 4.1 the He solution corresponds to a plasma temperature of 2.66 eV and an electron density of $6.45\text{x}10^{8}$ cm^{-3}.

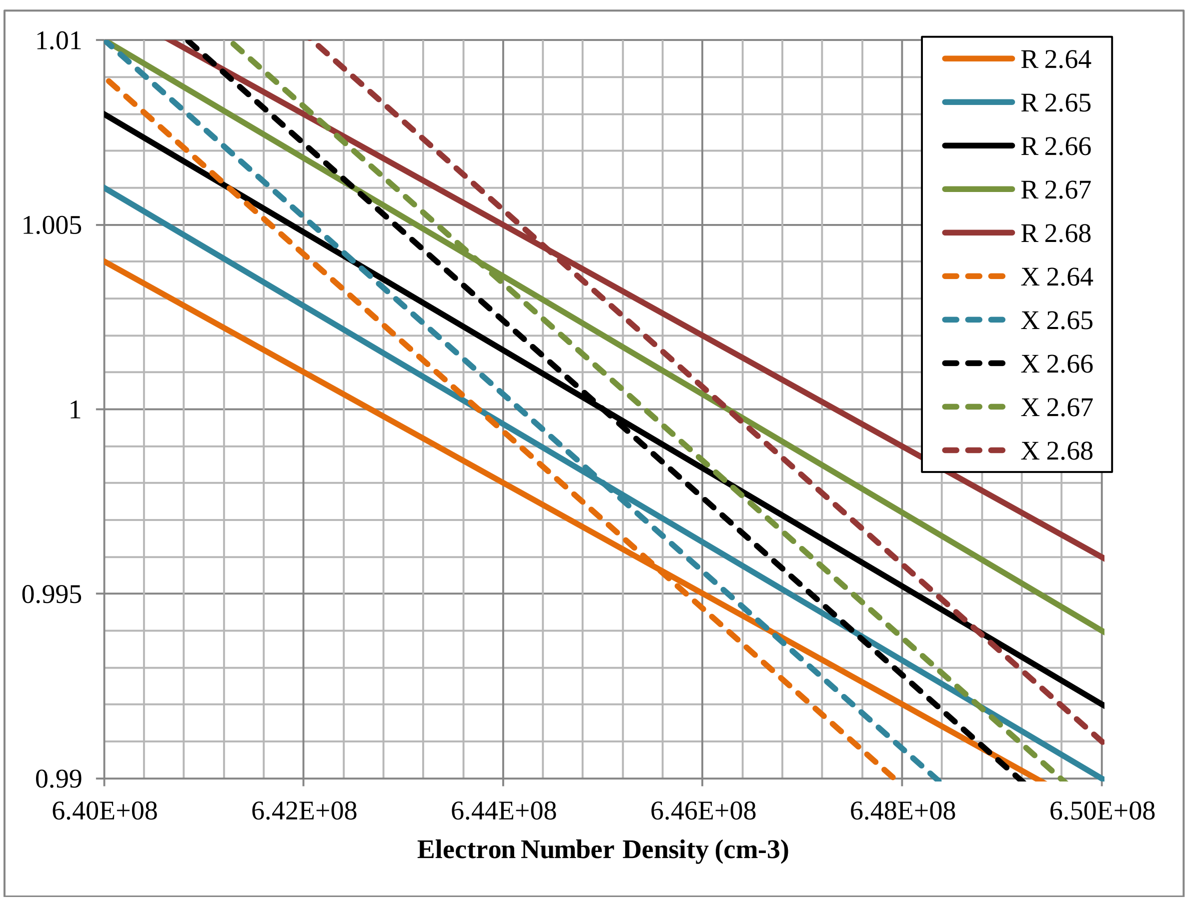

Figure 4.1; Graphical Solution of Circuit Model for He discharge

Figure 4.2 shows the He/O_2 solution corresponding to 2.845 eV and 6.318×10^{8} cm^{-3}.

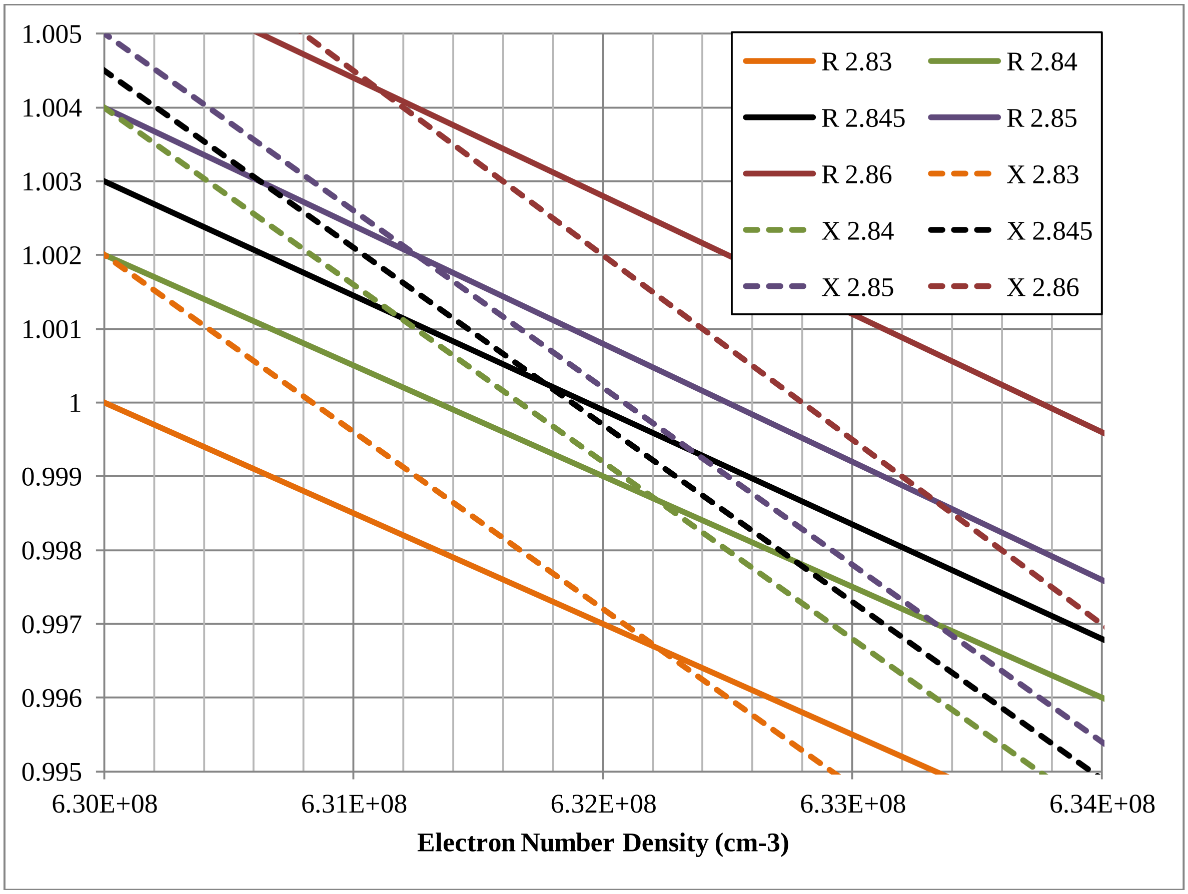

Figure 4.2; Graphical Solution of Circuit Model for He/O_2 discharge

The results are shown in Figure 4.3 along with the results calculated from the neutral bremsstrahlung technique using both Maxwellian (Max) and Druyvesteyn (Dru) electron energy distributions (EED).

The error associated with the temperatures calculated using the neutral bremsstrahlung technique is ~20%. This shows that the temperatures calculated for the circuit model and the neutral bremsstrahlung technique with a Maxwellian EEDF are well within the margin of error of each other. Electron temperatures in this range will be used in the chemical kinetics model.

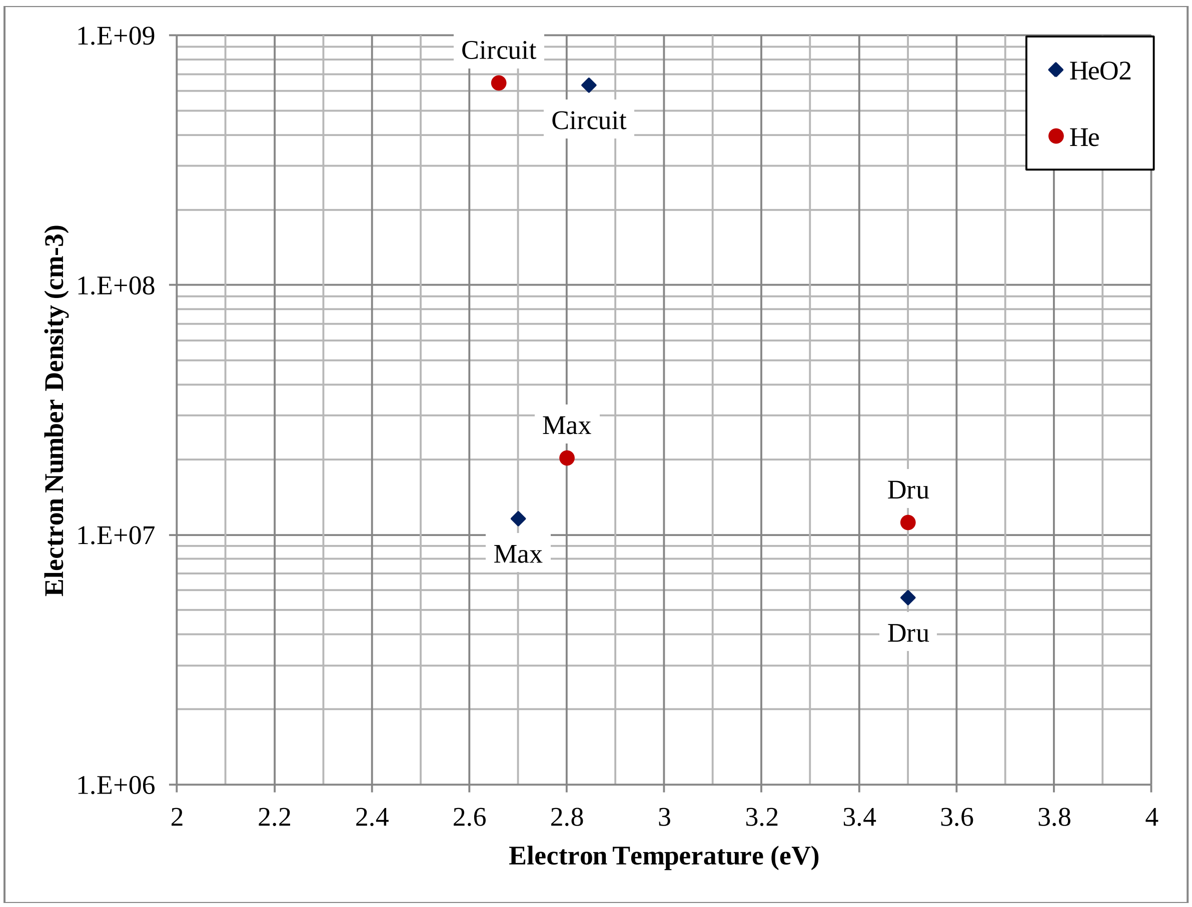

Figure 4.3; Electron temperature and number density calculated using the circuit model (Circuit) and neutral bremsstrahlung technique with Maxwellian (Max) and Druyvesteyn (Dru) EED

4.2 Chemical Kinetics Model

As indicated in the literature review in Section 1.3, atmospheric plasmas used for surface modifications are not typically characterized by traditional plasma parameters. Authors give the working gas, the chamber pressure, the chamber geometry, electrical schematic, and details of the power supply used as the main parameters in atmospheric plasma surface modification systems. This information is, at best, enough to recreate the exact conditions of the experiment. It does not tell other experimenters whether or not their plasma device could reproduce the experiment. It would be better if the plasmas were characterized by their electron number densities, electron temperatures, mean free paths, chemical species present in the plasma, ion and radical concentrations, and chemical reaction rates. In the previous chapters, the electron number density, and temperatures have been characterized through OES and circuit modeling with good correlation between the results from various techniques and have shown consistency and adequate results as compared to results from the developed models. These values are now used as inputs into a chemical kinetics model in order to determine the concentrations of chemical species present in the plasma.

4.2.1 Global Chemical Kinetics Model

This model assumes a time and space average within the plasma cell. A steady flow of working gas (He and O_2) is introduced at the inlet. Because the cell pressure is steady, the flow at the exit must be equal to the inlet flow. This out flow is a loss for all species and is directly proportional to the concentration of each species individually. The formulations presented are based on Kuo [82].

Given the general set of chemical equations:

$$\sum_{k=1}^{K} \nu'_{\mathrm{ki}} \mathrm{C_k} \rightarrow \sum_{k=1}^{K} \nu''_{\mathrm{ki}} \mathrm{C_k} \qquad [4\text{-}22]$$

The rates of creation ($\dot{\mathrm{C}}_\mathrm{k}$) and destruction ($\dot{\mathrm{D}}_\mathrm{k}$) of species *k* may be written as (including flow-in (FI) and flow-out (FO))

$$\dot{\mathrm{C}}_\mathrm{k} = \sum_{i=1}^{I} \nu''_{\mathrm{ki}} \mathrm{k_i} \prod_{\mathrm{j=1}}^{\mathrm{K}} \mathrm{C_{M,j}}^{\nu'_{\mathrm{ji}}} + \mathrm{FI_k} \qquad [4\text{-}23a]$$

$$\dot{\mathrm{D}}_\mathrm{k} = \sum_{i=1}^{I} \nu'_{\mathrm{ki}} \mathrm{k_i} \prod_{\mathrm{j=1}}^{\mathrm{K}} \mathrm{C_{M,j}}^{\nu'_{\mathrm{ji}}} + \mathrm{FO_k} \qquad [4\text{-}23b]$$

Once steady state is reached $\dot{\mathrm{C}}_\mathrm{k} = \dot{\mathrm{D}}_\mathrm{k}$, an iterative scheme can be used to solve for the concentrations of all the species. Starting with an initial value, and building upon each iteration, we can write

$$\mathrm{C_{k,x+1}} = \frac{\sum_{i=1}^{I} \nu''_{\mathrm{ki}} \mathrm{k_i} \prod_{\mathrm{j=1}}^{\mathrm{K}} \mathrm{C_{M,j,x}}^{\nu'_{\mathrm{ji}}} + \mathrm{FI_k}}{\sum_{i=1}^{I} \nu'_{\mathrm{ki}} \mathrm{k_i} \prod_{\mathrm{j=1}}^{\mathrm{K}} \mathrm{C_{M,j,x}}^{\nu'_{\mathrm{ji}}} + \mathrm{FO_{k,x}}} \mathrm{C_{k,x}} \qquad [4\text{-}24]$$

This model iterates until $\sum_{k=1}^{K} \left|\mathrm{C_{k,x+1}} - \mathrm{C_{k,x}}\right| < .001$ (the code can be found in Appendix D)

The model includes 14 species of helium and oxygen (He, He*, He^+, He_2*, $He2^+$, O_2, O_2*, O_2^+, O_2^-, O, O*, O^+, O^-, and O_3). The metastable species refer to He(^{2}S), O_2($^1\Delta$), and O(^{1}D). He_2* is the "ground" state of He_2 because a stable version does not exist. There are 123 reaction mechanisms considered for these species plus electrons as well as 10 wall reactions. The reactions for a pure helium discharge are shown in Table 4.1. The full set of reactions used can be found in Appendix E. Table 4.2 shows the wall reactions and their probabilities. The rate constants shown are in cm^3s^{-1} for two body reactions, cm^6s^{-1} for three body reactions and s^{-1} for the radiative de-excitation of O_2*. T_e is in eV, T is in K, and T_o = T/300.

Table 4.1; Reactions & Rate Constants for pure He

No.	Reaction	Rate Constant, k (cm, molecules, s)	Ref.
1	$e + He \rightarrow He^* + e$	$4.2E-9\ T_e^{0.31}\exp(-19.8/T_e)$	83
2	$e + He \rightarrow He^+ + e + e$	$1.5E-9\ T_e^{0.68}\exp(-24.6/T_e)$	83
3	$He^* + He \rightarrow He + He + hv$	$3.06E-15$	84
4	$e + He^* \rightarrow He + e$	$2.00E-10\ T_e^{0.31}$	85
5	$He^* + He^* \rightarrow He^+ + He + e$	$1.5E-9\ T_o^{0.5}$	86
6	$e + He^+ \rightarrow He^*$	$6.76E-13\ T_e^{-0.5}$	86
7	$e + e + He^+ \rightarrow He^* + e$	$5.12E-27\ T_e^{-4.5}$	86
8	$e + He^* \rightarrow He^+ + e + e$	$1.28E-7\ T_e^{0.6}\exp(-4.78/T_e)$	86
9	$e + He_2^+ \rightarrow He^* + He$	$5.0E-9\ T_e^{-0.5}$	83
10	$He^+ + He + He \rightarrow He_2^+ + He$	$2.0E-31$	83
11	$e + He_2^* \rightarrow He_2^+ + e + e$	$9.75E-10\ T_e^{0.71}\exp(-3.4/T_e)$	85
12	$He^* + He + He \rightarrow He_2^* + He$	$1.3E-33$	85
13	$He^* + He^* \rightarrow He_2^+ + e$	$2.0E-9$	87
14	$e + e + He_2^+ \rightarrow He + He + e$	$5.036E-27\ T_e^{-4.5}$	87
15	$e + He_2^+ \rightarrow He + He$	$1.0E-8$	87
16	$e + He + He_2^+ \rightarrow He + He + He$	$2.0E-27$	87
17	$He_2^* + He_2^* \rightarrow He_2^+ + He + He + e$	$1.5E-9$	88

Table 4.2; Wall Reactions [86]

No.	Wall Reaction	Probability
W1	$He^{*} + wall \rightarrow He$	1.0
W2	$He^{+} + wall \rightarrow He$	1.0
W3	$He_2^{+} + wall \rightarrow He_2^{*}$	1.0
W4	$O_2^{*} + wall \rightarrow O_2$	1E-5
W5	$O + wall \rightarrow 1/2\ O_2$	0.02
W6	$O_2^{+} + wall \rightarrow O_2$	1.0
W7	$O_2^{-} + wall \rightarrow O_2$	1.0
W8	$O^{*} + wall \rightarrow O$	1.0
W9	$O^{+} + wall \rightarrow O$	1.0
W10	$O^{-} + wall \rightarrow O$	1.0

4.2.2 Chemical Kinetics Results

As was discussed in Section 4.1.5, the electron temperatures calculated using the neutral bremsstrahlung technique with a Maxwellian EEDF and the circuit model are within the margin of error of each other. The electron number densities, while within the range expected for atmospheric pressure plasmas, are significantly different. The results of the chemical kinetics model show that the logarithmic ratios of species concentrations are relatively independent of electron number density and depend almost exclusively on the electron temperature input. This is apparent in Figure 4.4 showing concentration vs. electron number density at 3 eV.

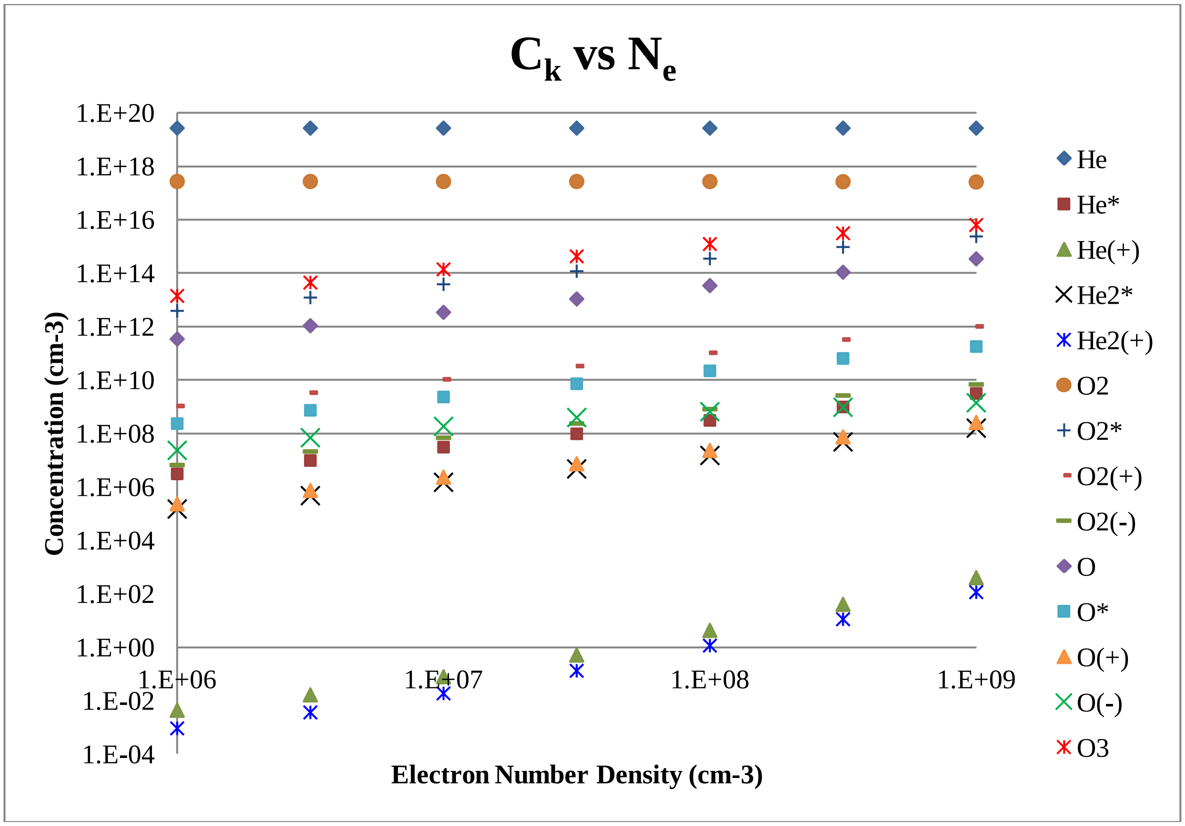

Figure 4.4; Species concentration vs. electron number density at 3 eV

All species are following very similar slopes except for O^- which follows a slightly shallower slope. This is in stark contrast to the data shown in Figures 4.5 and 4.6 which show large changes in concentration ratios with changes in electron temperature.

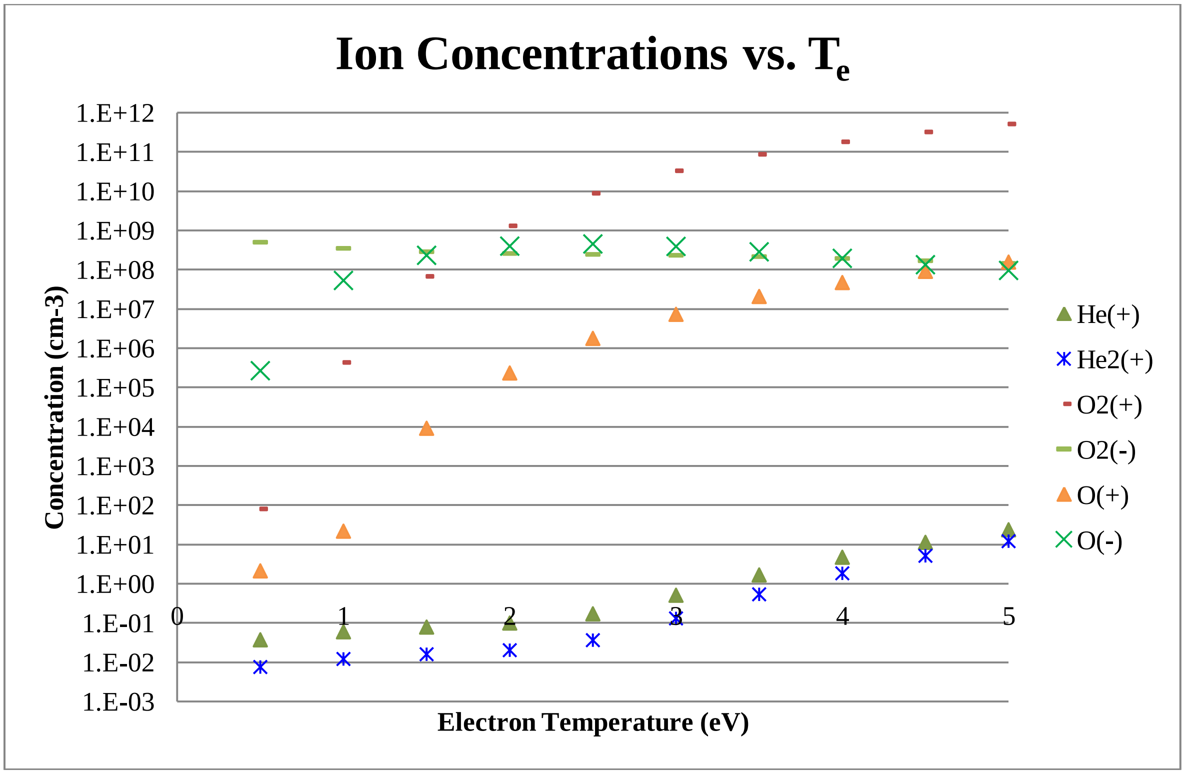

Figure 4.5; Ion concentration vs. electron temperature at an electron number density of 5E7 cm-3

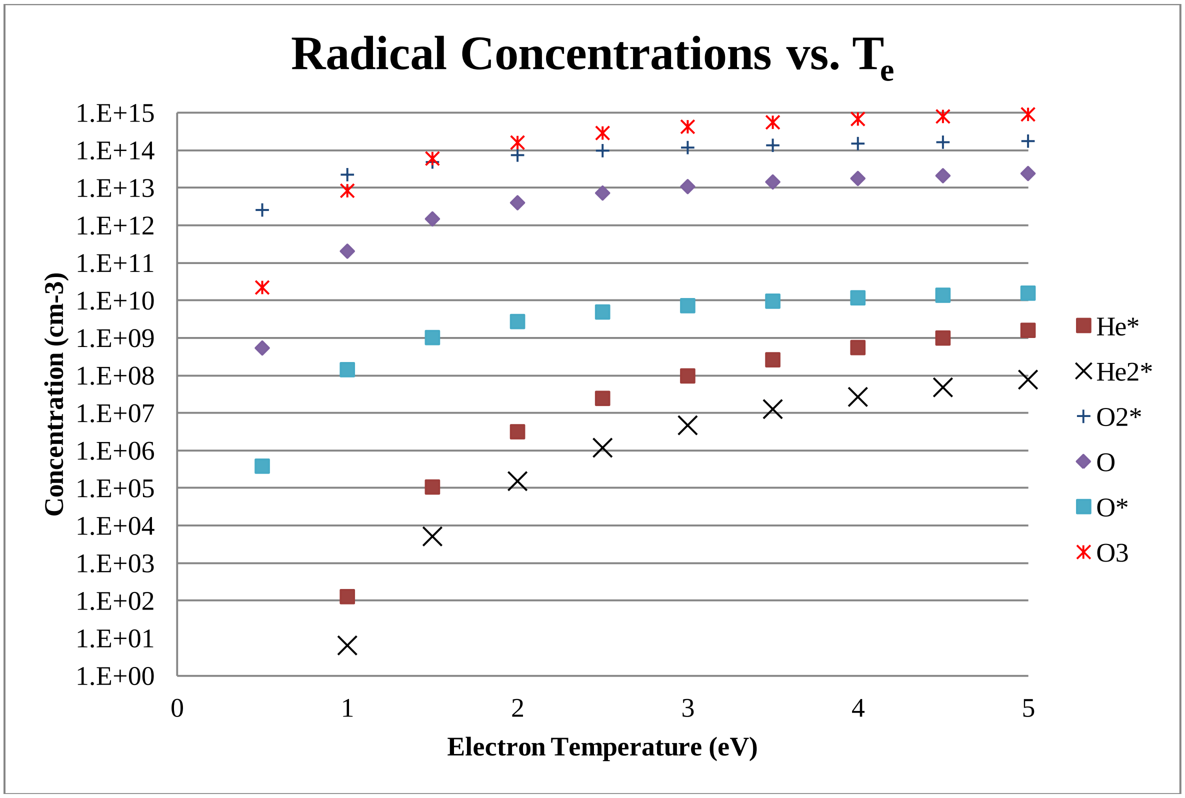

Figure 4.6; Radical concentration vs. electron temperature at an electron number density of 3E7 cm-3

It is clear that the He/O_2 plasma is dominated by both oxygen ions and radicals and that in this case, the helium plays a lesser role. Without accurate electron number densities, it is impossible to determine the exact concentrations of the plasma species. It is, however, possible to determine the relative concentrations of species with reasonably accurate electron temperature data. This allows for a determination of which species dominate the plasma, which in turn allows for a more complete understanding of the surface modification mechanisms involved in the enhanced adhesion of nanofibers to the fabric substrate.

Chapter 5: Experiments on Nanofiber Production Using the Hybrid System

5.1 Nanofiber Production

Nylon 6 nanofibers were electrospun in the hybrid system. The electrospinning syringe was filled with Nylon 6 (12 wt%) solution in tetrafluoroethylene (TFE). The feed rate was maintained at 1 ml/hr. The needle tip was placed 15 cm from the rotating collector and the electrospinning voltage was set at 15 kV. The substrate was a Nylon 6,6 / cotton (50/50) woven fabric (240 g/m2). The fabric was placed on aluminum foil and fastened to the rotating collector. The rotational speed was steady at 20 rpm. The experimental set-up is shown in the Figure 5.1.

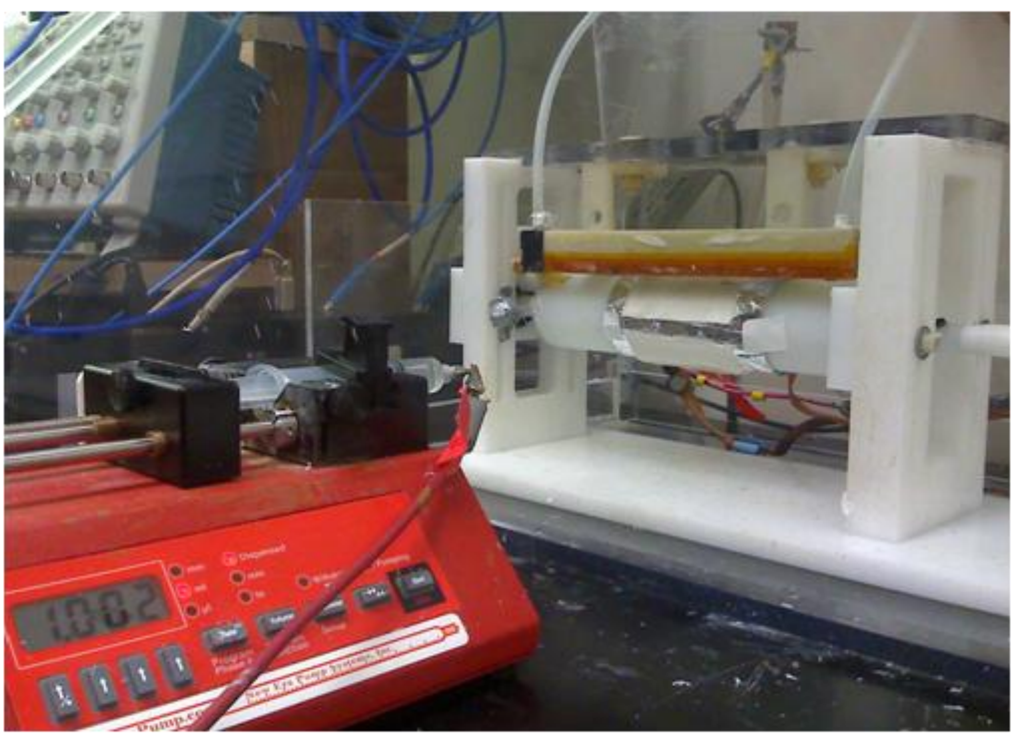

Figure 5.1; Set-up for hybrid atmospheric plasma treatment while electrospinning

The plasma gas was either 100% He or He:O_2 (99:1) with a total gas flow rate of 20 L/min.

The plasma was blown down in front of the rotating collector as shown in Figure 5.2. The deposition time for each nanofiber mat was held constant at 10 min.

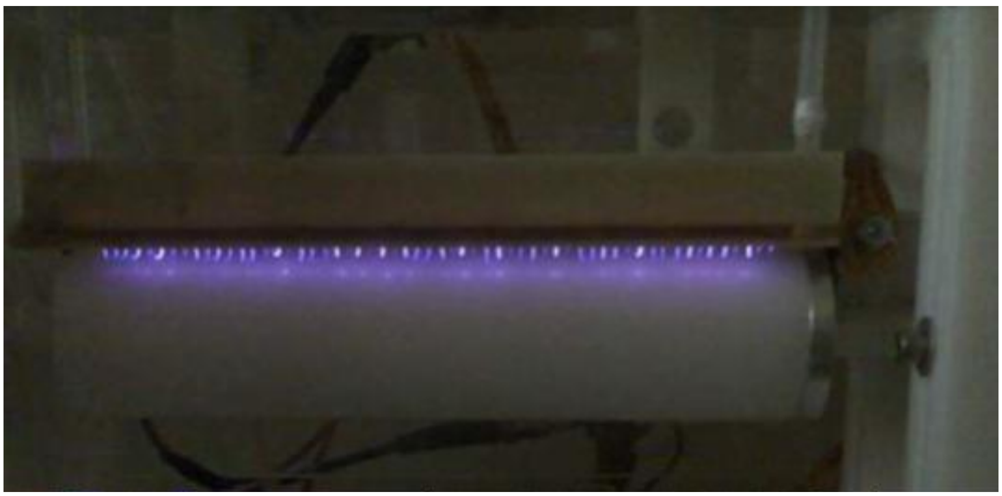

Figure 5.2; He plasma being blown in front of the electrospinning collector

5.2 Nanofiber Characterization

The nylon nanofibers were characterized in two ways, elemental composition and adhesion to the substrate. The elemental composition analysis was performed through X-Ray Photoelectron Spectroscopy (XPS). The adhesive strength was both quantified by a peel test and qualitatively analyzed through flex testing.

5.2.1 XPS Analysis

The XPS analysis was carried out using Axis Ultra (Kratos Analytical Ltd, UK) with MgKα excitation (1254 eV). The energy was calibrated using the adventitious carbon line

(C1s at 284.5 eV binding energy) as a reference. The base pressure of the analysis chamber was ~10^{-10} Torr. CASA XPS software was used to analyze the data. The elemental surface compositions of the nylon nanofibers are shown below along with the relative surface chemical bonds (in %).

Table 5.1; Elemental surface composition and relative surface bonds of the control and hybrid electrospun nanofibers

	Composition (%)			Relative Surface Chemical Bonds (%)				
	C	O	N	C-C	C-N	C-O	CONH	O-C=O
Control	78.1	11.1	10.8	39.3	33.2	-	27.5	-
He plasma	77.2	10.8	12	44.8	26.3	17.4	11.4	-
He/O2 plasma	72.5	16.6	10.9	23.8	5.5	45.4	5.7	19.6

Nanofibers hybrid electrospun with pure helium plasma did not show a significant change in elemental surface composition when compared to the control samples. Mainly there was a slight increase in nitrogen content accompanied by a slight decrease in carbon content. There was, however, a significant change in relative surface chemical bonds. The large decrease in CONH bonds and large increase in C-O bonds suggests the breaking of CONH bonds to form C-O bonds. The He/O_2 plasma treated nanofibers showed a substantial increase in surface oxygen content, as one would expect from oxygen plasma treatment. This is made even clearer by the drastic increase in C-O surface bonds (over 45% of the surface bonds). The large drop in C-N and CONH bonds accompanied by the creation of O-C=O bonds further shows that the He/O_2 plasma was very effective in oxygenating the nanofiber surface. The increased content of C-O and O-C=O bonds lead to improved reactivity of the nanofiber surfaces.

5.2.2 Peel Test Results

The adhesion strength between the nylon nanofibers and the fabric substrate was measured by a peel test method based on ASTM 2261 *Standard Test Method for Tearing Strength of Fabrics by the Tongue Procedure* using an Instron® Tensile Tester. To assure proper peeling and avoid slippage of the grip, tapes were attached to both the nanofiber mat and substrate fabric. The nanofiber mat was held by the moving grip while the fabric was held by the stationary grip. A 50 gram load cell was used to determine the maximum load required to remove the nanofiber mats from the fabric substrates at a constant rate of 50 mm/min.

Figure 5.3; Peel test sample (left) and sample being tested in the tensile tester (right)

The adhesion strength was measured in gram force and averaged over 20 specimens for the control, 100% He plasma, and He:O_2 plasma treatments. Table 5.2 shows the average adhesion strengths and standard deviations between the nanofiber mats and fabric substrates. It is clear that hybrid plasma treatment increased the adhesion between the nanofibers and fabrics.

Table 5.2; Average adhesion strengths in grams force along with standard deviations for untreated and plasma treated nanofiber mats

	Adhesion Strength (gf)
Control	1.51 ± 0.3
He plasma	2.74 ± 0.6
He/O_2 plasma	3.69 ± 0.9

The adhesive strength remains low (still on the order of a few grams), but the percentage increase is significant. This increased adhesion correlates to the increase in active surface functional groups shown by XPS analysis in Table 5.1. This indicates that there may be covalent bonding and cross-linking between the nanofiber mats and fabric substrates.

5.2.3 Flex Testing

The flex durability of the nanofiber mats was qualified using a Gelbo Flex test conducted based on ASTM F392-93 *Standard Test Method for Flex Durability of Flexible Barrier Materials*. The test was performed using an IDM Gelbo Flex Tester (IDM Instruments Ltd®) (shown in Figure 5.4).

Figure 5.4; Gelbo Flex Tester

The nanofiber deposited fabric samples were attached to the two disks with hose clamps. They were twisted and flexed for 1000 cycles and the adhesion was qualitatively assessed based on SEM images of the nanofiber/fabric surface. Typical SEM images of nanofiber/fabric surfaces before and after Gelbo Flex testing are shown in Figure 5.5.

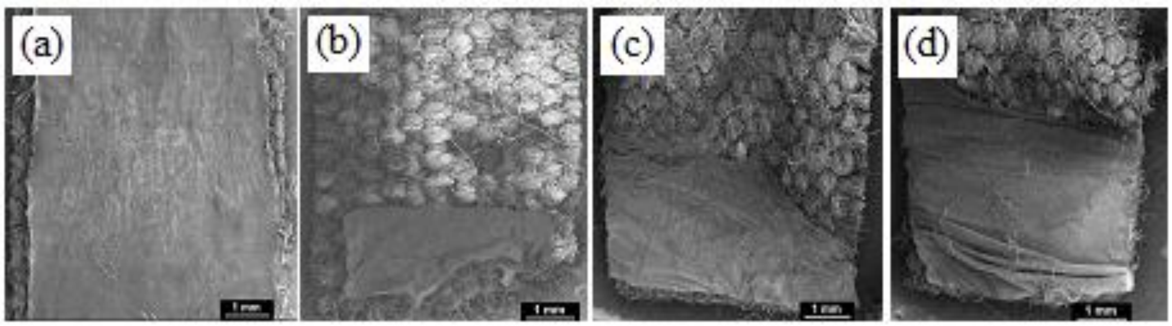

Figure 5.5; Typical SEM images of deposited nanofibers before (a) Gelbo Flex testing, and nanofibers hybrid electrospun with no plasma (b), He plasma (c), and He/O2 plasma (d) after 1000 cycles of flex testing

It is clear that the hybrid plasma treated nanofibers showed a higher resistance to peeling and tearing. Again, the treatment does not prevent the failure of the nanofiber/fabric interface, but the adhesion strength does show a marked increase from untreated samples when compared to He plasma treated samples. The adhesion is further increased for He/O_2 treated samples. These results correlate well to the increased adhesion strength shown in the peel test as well as the increase in active surface functional groups shown by XPS.

Chapter 6: Conclusions

The most important outcome of this research is the determination of the feasibility of combining electrospinning and atmospheric plasma treatment in a hybrid system efficient enough to electrospin nanofibers and expose them to atmospheric plasma for the purpose of developing protective cloths and mats. It was difficult to produce nanofibers in the presence of the electrical and physical interference from the plasma electrodes; however, a solution has been implemented and successfully operated. As the interference developed, especially between the electric fields of the electrospinner and that of the plasma dielectric barrier discharge (DBD), placing the plasma source out of the electrospinning path has provided the means by which the hybrid process achieved the desired operation. In order to do such implementation, the plasma was blown into the electrospinning path with the source to the side to treat the nanofibers in the afterglow of the plasma. Here in the afterglow plasma, the active species are mainly the plasma radicals and not the ions and electrons, which provide an abundance of excited atoms and molecules efficient enough to interact with the nanofibers and provide the desired treatment and lead to enhanced nanofiber/substrate properties. The design of the hybrid atmospheric plasma-electrospinning system has an advantage over the individual benefits of each separate system. The final design was achieved following a series of design features which started from electrospinning flowing into DBD plasma to finally injecting electrospinning into the plasma afterglow with the collection performed on a rotating drum. In this final design a slit with distributed holes allows for the continuous blowing of the plasma with the electric field of the electrospinner approximating a point charge source with the applied potential between the needle and the collection drum. Uniform homogeneous plasma is successfully generated along the source length.

The design of the hybrid system has an invention disclosure NCSU File Number 09-071, Filed for Provisional Patent Attorney File Nos. 61824 1230P1; 61824.01050.4, U.S. Provisional Patent Application Serial No. 61/445,333 on 21 February 2011.

Treatment of electrospun nanofibers in the hybrid system has shown that not only the adhesion between nanofibers and the fabric substrate was increased, but also the nanofibers themselves have shown increased strength and durability. The peel test of the treated samples has shown an increased adhesion strength from 1.51 grams force (gf) of the untreated samples to 2.74 gf with the in situ treatment of the nanofibers using only He as the working gas and increase to 3.69 gf for the treatment using 99%He/1%O_2 as the working gas, these results represent increases of 81% and 144%, respectively, which are excellent results when compared to plasma-only treatments and other techniques.

Another important result of this research is that the in situ treatment increased the nanofiber mats resistance to flex stresses. The apparent reason for such increase is attributed to surface oxygenation as evidential from XPS analysis. This oxygenation has likely led to increased hydrogen bonding and possible crosslinking between the polymer chains due to covalent bonds with oxygen as the binder. The C-O bonds on the nanofiber surfaces were also increased from zero to 17.4% for helium plasma and further increased to 45.4% for the He/O_2 plasma. This increased adhesion, strength, and durability is considered significant; however, higher levels should be achieved to be viable for protective clothing for warfare applications. The further increase may be achieved by increased exposure time, increased oxygen fraction or the addition of other reactive gases into the plasma formation. It is also important to obtain better understanding of the plasma mechanisms and the role of plasma active chemical species on the treatment process that control the surface modifications. In order to relate the surface processes to the plasma treatment, one must investigate the plasma at both the fundamental physics of non-thermal atmospheric plasmas and the experiment specific levels conducted during nanofiber treatment. The plasma was diagnosed electrically, thermally and optically to understand the fundamental characteristics such as electron temperature, electron number density, species present in the plasma, and the relative concentrations of those species.

A plasma equivalent circuit model was developed to simulate the DBD plasma as an electrical circuit, which can be compared to the actual electrical parameters of the experiment. The circuit model took into consideration the bulk plasma, the insulating parts of the DBD and the plasma sheaths. The model calculates the plasma temperature and number density using two different electron energy distribution functions (EEDF). The measured discharge current and voltage are used to compare the plasma impedance to the model impedance and to solve for the plasma parameters. Results of optical emission spectroscopy using the neutral bremsstrahlung technique with a Maxwellian EEDF showed good continuum matching for both He and He/O_2 plasmas. These continua showed electron temperatures very similar to those calculated using the equivalent circuit model. The helium discharge matches well to an average electron temperature of 2.8 eV, corresponding to

$2.0x10^7$ electrons/cm^3 and the He/O_2 discharge shows an electron temperature of 2.7 eV, corresponding to $1.16x10^7$ electrons/cm^3. This shows good correlation between electrical measurements and optical analysis which would allow for real time monitoring of the electron temperature via automatic solver of the plasma impedance of the equivalent circuit model using the real-time monitoring of the discharge current and voltage. Optical emission spectroscopy confirmed the existence of helium and oxygen lines in the discharge.

The chemical kinetics model shows that the electron number density affects only the magnitude of the species concentration and not its functionality, which is shown to depend mainly on the electron temperature. Graphs of species concentration versus temperature from this model can be used to show the relative changes in concentrations with the changes in electron temperature as measured in real time using the electrical measurements from the solver of the equivalent circuit model.

Recommendations for Future Work

Enhanced performance of hybrid atmospheric plasma-electrospinning system requires additional experimentation to optimize the system functionality for various applications.

Research focusing on the fundamental mechanisms of surface interaction that lead to strong adhesion is recommended as is the expansion of plasma diagnostics for the role of ionic species versus excited atoms and molecules. Other reactive and non-reactive gases can be experimented in the hybrid system to determine the effectiveness of other species on surface modifications and implementation of other desired features.

It is recommended to extend the measurements of optical emission spectroscopy with neutral bremsstrahlung and line intensity measurements with absolute calibration to correlate electron temperature to power levels and oxygen concentrations. These diagnostics would be beneficial if analysis could be automated such that calculation of the electron temperature could be seen in real time to monitor the behavior of the plasma with changes in electron population. The change in electron population correlates to the change in the population of the ionic species, which can also be an important role in surface modifications.

An expansion on the chemical kinetics model to include chemical kinetics and gas mixing in the region where treatment occurs, i.e. outside the plasma source in the afterglow/atmospheric air region where the electrospinning takes place, would add an insight on the chemical reactions of the excited atoms and molecules for second, third and higher order reactions. This, in turn, would allow for a good correlation of the active species and the XPS surface analysis and could be used for an optimization of the surface chemical changes at various oxygen concentrations and power levels. The chemical kinetics model should also be expanded to include other gases such as water vapor, N_2, CO_2, CF_4, Ar, etc. to examine other effects. This expanded model could be used to determine the viability of using chemical precursors such as CO_2 to enhance the nanofiber/substrate adhesion.

References

[1] Schutze, A., Jeong, J., Babayan, S., Park, J., Selwyn, G., & Hicks, R. (1998). The atmospheric-pressure plasma jet: a review and comparison to other plasma sources. IEEE Transactions on Plasma Science, 26(6), 1685-1694.

[2] Fridman, A., Chirokov, A., & Gutsol, A. (2005). Non-thermal atmospheric pressure discharges. Journal of Physics D: Applied Physics, 38, R1-R24.

[3] Andrady, A. L. (2005). *Science and Technology of Polymer Nanofibers*. John Wiley & Sons, Inc. Hoboken, NJ: John Wiley & Sons, Inc.

[4] Dalton, P. D., Grafahrend, D., Klinkhammer, K., Klee, D. & M. Moeller, M. (2007). Electrospinning of polymer melts: phenomenological observations. Polymer, 48.

[5] Sawicka, K. M. & Gouma, P. (2006). Electrospun composite nanofibers for functional applications, Journal of Nanoparticle Research, 8.

[6] Deitzel, J., Beck Tan, N. C., Kleinmeyer, J. D., Rehrmann, J., Tevault, D., Reneker, D. Sendijarevic, I., & McHugh, A. (1999). Generation of Polymer Nanofibers Through Electrospinning. Technical Report ARL-TR-1989, U.S. Army Research Laboratory, Aberdeen Proving Ground, MD.

[7] Subbiah, T., Bhat, G. S., Tock, R. W., Parameswaran, S., & Ramkumar, S. S. (2005). Electrospinning of nanofibers. Journal of Applied Polymer Science, 96.

[8] Doshi, J. & Reneker, D. H. (1995). Electrospinning process and applications of electrospun fibers. *Journal of Electrostatics*, 35, 151-160.

[9] Huang, C., Chen, S., Lai, C., Reneker, D. H., Qiu, H., Ye, Y. & Hou, H. (2006). Electrospun polymer nanofibres with small diameters. *Nanotechnology*, 17, 1558-1563.

[10] Fridrikh, S. V., Yu, J. H., Brenner, M. P. & Rutledge, G. C. (2003). Controlling the fiber diameter during electrospinning. *Physical Review Letters*, 90(14).

[11] Rutledge, G. C. & Fridrikh, S. V. (2007). Formation of fibers by electrospinning. *Advanced Drug Delivery Reviews*, 59, 1384-1391.

[12] Temmerman, E., Akishev, Y., Trushkin, N., Leys, C., & Vershuren, J. (2005). Surface modification with a remote atmospheric pressure plasma: dc glow discharge and surface streamer regime. Journal of Physics D: Applied Physics, 38, 505-509.

[13] Leroux, F., Perwuelz, A., Campagne, C., & Behary, N. (2006). Atmospheric air-plasma treatments of polyester textile structures. Journal of Adhesion Science and Technology, 20(9), 939-957.

[14] Karahan, H. & Ozdogan, E. (2008). Improvements of surface functionality of cotton fibers by atmospheric plasma treatment. Fibers and Polymers, 9(1), 21-26.

[15] De Geyter, N., Morent, R., Gengembre, L., Leys, C., Payen, E., Van Vlierberghe, S., & Schacht, E. (2008). Increasing the hydrophobicity of a PP film using a helium/CF4 DBD treatment at atmospheric pressure. Plasma Chemistry and Plasma Processing, 28, 289-298.

[16] Choi, J., Lee, E., Baik, H., Lee, S., Song, K., & Lim, Y. (2005). Analysis of polymer surface treated by dielectric barrier discharge. Plasma Sources Science and Technology, 14, 363-367.

[17] Gao, Z., Sun, J., Peng, S., Yao, L., & Qiu, Y. (2009). Surface modification of a polyamide 6 film by He/CF4 plasma using atmospheric pressure plasma jet. Applied Surface Science, 256, 1496-1501.

[18] Ho, K., Lee, A., & Bismarck, A. (2007). Fluorination of carbon fibres in atmospheric plasma. Carbon, 45, 775-784.

[19] Qiu, Y., Hwang, Y., Zhang, C., Bures, B., & McCord, M. (2002). Atmospheric pressure helium + oxygen plasma treatment of ultrahigh modulus polyethylene fibers. Journal of Adhesion Science and Technology, 16(4), 449-457.

[20] Kusano, Y., Anderson, T., & Michelsen, P. (2008). Atmospheric pressure plasma surface modification of carbon fibres. Journal of Physics: Conference Series, 100, 012002 1-4.

[21] Lommatzsch, U., Pasedag, D., Baalmann, A., Ellinghorst, G., & Wagner, H. (2007). Atmospheric pressure plasma jet treatment of polyethylene surfaces for adhesion improvement. Plasma Processes and Polymers, 4, S1041-S-1045.

[22] Park, J., Ju, W., Paek, K., Kim, Y., Choi, Y., Kim, J., & Hwang, Y. (2003). Pre-treatments of polymers by atmospheric pressure ejected plasma for adhesion improvement. Surface and Coatings Technology, 174-175, 547-552.

[23] Kan, C., Yuen, C., & Tsoi, W. (2011). Using atmospheric pressure plasma for enhancing the deposition of printing paste on cotton fabric for digital ink-jet printing. Cellulose, 18, 827-839.

[24] Gorensek, M., Gorjanc, M, Bukosek, V., Kovac, J., Jovancic, P., & Mihailovic, D. (2010). Functionalization of PET fabrics by corona and nano silver. Textile Research Journal, 80(3), 253-262.

[25] Mori, Y., Yamauchi, K., Yamamura, K., & Sano, Y. (2000). Development of plasma chemical vaporization machining. Review of Scientific Instruments, 71(12), 4627-4632.

[26] Sano, Y., Kato, T., Yamamura, K., Mimura, H., Matsuyama, S., & Yamauchi, K. (2010). Beveling of silicon carbide wafer by plasma etching using atmospheric-pressure plasma. Japanese Journal of Applied Physics, 49, 08JJ03 1-4.

[27] Tu, V., Jeong, J., Schutze, A., Babayan, S., Ding, G., Selwyn, G., & Hicks, R. (2000). Tantalum etching with a nonthermal atmospheric-pressure plasma. Journal of Vacuum Science and Technology, 18(6), 2799-2805.

[28] Karahan, H., Ozdogan, E., Demir, A., Kocum, I., Oktem, T., & Ayhan, H. (2009). Effects of atmospheric pressure plasma treatments on some physical properties of wool fibers. Textile Research Journal, 79(14), 1260-1265.

[29] Thiebaut, J., Belmonte, T., Chaleix, D., Choquet, P., Baravian, G., Puech, V., & Michel, H. (2003). Comparison of surface cleaning by two atmospheric pressure discharges. Surface and Coatings Technology, 169-170, 186-189.

[30] Goossens, O., Dekempeneer, E., Vangeneugden, D., Van de Leest, R., & Leys, C. (2001). Application of atmospheric pressure dielectric barrier discharges in deposition, cleaning and activation. Surface and Coatings Technology, 142-144, 474-481.

[31] Jung, M. & Choi, H. (2006). Photoresist etching using Ar/O2 and He/O2 atmospheric pressure plasma. Thin Solid Films, 515, 2295-2302.

[32] Cai, Z., Qiu, Y., Zhang, C., Hwang, Y., & McCord, M. (2003). Effect of atmospheric plasma treatment on desizing of PVA on cotton. Textile Research Journal, 73(8), 670-674.

[33] Wang, B., Zhao, Q., Wang, L., & Dong, S. (2006). Application of atmospheric pressure plasma in the ultrasmooth polishing of SiC optics. Materials Science Forum, 532-533, 504-507.

[34] Detrick, M., Washington, G., & Subramanian, V. (2003). Control of polishing of diamond films using microactuation and an atmospheric pressure plasma. IEEE/ASME Transactions on Mechatronics, 8(1), 45-55.

[35] Korotkov, R., Gupta, R., Ricou, P., Smith, R., & Silverman, G. (2008). Atmospheric plasma discharge chemical vapor deposition of SnOx thin films using various tin precursors. Thin Solid Films, 516, 4720-4727.

[36] Zhang, X. & Han, G. (2008). Microporous textured titanium dioxide films deposited at atmospheric pressure using dielectric barrier discharge assisted chemical vapor deposition. Thin Solid Films, 516, 6140-6144.

[37] Foest, R., Adler, F., Sigeneger, F., & Schmidt, M. (2003). Study of an atmospheric pressure glow discharge (APG) for thin film deposition. Surface and Coatings Technology, 163-164, 323-330.

[38] Nattinen, K., Nikkola, J., Minkkinen, H., Heikkila, P., Lavonen, J., & Tuominen, M. (2011). Reel-to-reel inline atmospheric plasma deposition of hydrophobic coatings. Journal of Coatings Technology and Research, 8(2), 237-245.

[39] Morent, R., De Geyter, N., Van Vlierberghe, S., Vanderleyden, E., Dubruel, P., Leys, C., & Schacht, E. (2009). Deposition of polyacrylic acid films by means of an atmospheric pressure dielectric barrier discharge. Plasma Chemistry and Plasma Processing, 29, 103-117.

[40] Nozaki, T., Kimura, Y., & Okazaki, K. (2002). Carbon nanotubes deposition in glow barrier discharge enhanced catalytic CVD. Journal of Physics D: Applied Physics, 35, 2779-2784.

[41] Jiang, X., Rui, Y., & Chen, G. (2009). Improved properties of cotton by atmospheric pressure plasma polymerization deposition of sericin. Journal of Vinyl & Additive Technology, 15, 129-133.

[42] Hossain, M. M., Hegemann, D., Fortunato, G., Herrmann, A. S., & Heuberger, M. (2007). Plasma deposition of permanent superhydrophilic a-C:H:N films on textiles. *Plasma Processes and Polymers*, 4(4), 471-481.

[43] Yaman, N., Ozdogan, E., Seventekin, N., & Ayhan, H. (2009). Plasma treatment of polypropylene fabric for improved dyeability with soluble textile dyestuff. *Applied Surface Science*, 255(15), 6764-6770.

[44] Bai, G. & Liu, Y. (2010). Antistatic property of polyacrylonitrile fiber by plasma-grafting treatment. *Textile Research Journal*, 80(16), 1658-1664.

[45] Tseng, H. J. , Hsu, S. , Wu, M. W. , Hsueh, T. H. , & Tu, P. C. (2009). Nylon textiles grafted with chitosan by open air plasma and their antimicrobial effect. *Fibers and Polymers*, 10(1), 53-59.

[46] Fang, J., Niu, H., Lin, T., & Wang, X. (2008). Applications of electrospun nanofibers. Chinese Science Bulletin, 53(15), 2265-2286.

[47] Patanaik, A., Jacobs, V., & Anandjiwala, R. (2010). Performance evaluation of electrospun nanofibrous membrane. Journal of Membrane Science, 352, 136-142.

[48] Gopal, R., Kaur, S., Ma, Z., Chan, C., Ramakrishna, S., & Matsuura, T. (2006). Electrospun nanofibrous filtration membrane. Journal of Membrane Science, 281, 581-586.

[49] Sang, Y., Gu, Q., Sun, T., Li, F., & Liang, C. (2008). Filtration by a novel nanofiber membrane and alumina adsorption to remove copper(II) from groundwater. Journal of Hazardous Materials, 153, 860-866.

[50] Shin, C., Chase, G., & Reneker, D. (2005). Recycled expanded polystyrene nanofibers applied in filter media. Colloids and Surfaces A: Physicochemical and Engineering Aspects, 262, 211-215.

[51] Gibson, P., Schreuder-Gibson, H., & Rivin, D. (2001). Transport properties of porous membranes based on electrospun nanofibers. Colloids and Surfaces A: Physicochemical and Engineering Aspects, 187-188, 469-481.

[52] Qin, X. & Wang, S. (2006). Filtration properties of electrospinning nanofibers. Journal of Applied Polymer Science, 102, 1285-1290.

[53] Vitchuli, N., Shi, Q., Nowak, J., McCord, M., Bourham, M., & Zhang, X. (2010). Electrospun ultrathin nylon fibers for protective applications. Journal of Applied Polymer Science, 116, 2181-2187.

[54] Uyar, T., Havelund, R., Nur, Y., Hacaloglu, J., Besenbacher, F., & Kingshott, P. (2009). Journal of Membrane Science, 332, 129-137.

[55] Zhang, H., Wu, C., Zhang, Y., White, C., Xue, Y., Nie, H., & Zhu, L. (2010). Elaboration, characterization and study of a novel affinity membrane made from electrospun hybrid chitosan/nylon -6 nanofibers for papain purification. Journal of Materials Science, 45, 2296-2304.

[56] Ma, Z., Kotaki, M., & Ramakrishna, S. (2005). Electrospun cellulose nanofiber as affinity membrane. Journal of Membrane Science, 265, 115-123.

[57] Cho, D., Zhou, H., Cho, Y., Audus, D., & Joo, Y. (2010). Structural properties and superhydrophobicity of electrospun polypropylene fibers from solution and melt. Polymer, 51, 6005-6012.

[58] Cui, W., Li, X., Zhou, S., & Weng, J. (2008). Polymer Degradation and Stability, 93, 731-738.

[59] Ma, M., Hill, R., Lowery, J., Fridrikh, S., & Rutledge, G. (2005). Electrospun poly(styrene-block-dimethylsiloxane) block copolymer fibers exhibiting superhydrophobicity. Langmuir, 21, 5549-5554.

[60] Yoon, H., Park, J., & Kim, G. (2010). A superhydrophobic surface fabricated by an electrostatic process. Macromolecular Rapid Communications, 31, 1435-1439.

[61] Cengiz, U., Avci, M., Erbil, Y., & Sarac, A. (2012). Superhydrophobic terpolymer nanofibers containing perfluoroethyl alkyl methacrylate by electrospinning. Applied Surface Science, 258, 5815-5821.

[62] Ma, M., Mao, Y., Gupta, M., Gleason, K., & Rutledge, G. (2005). Superhydrophobic fabrics produced by electrospinning and chemical vapor deposition. Macromolecules, 38, 9742-9748.

[63] Han, D. & Steckl, A. (2009). Superhydrophobic and oleophobic fibers by coaxial electrospinning. Langmuir, 25(16), 9454-9462.

[64] Sahu, R., Sinha-Ray, S., Yarin, A., & Pourdeyhimi, B. (2012). Drop impacts on electrospun nanofiber membranes. Soft Matter, 8, 3957-3970.

[65] Bagherzadeh, R., Latifi, M., Najar, S., Tehran, M., Gorji, M., & Kong, L. (2011). Transport properties of multi-layer fabric based on electrospun nanofiber mats as a breathable barrier textile material. Textile Research Journal, 82(1), 70-76.

[66] Lee, S. & Obendorf, S. (2007). Use of electrospun nanofiber web for protective textile materials as barriers to liquid penetration. Textile Research Journal, 77(9), 696-702.

[67] Park, S., Bae, H., Xing, Z., Kwon, O., Huh, M., & Kang, I. (2009). Preparation and properties of silver-containing nylon 6 nanofibers formed by electrospinning. Journal of Applied Polymer Science, 112, 2320-2326.

[68] Shi, Q., Vitchuli, N., Nowak, J., Caldwell, J., Breidt, F., Bourham, M., Zhang, X., & McCord, M. (2011). Durable antibacterial Ag/polyacrylonitrile (Ag/PAN) hybrid nanofibers prepared by atmospheric plasma treatment and electrospinning. European Polymer Journal, 47, 1402-1409.

[69] Pant, H., Bajgai, M., Nam, K., Seo, Y., Pandeya, D., Hong, S., & Kim, H. (2011). Electrospun nylon-6 spider-net like nanofiber mat containing TiO2 nanoparticles: a multifunctional nanocomposite textile material. Journal of Hazardous Materials, 185, 124-130.

[70] Vitchuli, N., Shi, Q., Nowak, J., Kay, K., Caldwell, J., Breidt, F., Bourham, M., McCord, M., & Zhang, X. (2011). Multifunctional ZnO/Nylon 6 nanofiber mats by an electrospinning-electrospraying hybrid process for use in protective applications. Science and Technology of Advanced Materials, 12, 055004 1-7.

[71] Sundarrajan, S. & Ramakrishna, S. (2007). Fabrication of nanocomposite membranes from nanofibers and nanoparticles for protection against chemical warfare simulants. Journal of Materials Science, 42, 8400-8407.

[72] Ramaseshan, R. & Ramakrishna, S. (2007). Zinc titanate nanofibers for the detoxification of chemical warfare simulants. Journal of the American Ceramic Society, 90(6), 1836-1842.

[73] Bures, B. (2004). Rapid mortality of pest arthropods by direct exposure to a dielectric barrier discharge. (Doctoral dissertation). North Carolina State Univ., Raleigh, NC.

[74] Park, J., Henins, I., Herrmann, H., & Selwyn, G. (2000). Neutral bremsstrahlung measurement in an atmospheric-pressure radio frequency discharge. Physics of Plasmas, 7(8), 3141-3144.

[75] Dalgarno, A. & Lane, N. (1966). Free-free transitions of electrons in gases. American Astronomical Society, 145(6), 623-633.

[76] NIST Atomic Spectra Database, NIST Standard Reference Database #78. Version 5 September 2012.

[77] Pearse, R. W. B. & Gaydon A. G. (1963). The identification of molecular lines. New York: Wiley.

[78] Jackson, J. D. (1999). *Classical electrodynamics*. New York: Wiley.

[79] Hutchinson, I. H. (2002). *Principles of plasma diagnostics*. New York: Cambridge University Press.

[80] Lochte-Holtgreven, W. (1995). *Plasma diagnostics*. New York: AIP Press.

[81] Oliver, B., Smy, P., & Clements, R. (1974). Small-sigmal transit-time analysis of a planar mobility-dominated ion sheath. Journal of Applied Physics, 45(12), 5245-5250.

[82] Kuo, K. K. (2005). Principles of Combustion. New York: Wiley.

[83] Shon, J. & Kushner, M. (1994). Excitation mechanisms and gain modeling of the high-pressure atomic Ar laser in He/Ar mixtures. Journal of Applied Physics, 75(4), 1883-1890.

[84] Zygelman, B. (1991). Radiative deexcitation of singlet metastable helium by collisions with helium atoms. *Physical Review A*, 43(1), 575-577.

[85] Yuan, X. & Raja, L. (2003). Computational study of capacitively coupled high-pressure glow discharges in helium. IEEE Transactions on Plasma Science, 31(4), 495-503.

[86] Stafford, D. & Kushner, M. (2004). O2(1Δ) production in He/O2 mixtures in flowing low pressure plasmas. Journal of Applied Physics, 96(5), 2451-2465.

[87] Stalder, K., Vidmar, R., Nersisyan, G., & Graham, W. (2006). Modeling the chemical kinetics of high-pressure glow discharges in mixtures of helium with real air. Journal of Applied Physics, 99, 093301 1-7.

[88] Niemi, K., Reuter, S., Graham, L., Waskoenig, J., Knake, N., Schulz-von der Gathen, V., & Gans, T. (2010). Diagnostic based modeling of radio-frequency driven atmospheric pressure plasmas. Journal of Physics D: Applied Physics, 43, 124006 1-6.

[89] Crompton, R., Elford, M., & Robertson, A. (1970). The momentum transfer cross section for electrons in helium derived from drift velocities at 77K. Australian Journal of Physics, 23, 667-681.

[90] Milloy, H. & Crompton, R. (1977). Momentum-transfer cross section for electron-helium collisions in the range 4-12 eV. Physical Review A, 15, 1847-1850.

[91] Hayashi, M. (1981). Report No. IPPJ-AM-19. Institute of Plasma Physics, Nagoya University.

[92] Walsh, J., Liu, D., Iza, F., Rong, M., & Kong, M. (2010). Contrasting characteristics of sub-microsecond pulsed atmospheric air and atmospheric pressure helium-oxygen glow discharges. Journal of Physics D: Applied Physics, 43, 032001 1-7.

[93] Golubovskii, Y., Maiorov, V., Behnke, J., & Behnke, J. F. (2003). Modeling of the homogeneous barrier discharge in helium at atmospheric pressure. Journal of Physics D: Applied Physics, 36, 39-49.

[94] Lieberman, M. A., & Lichtenberg, A. J. (1994). *Principles of plasma discharges and materials processing.* New York: Wiley.

[95] Gudmundsson, J. (2002). Global model of plasma chemistry in a low-pressure O2/F2 discharge. Journal of Physics D: Applied Physics, 35, 328-341.

[96] Jeong, J., Park, J., Henins, I., Babayan, S., Tu, V, Selwyn, G., Ding, G., & Hicks, R. (2000). Reaction chemistry in the afterglow of an oxygen-helium, atmospheric pressure plasma. Journal of Physical Chemistry A, 104, 8027-8032.

[97] Park, G., Hong, Y., Lee, H., Sim, J., & Lee, J. (2010). A global model for the identification of the dominant reactions for atomic oxygen in He/O2 atmospheric-pressure plasmas. Plasma Processes and Polymers, 7, 281-287.

APPENDICES

Appendix A: Momentum Transfer Cross-Section

The electron momentum transfer cross-section data for O2 is from JILA report No. 26 [JILA 26] and can be found in Table A.1. The He data is from Crompton et al. [89], Milloy & Crompton [90], and Hayashi [91] and can be found in Table A.2. These data were fit using the least Chi-squared fitting code CURMOD. The data was fit over the interval from ~1.24 eV (the lowest energy over which the integral in Eqn 3-3 is taken) to 100 eV (at which point the EEDs become so small that the integrals become negligible, i.e. less than .1% of the total integral). The momentum transfer cross-section equations (in cm^2) used for He and O_2 are shown below.

$$q_0(x)_{He} = \left[3.389e^{-.034x} - 33.54e^{-3.955x} + 3.337e^{-.0059x^2} - 4.6\ 10^{-4}x + .6\right]10^{-16}$$

$$q_0(x)_{O_2} = \left[2.507e^{-.08097x} - 3.95e^{-.0426(x-4.76)^2} - 1.16e^{-.3365(x-3.01)^2} - .019x + 8.38\right]10^{-16}$$

Table A.1; Momentum Transfer Cross-Sections for He

E (eV)	q_m (cm^2 10^{-16})
1.2	6.91
1.3	6.92
1.5	6.96
1.7	6.97
1.9	6.98
2.1	6.98
2.2	6.98
2.5	6.96
2.8	6.92
3	6.89
3.3	6.82
3.6	6.73
4	6.6
4.5	6.49
5	6.31
6	6
7	5.68
8	5.35
10	4.72
12	4.2
15	3.5
17	3.15
20	2.64
25	2.05
30	1.74
50	1.1
75	0.88
100	0.75

Table A.2; Momentum Transfer Cross-Sections for O_2

E (eV)	q_m (cm^2 10^{-16})
1	7.2
1.2	7.9
1.3	7.9
1.5	7.6
1.7	7.3
1.9	6.9
2.1	6.6
2.2	6.5
2.5	6.1
2.8	5.8
3	5.7
3.3	5.5
3.6	5.45
4	5.5
4.5	5.55
5	5.6
6	6
7	6.6
8	7.1
10	8
12	8.5
15	8.8
17	8.7
20	8.6
25	8.2
30	8
50	7.7
75	6.8
100	6.5

Appendix B: Neutral Bremsstrahlung Continuum Code

One of the four (He Max, He Dru, He/O2 Max, and He/O2 Dru) codes used to generate theoretical neutral bremsstrahlung continua for comparison with experimental data are contained here. They solve the integral in Eqn 3-3 at individual wavelength and average electron energy combinations. This data can then be plotted versus wavelength at various electron temperatures in order to match the continuum shape. When divided by the experimental continuum they solve for the electron number density at that temperature.

Neutral Bremsstrahlung Solution for He/O2 with a Maxwellian EEDF

Set Physical Constants and Inputs

$re := 2.818\times 10^{-15}$ $\quad P := 101325$ $\quad To := 300$

$c1 := 3\cdot 10^{8}$

$Ngas := \frac{P}{1.38065\cdot 10^{-23}\cdot To\cdot 100^{3}}$

$me := \frac{511000}{c1^{2}}$

$v(E) := \left(\sqrt{2\cdot\frac{E}{me}}\right)$ $\quad hv(\lambda) := \frac{1240}{\lambda}$

Set Values for Momentum Transfer Equations

$a1 := .03401$ $\quad b1 := .080965$

$a2 := .00589$ $\quad b2 := .042646$

$a3 := 3.9550$ $\quad b3 := 4.7615$

$a4 := 3.3888$ $\quad b4 := .33650$

$a5 := 3.3374$ $\quad b5 := 3.0102$ $\quad b9 := -.019090$

$a6 := -33.542$ $\quad b6 := 2.5067$ $\quad b10 := 8.3785$

$a7 := -.00045973$ $\quad b7 := -3.9505$

$a8 := .59904$ $\quad b8 := -1.1560$

$$qo(x) := \left(a4\cdot e^{-a1\cdot x} + a5\cdot e^{-a2\cdot x^{2}} + a6\cdot e^{-a3\cdot x} + a7\cdot x + a8\right)\cdot 10^{-16}$$

$$qo2(x) := \left[b6\cdot e^{-b1\cdot x} + b7\cdot e^{-b2\cdot (x-b3)^{2}} + b8\cdot e^{-b4\cdot (x-b5)^{2}} + b9\cdot x + b10\right]\cdot 10^{-16}$$

Set Values for Sigma and f

$$G1(E,\lambda) := \left[\left[qo(E - hv(\lambda)) + \left(1 - \frac{hv(\lambda)}{E}\right)\cdot qo(E)\right]\cdot .99 + \left[qo2(E - hv(\lambda)) + \left(1 - \frac{hv(\lambda)}{E}\right)\cdot qo2(E)\right]\cdot .01\right]$$

$$sigma(E,\lambda) := 8\cdot\frac{re}{(3\cdot c1\cdot hv(\lambda))}\cdot E\cdot\sqrt{1 - \frac{hv(\lambda)}{E}}\cdot G1(E,\lambda)$$

$$f(E,kT) := 2\cdot\sqrt{\frac{E}{\pi\cdot(kT)^3}}\cdot e^{\frac{-E}{kT}}$$

Solve for the integral Q

$\lambda := 200, 300 .. 1000$

$kT := .4, .5 .. 3$

$$Q(\lambda,kT) := hv(\lambda)\cdot\int_{hv(\lambda)}^{\infty} v(E)\cdot sigma(E,\lambda)\cdot f(E,kT)\,dE\cdot Ngas$$

$$Qv(\lambda,kT) := Q(\lambda,kT)\cdot\frac{c1}{\lambda^2}$$

$$Qf(\lambda,kT) := Qv(\lambda,kT)\cdot 1.602210^{-19}\cdot\frac{100\cdot 1\cdot 10^6}{1\cdot 10^{-9}} \qquad \frac{\mu W}{cm^2\cdot nm}$$

Appendix C: Equivalent Circuit Model Code

Because the circuit model equations (Eqn 4.21a and b) contain multiple functions of both n_e and T_e, the equations cannot be solved directly. Instead, a code was written to solve for *Re(Z)* and *Im(Z)* at any combination of temperature and number density. These were plotted as functions of n_e and T_e and solutions exist where they intersect at 1 (corresponding to *R=Re(Z)* or *X=Im(Z)*). There are multiple solutions which satisfy either *R=Re(Z)* or *X=Im(Z)*, but only one set of n_e and T_e that satisfies both. The relative ion concentrations were iterated along with the chemical kinetics code which showed that in the He plasma He^+ was dominant and in the He/O_2 plasma O_2^+ was dominant.

Set Dimensions, Physical Constants, and Inputs

$me := 9.1094 10^{-31}$

$h := 6.62607 10^{-34}$

$k := 1.380651 0^{-23}$

$q := 1.6022 10^{-19}$

$E0 := 8.854 10^{-12}$

$mHe := 6.6465 10^{-27}$

$mO := 16 \cdot amu$

$mO2 := 32 \cdot amu$

$Vo := 5096.$

$Io := .014$

$phi := 1.41371 + \frac{\pi}{2}$

$w := 110002 \cdot \pi$

$r := .1$

$th := \frac{.0254}{8}$

$Ax := r \cdot th$

$dg := \frac{.0254}{16}$

$dpe := .0002$

$kg := 5$

$kpe := 2.$

$nn := 2.446 10^{25}$

$amu := 1.66054 10^{-27}$

$XO := 0$

$XO2 := 1.$

$XHe := 1 - XO - XO2$

$X := .1$

$ds := X \cdot 3 \cdot \frac{.0254}{32}$

$dp := \frac{3 \cdot .0254}{32} - ds$

Set Values for ne and Te

$i := 1..200$

$j := 1, 2..50$

$ne_i := i \cdot 10^{13}$

$Te_j := \frac{j}{10}$

Set ne and Te Dependent parameters

$$mI := XHe \cdot mHe + XO \cdot mO + XO2 \cdot mO2$$

$$wpi_i := \sqrt{q^2 \cdot \frac{(.5ne)_i}{E0 \cdot mI}} \qquad vB_j := \sqrt{\frac{k \cdot 350}{mI}} \qquad v := \sqrt{\frac{8 \cdot k \cdot 300}{\pi \cdot mI}} \qquad vi_i := \frac{1}{\sqrt{2}} \cdot \frac{Io}{Ax \cdot q \cdot ne_i}$$

$$wpe_i := \sqrt{q^2 \cdot \frac{ne_i}{E0 \cdot me}} \qquad ti_i := \frac{ds}{v} \qquad \sigma in := \pi \cdot \left(124 \cdot 10^{-12}\right)^2$$

$$vin_i := nn \cdot \sigma in \cdot v$$

$$wp_i := wpe_i \qquad \mu_i := \frac{q}{mI \cdot vin_i}$$

$$ven_j := nn \cdot \sqrt{\frac{8 \cdot Te_j \cdot q}{\pi \cdot me}} \cdot 6.9 \cdot 10^{-20} \qquad \alpha_i := \frac{E0}{ne_i \cdot q \cdot \mu_i \cdot (ti_i)}$$

Solve for Dielectric, Sheath, and Plasma Reactance and Resistance

$$Ash_{i,j} := 0 \qquad Ap_{i,j} := \frac{dp}{w \cdot E0 \cdot Ax} \cdot \frac{\left[-w \cdot (wp_i)^2 \cdot ven_j\right]}{\left[(wp_i)^2 - w^2\right]^2 + w^2 \cdot (ven_j)^2}$$

$$Bsh_i := \frac{ds \cdot 2 \cdot \alpha_i}{Ax \cdot E0 \cdot w \cdot (1 + 2 \cdot \alpha_i)}$$

$$Bp_{i,j} := \frac{-dp}{w \cdot E0 \cdot Ax} \cdot \frac{\left[w^2 \cdot (wp_i)^2 - w^4 - w^2 \cdot (ven_j)^2\right]}{\left[(wp_i)^2 - w^2\right]^2 + w^2 \cdot (ven_j)^2}$$

$$Bd := \frac{-1}{w \cdot E0 \cdot Ax} \cdot \left(\frac{dg}{kg} + \frac{dpe}{kpe}\right)$$

Total Impedance

$$A_{i,j} := Ash_{i,j} + Ap_{i,j} \qquad B_{i,j} := Bd + Bp_{i,j} + Bsh_i$$

Resistance and Reactance Ratios

$$Alpha := \frac{Vo}{Io} \cdot \cos(phi) \qquad Beta := \frac{Vo}{Io} \cdot \sin(phi)$$

$$R_{i,j} := \frac{A_{i,j}}{Alpha} \qquad \chi_{i,j} := \frac{B_{i,j}}{Beta}$$

Appendix D: Chemical Kinetics Model Code

The chemical kinetics code can be used with either He or He/O_2 feed gases. An explanation of the iterative solution method can be found in Section 4.2.1. The rate constant equations have been left out as they are shown far more elegantly in Appendix E.

```
function [NHe,NHem,NHep,NHe2m,NHe2p,NO2,NO2m,NO2p,NO2n,NO,NOm,NOp,NOn,NO3,NNe] =
CKHeO2(x,y,z)

% Temperatures
   Te=.5*x;
   T=300;
   To=T/300;
   P=101325;
   R=8.314;
% Wall
   Axy=18*1.3;
   S=Axy*100/4*sqrt(2*1.38065E-23*T/1.66054E-27);

% Flow In & Out
   V=18*3*2.54*1.3/32;
   NA=6.0221415E23;
   sccs=20/60;
   FI=NA*sccs/V/22.4;
   FO=sccs/V*1000;

% Initial values
k=1
Chi=1;
S1=1E5;

He(k)=1E19;
Hem(k)=S1;
Hep(k)=100;
He2m(k)=S1;
He2p(k)=S1;

O2(k)=1E17;
O2m(k)=0;
O2p(k)=S1;
O2n(k)=0;
O(k)=S1;
Om(k)=0;
Op(k)=S1;
On(k)=0;
O3(k)=S1;
M(k)=S1;
Ne(k)=Hep(k)+O2p(k)+Op(k)-O2n(k)-On(k);
dN(k)=1;

while abs(dN(k))>.001
   Ne(k)=sqrt(10)^y;

   HeGain(k)=.99*FI+k3*Hem(k)*He(k)+k4*Ne(k)*Hem(k)+k5*Hem(k)*Hem(k)...
      +k10*He2p(k)*Ne(k)+2*k15*He2p(k)*Ne(k)*Ne(k)+2*k16*He2p(k)*Ne(k)...
      +2*k17*He2p(k)*Ne(k)*He(k)+2*k18*He2m(k)*He2m(k)+k19*On(k)*Hep(k)...
      +k20*O2n(k)*Hep(k)+k21*On(k)*Hep(k)*M(k)+k22*Hem(k)*O2(k)...
```

```
    +k23*Hem(k)*O3(k)+k24*Hem(k)*O(k)+k25*Hem(k)*Om(k)+k26*Hep(k)*O2(k)...
    +k27*Hep(k)*O3(k)+k28*Hep(k)*O2(k)+k29*Hep(k)*O2m(k)+k30*Hep(k)*O2m(k)...
    +k31*Hep(k)*O(k)+k32*Hep(k)*Om(k)+2*k33*He2m(k)*O2(k)+2*k34*He2m(k)*O2(k)...
    +2*k35*He2p(k)*O2(k)+2*k36*He2p(k)*O2(k)+kw1*Hem(k)+kw2*Hep(k);
HeLoss(k)=FO+k1*Ne(k)+k2*Ne(k)+k11*Hep(k)*He(k)+k13*Hem(k)*He(k);
He(k+1)=HeGain(k)/HeLoss(k);

O2Gain(k)=0.01*FI+k20*O2n(k)*Hep(k)+k27*Hep(k)*O3(k)+k38*On(k)*O2p(k)...
    +k39*On(k)*O(k)+k40*Ne(k)*O2m(k)+k41*O2m(k)*O2(k)+k42*O2m(k)*O(k)...
    +k43*Ne(k)*O3(k)+2*k44*O2n(k)*O2p(k)+k45*O2n(k)*Op(k)+2*k46*O3(k)*O(k)...
    +k47*Ne(k)*Ne(k)*O2p(k)+k48*Ne(k)*O2p(k)*O2(k)+k49*O(k)*O(k)*O(k)...
    +k50*On(k)*Op(k)*O2(k)+k51*O(k)*Om(k)*O2(k)+2*k52*O2n(k)*O2p(k)...
    +k53*O2n(k)*O2p(k)+2*k54*On(k)*O3(k)+k55*On(k)*O3(k)+k56*O2n(k)*O(k)...
    +2*k57*O2n(k)*O2m(k)+k58*Op(k)*O3(k)+k59*Om(k)*O3(k)+2*k60*Om(k)*O3(k)...
    +2*k61*O2m(k)*O2m(k)+2*k62*O2m(k)*O3(k)+k63*O2m(k)*He(k)+k64*Ne(k)*O3(k)...
    +k65*On(k)*O2p(k)*M(k)+k66*O(k)*O(k)*He(k)+k67*O(k)*O(k)*O2(k)...
    +k68*O3(k)*He(k)+k69*O3(k)*O(k)+k70*O3(k)*O2(k)+k71*O3(k)*O3(k)...
    +k72*O2m(k)+k124*O2n(k)*M(k)+kw4*O2m(k)+.5*kw5*O(k)+kw6*O2p(k)+kw7*O2n(k);
O2Loss(k)=FO+k22*Hem(k)+k26*Hep(k)+k28*Hep(k)+k33*He2m(k)+k34*He2m(k)...
    +k35*He2p(k)+k36*He2p(k)+k37*He2p(k)+k73*Ne(k)+k74*Ne(k)+k75*Ne(k)...
    +k76*Ne(k)+k77*Ne(k)+k78*Op(k)+k79*Ne(k)+k80*Ne(k)+k81*Om(k)...
    +k82*On(k)+k83*Ne(k)*M(k)+k84*O2m(k)+k85*O(k)*He(k)+k86*O(k)*O2(k)...
    +k87*O(k)*O(k)+k88*O(k)*O3(k);
O2(k+1)=O2Gain(k)/O2Loss(k);

HemGain(k)=k1*Ne(k)*He(k)+k6*Ne(k)*Hep(k)+k7*Ne(k)*Ne(k)*Hep(k)...
    +k10*He2p(k)*Ne(k);
HemLoss(k)=FO+k3*He(k)+k4*Ne(k)+2*k5*Hem(k)+k8*Ne(k)+k13*He(k)*He(k)...
    +2*k14*Hem(k)+k22*O2(k)+k23*O3(k)+k24*O(k)+k25*Om(k)+kw1;
Hem(k+1)=HemGain(k)/HemLoss(k);

HepGain(k)=k2*Ne(k)*He(k)+k5*Hem(k)*Hem(k)+k8*Ne(k)*Hem(k);
HepLoss(k)=FO+k6*Ne(k)+k7*Ne(k)*Ne(k)+k11*He(k)*He(k)+k19*On(k)+k20*O2n(k)...
    +k21*On(k)*M(k)+k26*O2(k)+k27*O3(k)+k28*O2(k)+k29*O2m(k)+k30*O2m(k)...
    +k31*O(k)+k32*Om(k)+kw2;
Hep(k+1)=HepGain(k)/HepLoss(k);

O2mGain(k)=k79*Ne(k)*O2(k)+k81*Om(k)*O2(k)+k111*O(k)*O(k)*O2(k)...
    +k112*O(k)*O(k)*O(k)+k113*O(k)*O(k)*He(k);
O2mLoss(k)=FO+k29*Hep(k)+k30*Hep(k)+k40*Ne(k)+k41*O2(k)+k42*O(k)...
    +k57*O2n(k)+2*k61*O2m(k)+k62*O3(k)+k63*He(k)+k72+k84*O2(k)+k93*Ne(k)...
    +k94*On(k)+k104*Ne(k)+k119*On(k)+k120*Ne(k)*O2(k)+k121*Ne(k)*O(k)...
    +k123*Ne(k)+kw4;
O2m(k+1)=O2mGain(k)/O2mLoss(k);

O2nGain(k)=k55*On(k)*O3(k)+k83*Ne(k)*O2(k)*M(k)+k94*On(k)*O2m(k)+k98*Ne(k)*O3(k)...
    +k120*Ne(k)*O2m(k)*O2(k)+k121*Ne(k)*O2m(k)*O(k);
O2nLoss(k)=FO+k20*Hep(k)+k44*O2p(k)+k45*Op(k)+k52*O2p(k)*O2(k)+k53*O2p(k)...
    +k56*O(k)+k57*O2m(k)+k110*O(k)+k114*O(k)*O(k)+k118*Op(k)*M(k)+k124*M(k)+kw7;
O2n(k+1)=O2nGain(k)/O2nLoss(k);
```

```
O2pGain(k)=k22*Hem(k)*O2(k)+k23*Hem(k)*O3(k)+k28*Hep(k)*O2(k)+k30*Hep(k)*O2m(k)...
    +k34*He2m(k)*O2(k)+k35*He2p(k)*O2(k)+k37*He2p(k)*O2(k)+k58*Op(k)*O3(k)...
    +k75*Ne(k)*O2(k)+k78*Op(k)*O2(k)+k109*O(k)*Op(k)*M(k)+k123*Ne(k)*O2m(k);
O2pLoss(k)=FO+k38*On(k)+k44*O2n(k)+k47*Ne(k)*Ne(k)+k48*Ne(k)*O2(k)...
    +k52*O2n(k)*O2(k)+k53*O2n(k)+k65*On(k)*M(k)+k90*Ne(k)+k91*On(k)...
    +k102*Ne(k)+k117*On(k)*O2(k)+kw6;
O2p(k+1)=O2pGain(k)/O2pLoss(k);

OGain(k)=k19*On(k)*Hep(k)+k21*On(k)*Hep(k)*M(k)+k23*Hem(k)*O3(k)+k26*Hep(k)*O2(k)...
    +k29*Hep(k)*O2m(k)+k33*He2m(k)*O2(k)+k36*He2p(k)*O2(k)+k38*On(k)*O2p(k)...
    +k45*O2n(k)*Op(k)+2*k53*O2n(k)*O2p(k)+2*k59*Om(k)*O3(k)+k62*O2m(k)*O3(k)...
    +k64*Ne(k)*O3(k)+k65*On(k)*O2p(k)*M(k)+k68*O3(k)*He(k)+k69*O3(k)*O(k)...
    +k70*O3(k)*O2(k)+k71*O3(k)*O3(k)+k73*Ne(k)*O2(k)+2*k74*Ne(k)*O2(k)...
    +k77*Ne(k)*O2(k)+k78*Op(k)*O2(k)+k80*Ne(k)*O2(k)+k81*Om(k)*O2(k)...
    +k84*O2m(k)*O2(k)+k89*Ne(k)*On(k)+2*k90*Ne(k)*O2p(k)+3*k91*On(k)*O2p(k)...
    +2*k92*On(k)*Op(k)+k93*Ne(k)*O2m(k)+k94*On(k)*O2m(k)+k95*Ne(k)*Om(k)...
    +k96*Om(k)*O(k)+k97*Om(k)*O2(k)+k98*Ne(k)*O3(k)+k99*Ne(k)*Ne(k)*Op(k)...
    +k100*Ne(k)*Op(k)*O2(k)+2*k101*On(k)*Op(k)*M(k)+k102*Ne(k)*O2p(k)...

+k103*Om(k)*He(k)+2*k104*Ne(k)*O2m(k)+k105*On(k)*Op(k)+kw8*Om(k)+kw9*Op(k)+kw10*On(k);
OLoss(k)=FO+k24*Hem(k)+k31*Hep(k)+k39*On(k)+k46*O3(k)+2*k49*O(k)*O(k)...
    +k51*Om(k)*O2(k)+k56*O2n(k)+2*k66*O(k)*He(k)+2*k67*O(k)*O2(k)+k85*O2(k)*He(k)...
    +k86*O2(k)*O2(k)+k87*O2(k)*O(k)+k88*O2(k)*O3(k)+k106*Ne(k)+k107*Ne(k)...
    +k108*Ne(k)*O2(k)+k109*Op(k)*M(k)+k110*O2n(k)+2*k111*O(k)*O2(k)...
    +2*k112*O(k)*O(k)+2*k113*O(k)*He(k)+k114*O2n(k)*O(k)+kw5;
O(k+1)=OGain(k)/OLoss(k);

OmGain(k)=k33*He2m(k)*O2(k)+k80*Ne(k)*O2(k)+k102*Ne(k)*O2p(k)+k105*On(k)*Op(k)...
    +k107*Ne(k)*O(k)+k115*Ne(k)*Op(k)+k116*Ne(k)*Ne(k)*Op(k);
OmLoss(k)=FO+k25*Hem(k)+k32*Hep(k)+k51*O(k)*O2(k)+k59*O3(k)+k60*O3(k)...
    +k81*O2(k)+k95*Ne(k)+k96*O(k)+k97*O2(k)+k103*He(k)+k122*Ne(k)+kw8;
Om(k+1)=OmGain(k)/OmLoss(k);

OpGain(k)=k24*Hem(k)*O(k)+k25*Hem(k)*Om(k)+k26*Hep(k)*O2(k)+k27*Hep(k)*O3(k)...
    +k29*Hep(k)*O2m(k)+k31*Hep(k)*O(k)+k32*Hep(k)*Om(k)+k36*He2p(k)*O2(k)...
    +k76*Ne(k)*O2(k)+k77*Ne(k)*O2(k)+k106*Ne(k)*O(k)+k122*Ne(k)*Om(k);
OpLoss(k)=FO+k45*O2n(k)+k50*On(k)*O2(k)+k58*O3(k)+k78*O2(k)+k92*On(k)...
    +k99*Ne(k)*Ne(k)+k100*Ne(k)*O2(k)+k101*On(k)*M(k)+k105*On(k)+k109*O(k)*M(k)...
    +k115*Ne(k)+k116*Ne(k)*Ne(k)+k118*O2n(k)*M(k)+kw9;
Op(k+1)=OpGain(k)/OpLoss(k);

OnGain(k)=k43*Ne(k)*O3(k)+k56*O2n(k)*O(k)+k73*Ne(k)*O2(k)+k76*Ne(k)*O2(k)...
    +k93*Ne(k)*O2m(k)+k108*Ne(k)*O(k)*O2(k);
OnLoss(k)=FO+k19*Hep(k)+k21*Hep(k)*M(k)+k38*O2p(k)+k39*O(k)+k50*Op(k)*O2(k)...
    +k54*O3(k)+k55*O3(k)+k65*O2p(k)*M(k)+k82*O2(k)+k89*Ne(k)+k91*O2p(k)...
    +k92*Op(k)+k94*O2m(k)+k101*Op(k)*M(k)+k105*Op(k)+k117*O2p(k)*O2(k)...
    +k119*O2m(k)+kw10;
On(k+1)=OnGain(k)/OnLoss(k);

O3Gain(k)=k82*On(k)*O2(k)+k84*O2m(k)*O2(k)+k85*O(k)*O2(k)*He(k)...
    +k86*O(k)*O2(k)*O2(k)+k87*O(k)*O2(k)*O(k)+k88*O(k)*O2(k)*O3(k)...
```

```
    +k110*O2n(k)*O(k)+k114*O2n(k)*O(k)*O(k)+k117*On(k)*O2p(k)*O2(k)...
    +k118*O2n(k)*Op(k)*M(k)+k119*On(k)*O2m(k);
  O3Loss(k)=FO+k23*Hem(k)+k27*Hep(k)+k43*Ne(k)+k46*O(k)+k54*On(k)...
    +k55*On(k)+k58*Op(k)+k59*Om(k)+k60*Om(k)+k62*O2m(k)+k64*Ne(k)...
    +k68*He(k)+k69*O(k)+k70*O2(k)+k71*O3(k)+k98*Ne(k);
  O3(k+1)=O3Gain(k)/O3Loss(k);

  He2mGain(k)=k13*Hem(k)*He(k)*He(k)+k37*He2p(k)*O2(k)+kw3*He2p(k);
  He2mLoss(k)=FO+k12*Ne(k)+2*k18*He2m(k)+k33*O2(k)+k34*O2(k);
  He2m(k+1)=He2mGain(k)/He2mLoss(k);

  He2pGain(k)=k11*Hep(k)*He(k)*He(k)+k12*Ne(k)*He2m(k)+k14*Hem(k)*Hem(k)...
    +k18*He2m(k)*He2m(k);
  He2pLoss(k)=FO+k10*Ne(k)+k15*Ne(k)*Ne(k)+k16*Ne(k)+k17*Ne(k)*He(k)...
    +k35*O2(k)+k36*O2(k)+k37*O2(k)+kw3;
  He2p(k+1)=He2pGain(k)/He2pLoss(k);

  M(k+1)=O3(k+1)+On(k+1)+Op(k+1)+Om(k+1)+O(k+1)+O2p(k+1)+O2n(k+1)+O2m(k+1)...
    +O2(k+1)+Hep(k+1)+Hem(k+1)+He(k+1)+He2m(k+1)+He2p(k+1);


  dN(k+1)=abs(He(k)-He(k+1))+abs(Hem(k)-Hem(k+1))+abs(Hep(k)-Hep(k+1))...
    +abs(O2(k)-O2(k+1))+abs(O2m(k)-O2m(k+1))+abs(O2p(k)-O2p(k+1))+abs(O2n(k)-O2n(k+1))...
    +abs(O(k)-O(k+1))+abs(Om(k)-Om(k+1))+abs(Op(k)-Op(k+1))+abs(On(k)-On(k+1))...
    +abs(O3(k)-O3(k+1))+abs(He2m(k)-He2m(k+1))+abs(He2p(k)-He2p(k+1));

  %disp(dN(k+1))
  k=k+1;
  NHe=He(k);
  NHem=Hem(k);
  NHep=Hep(k);
  NHe2m=He2m(k);
  NHe2p=He2p(k);
  NO2=O2(k);
  NO2m=O2m(k);
  NO2p=O2p(k);
  NO2n=O2n(k);
  NO=O(k);
  NOm=Om(k);
  NOp=Op(k);
  NOn=On(k);
  NO3=O3(k);
  NNe=Hep(k)+O2p(k)+Op(k)+He2p(k)-O2n(k)-On(k);

end
```

Appendix E: Chemical Reactions and Rate Constants

Table E.1; Full Set of Chemical Reactions and Rate Constants

No.	Reaction	Rate Constant, k (cm, molecules, s)	Ref.
1	$e + He \rightarrow He^{*} + e$	$4.2E - 9\, T_e^{0.31} \exp(-19.8/T_e)$	83
2	$e + He \rightarrow He^{+} + e + e$	$1.5E - 9\, T_e^{0.68} \exp(-24.6/T_e)$	83
3	$He^{*} + He \rightarrow He + He + h\nu$	$3.06E - 15$	84
4	$e + He^{*} \rightarrow He + e$	$2.00E - 10\, T_e^{0.31}$	85
5	$He^{*} + He^{*} \rightarrow He^{+} + He + e$	$1.5E - 9\, T_o^{0.5}$	86
6	$e + He^{+} \rightarrow He^{*}$	$6.76E - 13\, T_e^{-0.5}$	86
7	$e + e + He^{+} \rightarrow He^{*} + e$	$5.12E - 27\, T_e^{-4.5}$	86
8	$e + He^{*} \rightarrow He^{+} + e + e$	$1.28E - 7\, T_e^{0.6} \exp(-4.78/T_e)$	86
9	$e + He_2^{+} \rightarrow He^{*} + He$	$5.0E - 9\, T_e^{-0.5}$	83
10	$He^{+} + He + He \rightarrow He_2^{+} + He$	$2.0E - 31$	83
11	$e + He_2^{*} \rightarrow He_2^{+} + e + e$	$9.75E - 10\, T_e^{0.71} \exp(-3.4/T_e)$	85
12	$He^{*} + He + He \rightarrow He_2^{*} + He$	$1.3E - 33$	85
13	$He^{*} + He^{*} \rightarrow He_2^{+} + e$	$2.0E - 9$	87
14	$e + e + He_2^{+} \rightarrow He + He + e$	$5.036E - 27\, T_e^{-4.5}$	87
15	$e + He_2^{+} \rightarrow He + He$	$1.0E - 8$	87
16	$e + He + He_2^{+} \rightarrow He + He + He$	$2.0E - 27$	87
17	$He_2^{*} + He_2^{*} \rightarrow He_2^{+} + He + He + e$	$1.5E - 9$	88
18	$O^{-} + He^{+} \rightarrow O + He$	$2.0E - 7\, T_o^{-1}$	86
19	$O_2^{-} + He^{+} \rightarrow O_2 + He$	$2.0E - 7\, T_o^{-1}$	86
20	$O^{-} + He^{+} + M \rightarrow O + He + M$	$2.0E - 25\, T_o^{-2.5}$	86
21	$He^{*} + O_2 \rightarrow O_2^{+} + He + e$	$2.54E - 10\, T_o^{0.5}$	86
22	$He^{*} + O_3 \rightarrow O_2^{+} + O + He + e$	$2.54E - 10\, T_o^{0.5}$	86
23	$He^{*} + O \rightarrow O^{+} + He + e$	$2.54E - 10\, T_o^{0.5}$	86
24	$He^{*} + O^{*} \rightarrow O^{+} + He + e$	$2.54E - 10\, T_o^{0.5}$	86
25	$He^{+} + O_2 \rightarrow O^{+} + O + He$	$1.07E - 9\, T_o^{0.5}$	86
26	$He^{+} + O_3 \rightarrow O^{+} + O_2 + He$	$1.07E - 9\, T_o^{0.5}$	86
27	$He^{+} + O_2 \rightarrow O_2^{+} + He$	$3.3E - 11\, T_o^{0.5}$	86
28	$He^{+} + O_2^{*} \rightarrow O^{+} + O + He$	$1.07E - 9\, T_o^{0.5}$	86
29	$He^{+} + O_2^{*} \rightarrow O_2^{+} + He$	$3.3E - 11\, T_o^{0.5}$	86
30	$He^{+} + O \rightarrow O^{+} + He$	$5.0E - 11\, T_o^{0.5}$	86
31	$He^{+} + O^{*} \rightarrow O^{+} + He$	$5.0E - 11\, T_o^{0.5}$	86
32	$He_2^{*} + O_2 \rightarrow O + O^{*} + He + He$	$1.0E - 12$	92
33	$He_2^{*} + O_2 \rightarrow O_2^{+} + He + He + e$	$7.0E - 11$	85
34	$He_2^{+} + O_2 \rightarrow O_2^{+} + He + He$	$5.0E - 10$	85

Table E.1 Continued

35	$He_2^+ + O_2 \rightarrow O^+ + O + He + He$	$7.0E - 10$	85
36	$He_2^+ + O_2 \rightarrow O_2^+ + He_2^*$	$1.4E - 9$	93
37	$O^- + O_2^+ \rightarrow O + O_2$	$2.6E - 8\ T_o^{-0.44}$	94
38	$O^- + O \rightarrow O_2 + e$	$5.0E - 10$	94
39	$e + O_2^* \rightarrow O_2 + e$	$2.06E - 9\ \exp\,(-1.163/T_e)$	94
40	$O_2^* + O_2 \rightarrow O_2 + O_2$	$2.2E - 18\ T_o^{0.8}$	94
41	$O_2^* + O \rightarrow O_2 + O$	$7.0E - 16$	94
42	$e + O_3 \rightarrow O^- + O_2$	$2.12E - 9\ T_e^{-1.058}\exp\,(-.93/T_e)$	94
43	$O_2^- + O_2^+ \rightarrow O_2 + O_2$	$2.0E - 7\ T_o^{-0.5}$	94
44	$O_2^- + O^+ \rightarrow O_2 + O$	$2.0E - 7\ T_o^{-0.5}$	94
45	$O_3 + O \rightarrow O_2 + O_2$	$1.8E - 11\ \exp\,(-2300/T)$	94
46	$e + e + O_2^+ \rightarrow O_2 + e$	$1.0E - 19\ (0.026/T_e)^{4.5}$	94
47	$e + O_2^+ + O_2 \rightarrow O_2 + O_2$	$6.0E - 27\ (0.026/T_e)^{1.5}$	94
48	$O + O + O \rightarrow O_2 + O$	$6.2E - 32\ \exp\,(-750/T)$	94
49	$O^- + O^+ + O_2 \rightarrow O_2 + O_2$	$2.0E - 25\ T_o^{-2.5}$	94
50	$O + O^* + O_2 \rightarrow O_2 + O_2$	$9.9E - 33$	94
51	$O_2^- + O_2^+ + O_2 \rightarrow O_2 + O_2 + O_2$	$2.0E - 25\ T_o^{-2.5}$	94
52	$O_2^- + O_2^+ \rightarrow O_2 + O + O$	$1.0E - 7$	86
53	$O^- + O_3 \rightarrow O_2 + O_2 + e$	$3.01E - 10\ T_o^{0.5}$	86
54	$O^- + O_3 \rightarrow O_2^- + O_2$	$1.02E - 11\ T_o^{0.5}$	86
55	$O_2^- + O \rightarrow O^- + O_2$	$1.5E - 10\ T_o^{0.5}$	86
56	$O_2^- + O_2^* \rightarrow O_2 + O_2 + e$	$2.0E - 10\ T_o^{0.5}$	86
57	$O^+ + O_3 \rightarrow O_2^+ + O_2$	$1.0E - 10$	86
58	$O^* + O_3 \rightarrow O_2 + O + O$	$1.2E - 10$	86
59	$O^* + O_3 \rightarrow O_2 + O_2$	$1.2E - 10$	86
60	$O_2^* + O_2^* \rightarrow O_2 + O_2$	$9.0E - 17\ \exp\,(-560/T)$	86
61	$O_2^* + O_3 \rightarrow O_2 + O_2 + O$	$5.2E - 11\ \exp\,(-2840/T)$	86
62	$O_2^* + He \rightarrow O_2 + He$	$8.0E - 21\ T_o^{0.5}$	86
63	$e + O_3 \rightarrow O + O_2 + e$	$1.0E - 8\ T_o^{-0.5}$	95
64	$O^- + O_2^+ + M \rightarrow O + O_2 + M$	$2.0E - 25\ T_o^{-2.5}$	86
65	$O + O + He \rightarrow O_2 + He$	$0.62 \cdot 5.2E - 35\ \exp\,(900/T)$	96
66	$O + O + O_2 \rightarrow O_2 + O_2$	$1.15 \cdot 5.2E - 35\ \exp\,(900/T)$	96
67	$O_3 + He \rightarrow O + O_2 + He$	$0.54 \cdot 7.26E - 10\ \exp\,(-11400/T)$	96
68	$O_3 + O \rightarrow O + O_2 + O$	$0.13 \cdot 7.26E - 10\ \exp\,(-11400/T)$	96
69	$O_3 + O_2 \rightarrow O + O_2 + O_2$	$7.26E - 10\ \exp\,(-11400/T)$	96
70	$O_3 + O_3 \rightarrow O + O_2 + O_3$	$2.27 \cdot 7.26E - 10\ \exp\,(-11400/T)$	96
71	$O_2^* \rightarrow O_2 + hv$	$3.7E - 4$	96
72	$e + O_2 \rightarrow O^- + O$	$1.07E - 9\ T_e^{-1.391}\exp\,(-6.26/T_e)$	94
73	$e + O_2 \rightarrow O + O + e$	$6.86E - 9\ \exp\,(-6.29/T_e)$	94

Table E.1 Continued

74	$e + O_2 \rightarrow O_2^+ + e + e$	$2.34E-9\ T_e^{1.03}\exp(-12.29/T_e)$	94
75	$e + O_2 \rightarrow O^- + O^+ + e$	$7.1E-11\ T_e^{0.5}\exp(-17/T_e)$	94
76	$e + O_2 \rightarrow O + O^+ + e + e$	$1.88E-10\ T_e^{1.699}\exp(-16.81/T_e)$	94
77	$O^+ + O_2 \rightarrow O + O_2^+$	$2.0E-11\ T_o^{-0.5}$	94
78	$e + O_2 \rightarrow O_2^* + e$	$1.37E-9\ \exp(-2.14/T_e)$	94
79	$e + O_2 \rightarrow O + O^* + e$	$3.49E-8\ \exp(-5.92/T_e)$	94
80	$O^* + O_2 \rightarrow O + O_2^*$	$1.0E-12$	94
81	$O^- + O_2 \rightarrow O_3 + e$	$5.0E-15$	94
82	$e + O_2 + M \rightarrow O_2^- + M$	$3.6E-31\ T_e^{-0.5}$	86
83	$O_2^* + O_2 \rightarrow O + O_3$	$2.95E-21\ T_o^{0.5}$	86
84	$O + O_2 + He \rightarrow O_3 + He$	$0.54 \cdot 1.85E-35\ \exp(1057/T)$	96
85	$O + O_2 + O_2 \rightarrow O_3 + O_2$	$1.85E-35\ \exp(1057/T)$	96
86	$O + O_2 + O \rightarrow O_3 + O$	$0.13 \cdot 1.85E-35\ \exp(1057/T)$	96
87	$O + O_2 + O_3 \rightarrow O_3 + O_3$	$2.27 \cdot 1.85E-35\ \exp(1057/T)$	96
88	$e + O^- \rightarrow O + e + e$	$5.47E-8\ T_e^{0.324}\exp(-2.98/T_e)$	94
89	$e + O_2^+ \rightarrow O + O$	$2.2E-8\ T_e^{-0.5}$	94
90	$O^- + O_2^+ \rightarrow O + O + O$	$2.6E-8\ T_o^{-0.44}$	94
91	$O^- + O^+ \rightarrow O + O$	$4.0E-8\ T_o^{-0.44}$	94
92	$e + O_2^* \rightarrow O + O^-$	$4.19E-9\ T_e^{-1.376}\exp(-5.19/T_e)$	94
93	$O^- + O_2^* \rightarrow O_2^- + O$	$1.1E-11$	94
94	$e + O^* \rightarrow O + e$	$8.17E-9\ \exp(-0.4/T_e)$	94
95	$O + O^* \rightarrow O + O$	$8.0E-12$	94
96	$O^* + O_2 \rightarrow O + O_2$	$7.0E-12\ \exp(67/T)$	94
97	$e + O_3 \rightarrow O_2^- + O$	$1.0E-9$	94
98	$e + e + O^+ \rightarrow O + e$	$1.0E-19\ (0.026/T_e)^{4.5}$	94
99	$e + O^+ + O_2 \rightarrow O + O_2$	$6.0E-27\ (0.026/T_e)^{1.5}$	94
100	$O^- + O^+ + M \rightarrow O + O + M$	$2.0E-25\ T_o^{-2.5}$	86
101	$e + O_2^+ \rightarrow O + O^*$	$8.88E-9\ T_e^{-0.7}$	86
102	$O^* + He \rightarrow O + He$	$1.0E-13$	86
103	$e + O_2^* \rightarrow O + O + e$	$4.2E-9\ \exp(-4.6/T_e)$	95
104	$O^- + O^+ \rightarrow O + O^*$	$4.9E-10\ T_o^{-0.5}$	95
105	$e + O \rightarrow O^+ + e + e$	$9.0E-9\ T_e^{0.7}\exp(-13.6/T_e)$	94
106	$e + O \rightarrow O^* + e$	$4.54E-9\ \exp(-2.36/T_e)$	94
107	$e + O + O_2 \rightarrow O^- + O_2$	$1.0E-31$	94
108	$O + O^+ + M \rightarrow O_2^+ + M$	$1.0E-29\ T_o^{0.5}$	86
109	$O_2^- + O \rightarrow O_3 + e$	$1.5E-10\ T_o^{0.5}$	86
110	$O + O + O_2 \rightarrow O_2^* + O_2$	$1.93E-35\ T_o^{-0.63}$	86
111	$O + O + O \rightarrow O_2^* + O$	$6.93E-35\ T_o^{-0.63}$	86
112	$O + O + He \rightarrow O_2^* + He$	$9.88E-35$	86

Table E.1 Continued

113	$O_2^- + O + O \rightarrow O_3 + O$	$3.82E - 34$	95
114	$e + O^+ \rightarrow O^*$	$5.3E - 13\, T_e^{-0.5}$	86
115	$e + e + O^+ \rightarrow O^* + e$	$5.12E - 27\, T_e^{-4.5}$	86
116	$O^- + O_2^+ + O_2 \rightarrow O_3 + O_2$	$2.0E - 25\, T_o^{-2.5}$	94
117	$O_2^- + O^+ + M \rightarrow O_3 + M$	$2.0E - 25\, T_o^{-2.5}$	94
118	$O^- + O_2^* \rightarrow O_3 + e$	$2.2E - 11$	94
119	$e + O_2^* + O_2 \rightarrow O_2^- + O_2$	$1.9E - 30$	94
120	$e + O_2^* + O \rightarrow O_2^- + O$	$1.0E - 31$	94
121	$e + O^* \rightarrow O^+ + e + e$	$9.0E - 9\, T_e^{0.7} \exp(-11.6/T_e)$	94
122	$e + O_2^* \rightarrow O_2^+ + e + e$	$9.0E - 10\, T_e^{2.0} \exp(-11.6/T_e)$	95
123	$O_2^- + M \rightarrow O_2 + M + e$	$2.7E - 10\, T_o^{0.5} \exp(-5590/T)$	97